Nanocrystalline Semiconductor Nuclear Radiation Detectors

by

Geehyun Kim

A dissertation submitted in partial fulfillment
of the requirements for the degree of
Doctor of Philosophy
(Nuclear Engineering and Radiological Sciences)
in The University of Michigan
2013

Doctoral Committee:

Professor David K. Wehe, Co-Chair
Assistant Research Scientist Mark D. Hammig, Co-Chair
Professor Nicholas A. Kotov
Associate Professor Jamie Phillips
Staff Scientist Jeffrey M. Pietryga

For all the people, who have looked after me.

ACKNOWLEDGEMENTS

It has been five and half years since I started a new page of my life in Ann Arbor. It was not a short period of time in my life. A boy in his mid-20s has come to be in his 30s while he was earning a Ph.D. with two master's degrees. Life as a graduate student was a process of endless agonizing and compromising. I cannot remember how many times I had to agonize about upcoming decisions in my life, from the most trivial things to the significant issues, struggling with the practical necessity of compromise. Disappointed and frustrated sometimes, however, I have learned good lessons to possess the guts to keep composure of mind to deal with the situation and to be easy on myself and to be a little flexible.

One of the difficulties I had to encounter while I was preparing the dissertation was dealing with strong desires for perfectionism and self-satisfaction. In some aspects, this process was rather a fight against myself to suppress and to get over with my stubbornness and self-esteem, which took most of the time I spent. It was just hard for me to let go of the notion that I had to do the best job I could and that I always knew I could do better. I guess, life does not always work out necessarily in the way it was planned. Maybe it is because one's earlier plan was bad, and one realizes this as he gets older and wiser. Thus, as always, there are some regrets. I have to admit that I have been selfish; I didn't have enough room in my mind to take care of people around me even though I have received a lot from others. One thing I have realized is that I was truly a lucky person to meet everyone around me. And this dissertation owes a lot to many people I have to appreciate and acknowledge.

First of all, I cannot thank enough Dr. David Wehe and Dr. Mark Hammig as my academic/research advisors, for kind guidance and worry-proof support on my research. Their training philosophy and guidance has affected me a lot, and made a big contribution to my tenets in teaching and mentoring students. I have to tell a lot in order to effectively describe my complicated feelings about the recent five and half years, however, let's put them all under the name of the reminiscence. There are two major events that I will just mention: SORMA and the Annual DTRA Technical Reviews. These were really interesting and valuable experiences. I have grown up out of those experiences.

Secondly, I would like to thank all my committee members that every single one of had been very important people in my research at the graduate school. Dr. Jamie Phillips was the first person that I had asked for a help in my research outside the department. Back then, I was just a new graduate student, not even sure about whether it was appropriate to ask for a help or an advice to someone you've never met, even outside the department. Dr. Phillips was so kind that I could realize that the scientific community is indeed an open world of people helping each other rather than just full of competition. He encouraged me in the first place, that I could start all the interdisciplinary projects with an open mind to others. In this regard, Dr. Nicholas Kotov has opened up a lot of opportunities in my research, especially in nanocrystal device applications, and he also opened up my eyes in this field. He was always open for suggestion and discussion, and always willing to help people. I was able to use a couple of key pieces of equipment in my research thanks to his help. And I also have a very nice memory working with his team members: Dr. Sudhanshu Srivastava, Dr. Yunlong Zhou, Dr. Jae-il Park and Yoonseob Kim.

Probably the most intense but definitely the best research-oriented experience in my graduate school was when I spent the spring and summer in Los Alamos. It was fun, instructive, tough, and inspiring; I enjoyed a lot. I would like to thank Dr. Jeffrey

Pietryga along with other team members – Dr. Victor Klimov, Dr. Wan Ki Bae, Dr. Youngshin Park, Dr. Weon-kyu Koh, Dr. Hunter McDaniel, Dr. Lazaro Padhila, Dr. Bhola Nath Pal, Dr. Istvan Robel, Dr. Jason Stewart and Qianglu Lin – for giving me opportunities to work and study at LANL. They were such kind mentors for me and I have learned a lot from them. It was very fun working in a group, spending time together from time to time. I really wished I could spend more time there, but again, life does not necessarily work out as I would like it to be. However, Dr. Pietryga has been a very nice mentor, a good person to talk to, and an interesting Michigan alumnus friend of mine. I would also like to thank Dr. Aaron Couture at LANSCE for helping me out arranging everything so that I could do some experiments there.

I would also like to thank other great mentors in my academic life for providing me with invaluable advices and hearty support. Dr. John Lee has given me a number of inspiring comments and lessons in life, which gave me opportunities to reflect on myself and strengthen my faith as a scientist. I have learned a lot from his enthusiasm and integrity. Dr. Hee Dong Choi from Seoul National University and Dr. Soo Hyun Byun from McMaster University have also given me good advice and support as senior scholars in this field. Even though I didn't have many chances to visit them, it was always a pleasure to meet and talk to them. It was also delightful to interact with Korean visiting scholars and research fellows in the department. I would like to acknowledge Dr. Kwang-il Ahn, Dr. Han Gyu Joo, Dr. Keun Bae Oh, Dr. Nam-il Tak, and Dr. Jaecheon Kim for making helpful suggestions for my career and sharing their experiences with me.

Sure enough, I enjoyed the time at the Nuclear Engineering and Radiological Sciences department in the University of Michigan. I miss the times when I had meaningful discussions from time to time with my former group members – Dr. Jason Hayward, Dr. Haori Yang, Dr. Benjamin Kowash, Dr. Paul Barton and Dr. Manhee Jeong. I would especially like to thank Dr. Manhee Jeong about his sincere support

and care for me as a senior student in the group and a colleague. Other students in the NERS department as well as Ms. Peggy Gramer have provided such a friendly atmosphere that foreign national students can easily blend in to the department. I felt warmth and hospitality from the people in the department, at the early stage of my UM NERS life, thanks to my friends – Nick, Troy, Ceris, Greg, Eric, Shikha, Sonal & Willy, Crystal & Brian, Eva, Heeho and Doug (and Michelle). Needless to say, it was not the easiest thing to adapt myself to the new environment; thank you all for talking to me first, and accepting me as a friend of yours without any bias.

I also had a good time serving as a president (and an advisor) of the Korean Student Association – Graduate (KSAG) at the University of Michigan. Thus, I would like to acknowledge all the former and current staff members of KSAG and kudos for their hearty support and hard work for the welfare of Korean community at the University of Michigan. I would have to mention 30+ people, in order to name all of them, so I will just thank them all briefly. I also want to mention UM Korean Grad Basketball (KGB) crews, who dragged me out of my own cave. Of course, it was sincerely great fun playing basketball with them, however, there has always been something beyond just playing basketball with each other. I might have to mention names of another 20+ people in order to acknowledge them individually. Thank you all for caring for me. Times I spent with Taek-kyun club crews from the Seoul National University was another energizer for my Michigan life. I would like to thank Dr. Young Chang Cho, Mr. Sang-Heon Song, Mr. Young Soo Jung, and Dr. Michael Ralston for asking me after from time to time and always wishing me good luck. I also spent a lot of time with Yun Seok Eo from the Physics department, taking classes together and chatting about gazillion topics, which was another pleasurable part of my Michigan life.

I would like to thank people currently in Korea, too. My highschool friends, Sang Jae, Sungwoo, Heechul, and Daehyun have never forgot about me for the recent five

and half years. Whenever they get together, they have never failed to call me and ask after me. My Korean nuclear engineer friends from the Seoul National University, another 20+ people, including Dr. Nam Suk Jung and Byung Gun, which were also teammates in the ANPG group, are also appreciated for treating me heavily with dinners and drinks whenever I trip back to Korea. There are many more people I have to thank and acknowledge in this category, and I feel sorry that I have to cut down the list at the moment.

A significant portion of my Ph. D. study was supported by the Defense Threat Reduction Agency (DTRA) Basic Research Program, HDTRA 1-07-1-0021. I would like to thank the agency and the program manager for giving me good opportunities to participate and study, even if I was a foreign national student.

Lastly, I would like to mention the most important people in my life. I could have not done anything without bottomless support from my family and my girlfriend Ms. Sohhyun (Holly) Chung. It was my best luck that I could be the son of my parents, the elder brother of my younger brother, a member of my grand family, and the boyfriend of Holly. I have no doubt that my parents have done the best job in the world devoting their life to their two sons, and they were more than willing to sacrifice themselves for the sake of their sons. Even though I had made them fly 7000 miles, I was really happy that I could have my parents in my defense presentation. My brother, Kiho, and I had to go through toughest part of my graduate student life together. I really appreciate his assistance while he was living with me in Ann Arbor. He had no better than a housemaid life here to support me. I have always felt sorry in a deeper corner in my heart that I could not provide him with more delightful life and environment, due to the financial difficulties I had when he was here.

And I want to express a sincere appreciation for my lovely girlfriend Holly, for being an un-depleted source of the bottomless support I received. How can I say everything? Thank you very much, and I love you.

PREFACE

First of all, thank you for taking the effort to pick up this dissertation and for deciding to read this. In this dissertation, I will discuss the fabrication and characterization of nanostructured media for nuclear radiation detection, as a part of nuclear instrumentation. For the sake of *a broader spectrum of readership including non-scientific community*, I will give a brief introduction to the area of radiation detectors. I will then make a few points to justify the significance of this research in the field of nuclear science and technology.

To start, what is radiation? Even though people casually talk about the threats of radiation, and the general public has its own impression about radiation, few people know that they live under the steady influence of radiation, and they "survive" thanks to radiation in a broader sense. Radiation, in its broader definition, refers to any particle or wave that has energy to travel through a medium. This includes virtually any elementary or composite particles, such as bosons and fermions, hadrons, leptons, photons, etc. – anything you can think of. I would not categorize elementary and composite particles here; however, they belong to the big family of radiation. What the public calls radiation refers in general, to the "ionizing radiation," particles (waves) which have the ability to ionize an atom; thus, creating charged particles in consequence. Nuclear radiation, which comes as an outcome of nuclear decay process or nuclear reactions, such as alpha particles, beta particles, gamma rays and neutrons falls under this category. And this is what most people are concerned with. Atomic

radiation, notably characteristic x-rays from an excited atom, are often utilized for medical applications, as is well-known. Even though the boundary between the two becomes somewhat ambiguous at some point, there are also non-ionizing radiation, which includes a wide spectrum of electromagnetic waves of lower frequency (or energy, since $E = h\nu$) – ultraviolet (UV), visible light, infrared, microwaves, radio frequency waves, thermal waves. I have categorized neutrinos under the non-ionizing category, because there is not yet a verified ionizing process from the neutrino interaction with matter, as shown in the schematic below.

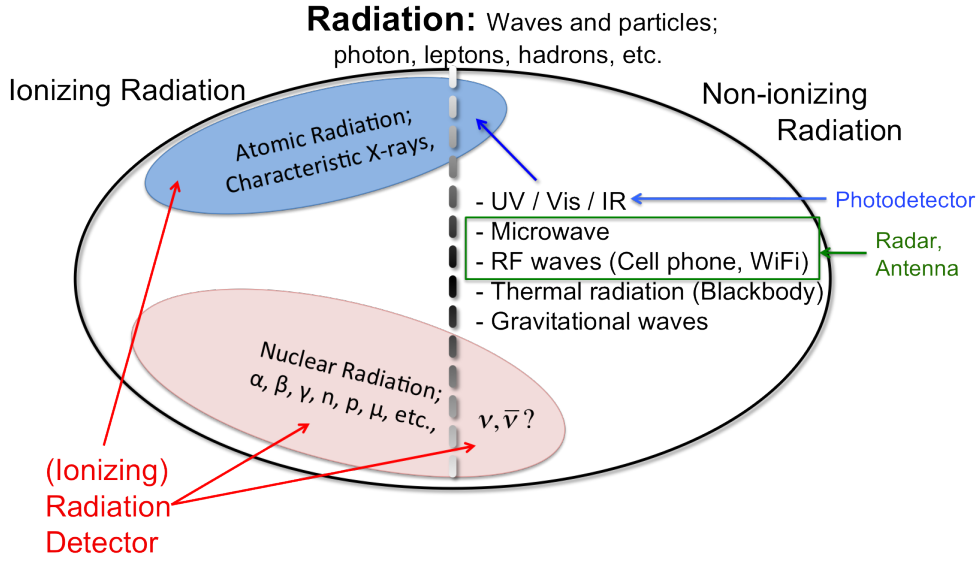

Let's look into the instrumental side of these types of radiation. There are devices developed specific to a certain wavelength range of radiation. For instance, photodetectors or photodiodes are developed to optimally respond to the photonic wavelength range of mainly visible light, infrared and UV. Measures to identify longer wavelength particles (microwaves and RF waves) utilize conductive sensors in the form of a radar or an antenna. However, what we pay attention to here in nuclear engineering are the categories of **nuclear radiation** and **atomic radiation**. We, as nuclear engineers, would like to "sense" the particle in a relatively higher energy range, where it would

be capable of ionizing atoms either directly or indirectly. The "sensors" should be able to detect and measure each individual particle, what we call *"(ionizing) radiation detectors."*

The (ionizing) radiation detector is a major part of nuclear instrumentation as shown in the figure below. The field of nuclear instrumentation involves such area studying and utilizing a) accelerators, b) various source facilities, c) detectors, and d) molecular or ion beam lines. However, there is no clear distinction between each boundary, because many of these instruments are often systemically combined with each other to compose an integrated facility. Amongst these, I, in particular, pay a little more attention to detectors. When we say detector in general, this usually refers to any type of detectors, not only limited to those used within the field of nuclear radiation – photodetectors, chemical and biological sensors, and even smoke detectors. (Actually, smoke detectors do utilize nuclear radiation.) However, when people say radiation detectors, this usually refers to ionizing (or nuclear) radiation detectors which are a part of nuclear instrumentation. Here, I am not trying to cover the whole area of detectors, just trying to concentrate only on a little portion of the detector category which is normally used in the nuclear science and technology field. Technically speaking, the nanocrystalline (NC) semiconductor detector developed and investigated in this dissertation can be exploited as an ionizing radiation detector. However, since we paid little attention to x-rays and haven't really tested for an x-ray source in the experiments, I would like to confine the scope of these NC detectors in this research within the boundary of nuclear radiation (α's, β's, and γ's). It should be noted that most nuclear radiation detectors are ionizing radiation detectors, and, thus, can also be used for x-ray or optical photon detection with a few adjustments in the set up.

In this study, we use quantum dots as an interaction medium for radiation detection and measurement. This study may appear to be only specific to semiconductor

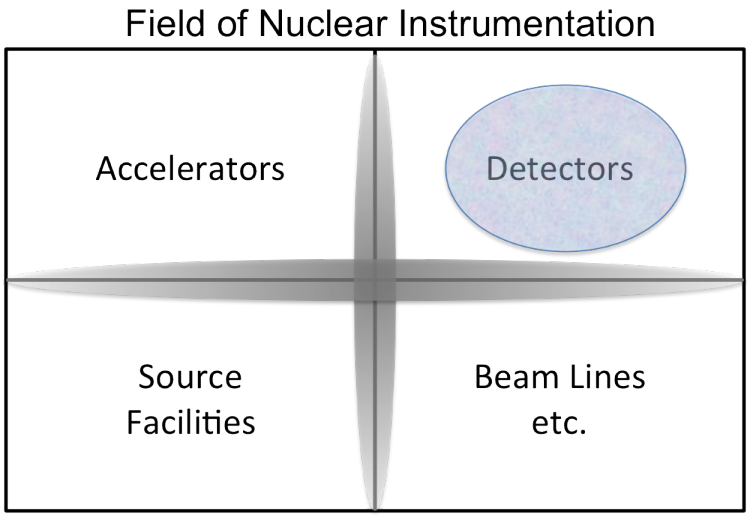

technology and nuclear radiation detection. However, not narrowly limited to the detection of ionizing particles emitted from the nucleus, sensing and measurement technologies based on semiconductor materials have played very crucial roles in the exploration of new sciences as well as nuclear engineering and technology. For example, the 2010 Nobel Prize in Physics was awarded for the development of sensor technologies using semiconductors (CCDs), and the development of LEDs and solar cells have become spotlighted along with the contemporary energy problem. In this regard, radiation detectors, photodetectors, and solar cells have many things in common. Notably, they are all based upon utilizing photons, converting incident radiation energy (photons) into electric energy – photovoltaic devices. However, radiation detectors are different from those two in the sense that they have to extract energy information much more precisely. Whereas photodetectors are often developed to count each individual photon coming in, an LED follows exactly the opposite process from the photodetector (converting electric charges injected by a potential difference into photons). Solar cells normally concentrate on efficiently converting the incident photon into the electric charge carrier, not necessarily correlating the incident photon energy into the amplitude of the signal.

In addition, sensing and measurement technologies can be further utilized to study

astronomy and to support space missions. The study on Cosmic Microwave Background Radiation, which received the Nobel Prize in 2006, was also enabled by support from good sensor technologies. Therefore, there is an increasing demand for measurement techniques and instrumental research as a cornerstone for basic science and technology application.

Lastly, I would like to point out the value of this research in the field of nuclear instrumentation. Even though this research was an exploratory step, and thus, the result may not be totally ground-breaking, I consider the value of this study as a part of my Ph.D work in the following three aspects:

1) One of the first pioneering approaches of NC assembly as a semiconductor media for the nuclear radiation detection.

2) Interdisciplinarity – Connections between various disciplines; starting from condensed matter physics, chemical engineering, material science, electrical engineering, and finally combining with nuclear science.

3) One-stop research process – I have gone through all these processes myself at least once. Starting from theoretical studies, I have performed NC synthesis and characterization (SEM, XRD, TEM, PL), fabrication of the NC assembly, and testing the device with radiation sources.

I hope you enjoy your reading and thank you again for your interest in this dissertation. Have fun.

Geehyun Kim

Dec. 2012

Ann Arbor, MI

TABLE OF CONTENTS

DEDICATION ii

ACKNOWLEDGEMENTS iii

PREFACE viii

LIST OF FIGURES xv

LIST OF TABLES xxiii

LIST OF APPENDICES xxiv

LIST OF ABBREVIATIONS xxv

ABSTRACT xxvii

CHAPTER

I. Introduction 1

II. Nanocrystalline Semiconductor (Nanocrystal, NC) "Quantum Dots (QD)" 7

2.1 Optical Properties of Nanocrystal 8
2.1.1 Two Approaches 8
2.1.2 Size Dependent Properties of Nanocrystal (NC) . . 11
2.1.3 Carrier Multiplication (CM) 36
2.2 Motivation for the Radiation Detector Application 44
2.2.1 Average Ionization Energy (W-value) 45
2.2.2 High atomic number and density of material 47
2.2.3 Low-cost fabrication modality with versatility in the size and shape 49
2.3 Design Parameters and Problems 50
2.3.1 Dimension – Thickness 50

2.3.2 Confronting Challenges 53

III. Experiments: Synthesis, Characterization, and Fabrication 57

3.1 Synthesis of Nanocrystals 57
3.1.1 Synthesis of CdTe Nanostructures 60
3.1.2 Synthesis of CdTe Nanowire 63
3.1.3 Synthesis of Lead Chalcogenide Nanocrystal 64
3.2 Characterization of Nanocrystals 75
3.2.1 Transmission Electron Micrograph (TEM) 77
3.2.2 Photoluminescence (PL) 80
3.2.3 X-ray Diffraction (XRD) 82
3.3 Fabrication of Nanocrystal Assembly 88
3.3.1 Drop-cast plain NC assemblies 90
3.3.2 Layer-by-Layer Method 95
3.3.3 Blended Assembly of NC/Polymer Composite . . . 104
3.3.4 CdTe NW Assembly 109
3.3.5 Metal contacts 111

IV. Results and Evaluation 113

4.1 CdTe Nanostructure System 114
4.1.1 CdTe Nanocrystal Assembly 114
4.1.2 CdTe Nanowire Assembly 121
4.2 Lead Chalcogenide (PbX, X = S, Se, Te) Nanocrystals 130
4.2.1 Plain Drop/Spin Cast Samples 130
4.2.2 Ligand Exchange – Chemically Treated Samples . . 135
4.2.3 Blended Assembly of NC/Polymer Composite . . . 143

V. Conclusion 163

5.1 Achievements 164
5.2 Confronting Challenges 166
5.3 Future Work 168
5.3.1 Material Possibilities 168
5.3.2 Junction Studies 169
5.3.3 Patterning on the Assembly 170
5.4 Final Remarks 171

APPENDICES 172

BIBLIOGRAPHY 198

LIST OF FIGURES

Figure

2.1 Evolution of silicon atomic orbitals into crystal energy bands. 10

2.2 Creation of electron-hole via photon absorption 28

2.3 Energy level structures of bulk semiconductor, quantum dot and molecule. 30

2.4 Size-dependent optical properties of PbSe nanocrystal. 35

2.5 Size-dependent optical properties of CdSe nanocrystal. 36

2.6 Dependence of first absorption peak and extinction coefficient on the size of CdX (X=s, Se, Te) nanocrystals. 37

2.7 Energy conversion mechanism in a conventional solar cell and the power conversion efficiency. 39

2.8 Photo-excited carrier dynamics in bulk and nanocrystal semiconductors. 40

2.9 Schematics of impact ionization (II) and Auger recombination (AR) 40

2.10 Schematics of dynamical channels for photoinduced hot electron-hole pair in NCs. 42

2.11 Average energy required for ionization (W-value) vs. band gap E_g. . 46

2.12 Comparison of common semiconductor radiation detector materials. 48

2.13 Intrinsic peak efficiency comparison between HPGe, CZT and PbTe. 50

2.14 Simulated tracks of 5.486 MeV alpha particle in single crystalline PbS. 53

2.15 Simulated tracks of electrons in a PbO slab calculated by PENELOPE Monte Carlo code. 54

3.1 A schematic of TGA-stabilized colloidal CdTe NC synthesis. 61

3.2 A typical experimental setup for the colloidal CdTe NC synthesis. . 62

3.3 The PL emission spectra of parent CdTe NCs and resulting NWs. . 64

3.4 TEM image and diffraction pattern of the TGA-stabilizaed CdTe NCs. 65

3.5 TEM images of CdTe NWs assembled from the CdTe NCs. 65

3.6 Synthesis of colloidal PbSe nanocrystal (NC) dispersion through hot injection method. 67

3.7 TEM images of PbSe NC synthesized in various reaction conditions. 70

3.8 Quantum dot clean-up process 71

3.9 PL absorption and emission spectra of PbSe NCs. 72

3.10 Simulated spectra from PbS NC and PbSe NC assembly 74

3.11 TEM images of PbS NCs synthesized through a typical procedure. . 76

3.12 HRTEM images of star-shaped PbSe NC particles. 78

3.13 Illustration of star-shaped PbSe NC particle growth. 78

3.14 Electron Diffraction (ED) pattern of the PbSe NCs. 79

3.15 X-ray energy dispersive spectrum (EDS) and the elemental composition analysis of the PbSe NCs. 80

3.16 A typical UV-VIS absorption spectrum of CdTe NC. 81

3.17 PL emission and excitation spectra obtained from size-selectively precipitated CdTe NCs. 83

3.18 PL absorption and emission spectra of PbS NC synthesized in various condition. 84

3.19 Schematic illustration of the Rigaku rotating anode XRD machine. . 84

3.20 XRD spectra of PbSe NC samples synthesized in various conditions. 87

3.21 Schematic of NC assembly made by drop-casting NC dispersion. . . 91

3.22 SEM images of the CdTe NC assembly surface. 92

3.23 PbSe NC assembly deposited by drop-casting method. 92

3.24 SEM images of the PbSe NC assembly surface. 94

3.25 Illustration of charge carrier transport hampered by excess ligands and cracks in the NC assembly. 95

3.26 SEM images of the PbSe NC assembly surface. 96

3.27 Schematic of NC assembly made by drop-casting NC dispersion. . . 97

3.28 EDS analysis on the cross-sectional view of the LBL deposited CdTe NC assembly 98

3.29 Cross-sectional view of the LBL deposited CdTe NC assembly sandwiched between Al and Pt electrodes on silicon wafer. 99

3.30 Schematic of charge carrier transport enhancement in NC assemblies promoted by the ligand exchange. 99

3.31 Schematic of fabricating PbSe NC thin films incorporating various ligands. 100

3.32 SEM images of PbS NC assembly deposited by drop-casting method. 102

3.33 SEM images of PbS NC assembly deposited by dip-coating method by 20 times. 103

3.34 Dip-coated PbS assembly with EDT treatment repeated for 150 times. 104

3.35 Configuration and charge carrier transport of the NC assembly in a blended composite structure. 105

3.36 PbSe NC/MEH-PPH composite assembly deposited on the glass substrate. 107

3.37 PbSe NC/MEH-PPH composite assembly deposited on plastic substrates. 108

3.38 Typical geometry configuration for a PbSe quantum dot separated by a single link of the MEH-PPV polymer chain. 108

3.39 Photograph and SEM images of CdTe NW assembly formed via vacuum filtration method. 110

3.40 SEM images of CdTe NW assembly showing the cross-sectional view of the NW assembly. 110

3.41 PbSe NC/MEH-PPV composite assembly samples after top metal contact deposition. 111

4.1 Schematic illustration of the NC assembly bounded by metal contacts. 114

4.2 Current-voltage characteristics of CdTe NC assembly drop-cast on the metal substrate. 115

4.3 Energy spectrum of Am-241 alpha source obtained from a drop-cast CdTe NC assembly, with an aluminum contact. 116

4.4 I-V curves of CdTe NC assembly formed by LBL dip-coating on Al-evaporated substrate. 117

4.5 The alpha signal pulse derived from the Au/CdTe NC/In LBL assembly. 118

4.6 The alpha signal pulse derived from a Al/CdTe NC/Pt LBL assembly. 119

4.7 Pulse height distribution derived from ∼250 nm CdTe NC detector operating in transmission mode. 119

4.8 Gamma response from the Al/CdTe NC/Pt assembly deposited with LBL method. 120

4.9 CdTe NW assemblies after the metal deposition and cutting 122

4.10 A photography of CdTe NW sample in the testing box. 122

4.11 Particle track simulation by SRIM and the transmitted energy of alpha particle emitted from the Am-241 source. 124

4.12 Current-voltage (I-V) characteristic curves measured from Spot 1 of Fig. 4.10 of the CdTe nanowire assembly with Au/In contacts. . . . 126

4.13 Current-voltage (I-V) characteristic curves measured from Spot 3 of Fig. 4.10 of the CdTe nanowire assembly with Au/In contacts. . . . 127

4.14 Current-voltage (I-V) characteristic curves measured from Spot 4 of Fig. 4.10 of the CdTe nanowire assembly with Au/In contacts. . . . 127

4.15 Spectral response of the CdTe NW sample, Spot 1 (big spot) to the Am-241 alpha source. 129

4.16 Spectral response of the CdTe NW sample, Spot 4 (small spot) to the Am-241 alpha source. 130

4.17 Spectral response of the CdTe NW sample to the Cs-137 gamma source, compared with the source-free background spectrum measured for the same amount of time. 131

4.18 Current-voltage characteristics of PbSe NC assembly drop-cast on the metal substrate. 132

4.19 Current-voltage characteristics of PbSe NC assembly drop-cast as shown in Fig. 3.23. 132

4.20 Summary of spin-cast NC detector samples, coordinated by OA capping ligands. 133

4.21 I-V curves of drop-cast PbS NC assembly investigated at two different regions. 136

4.22 I-V curves of slide-cast sample with 50 layers of EDT treatment and 20 layers of hydrazine sandwiched by Al and Au contact. 137

4.23 Preamplifier and amplifier signal from the slide-cast PbS NC assembly, induced by the alpha particle emitted from Am-241 source. . . 138

4.24 Pulse height spectra for alpha particles acquired in various bias configurations from the PbS NC sample. 138

4.25 Alpha spectra collected for 10 min. and 1 hour compared with the background noise. 140

4.26 Gamma ray responses of the PbS NC assembly 141

4.27 Preamplifier and amplifier signal from the dip-coated PbS NC assembly, induced by the alpha particle emitted from Am-241 source. . . 142

4.28 Dip-coated sample with 50 layers of PbS NC with hydrazine treatment sandwiched by Pt and In contact. 142

4.29 Summary of polymer-conjugated PbSe NC assembly detectors drop-cast and the assessment. 144

4.30 Schematic of nuclear electronics, and the resulting preamplifier and shaping amplifier signal from the NC composite assembly. 145

4.31 Pulse height spectrum obtained from "weak-response" samples, as a response to alpha particles. 146

4.32 Summary of polymer-conjugated detectors spin-cast and the assessment. 147

4.33 The pulse height distribution of an Am-241 alpha source at various bias voltages. 148

4.34 Comparison of the preamplifier and the shaping amplifier waveforms obtained from two different spin-cast NC blended composites. . . . 148

4.35 The charge-sensitive preamplifier signal derived from a silicon PIN and PbSe NC detector. 150

4.36 Schematic diagram and the result of the PbSe NC assembly with a blended structure. 151

4.37 The gamma-ray spectrum derived from a Ba-133 source. 152

4.38 Schematics of a silicon PIN and a PbSe NC detector and their different responses to the alpha particle impingement. 154

4.39 Typical pulses and the corresponding pulse height distribution obtained from the star-shaped PbSe NC blended assembly. 155

4.40 The pulse height distribution response of the PbSe NC blended sample to the Cs-137 gamma source. 156

4.41 Energy spectrum derived from Ba-133 gamma-rays and Am-241 alpha particles. 158

4.42 Spectral comparison of Ba-133 spectrum between existing radiation detectors and PbSe NC blended sample. 161

4.43 Temporal variation in the 356.02 keV peak derived from Ba-133, for the star-shaped NC PbSe detector. 162

5.1 Comparison of background noise fluctuation in different measurement environment. 168

A.1 Configuration table and images of NC composite assemblies with various parameters in the fabrication. 174

A.2 Electron micrographs of the NC assembly and particles. 176

A.3 Typical geometry for a PbSe quantum dot separated by a single link of the surfactant. 177

A.4 Schematic of the simulation geometry and the simulated spectra of Ba-133 from bulk and NC composite of PbSe. 178

A.5 Contributions from each event type and interactions with each element in the simulated spectra. 181

A.6 X-ray escape peak contributions from major gamma emissions. . . . 185

A.7 Gaussian broadened energy spectra of Ba-133 simulated for PbSe NC/p-MEH-PPV assembly of various thicknesses. 187

A.8 The Ba-133 energy spectra simulated for 20 μm-thick assembly. . . 188

A.9 The ratio of the Pb $L_{\alpha 1}$ single escape peak to its full energy peak for various thicknesses. 189

A.10 The ratio of the Pb $L_{\alpha 1}$ single escape peak to its full energy peak for various thicknesses. 190

A.11 Diagram of the PbSe NC composite detector geometry modeled. . . 191

B.1 Illustration of 3 different types of substrates for the NC assembly deposition. 193

B.2 Schematic of Si wafer-based NC assembly substrate fabrication procedure. 194

B.3 Schematic of glass wafer-based NC assembly substrate fabrication procedure. 195

B.4 Glass wafer-based NC assembly substrate with Al and Au bottom contacts. 196

B.5 Cross-sectional view of the glass-based substrate. 197

LIST OF TABLES

Table

3.1 Synthesis of PbSe NC at various reaction conditions. 67

3.2 Synthesis of PbS NC at various reaction conditions. 82

3.3 Various synthesis conditions for PbSe NC samples. 86

A.1 Gammas emitted from Ba-133. 179

LIST OF APPENDICES

Appendix

A. MCNP Simulation of Radiation Responses 173

B. Fabrication of Nanocrystal Assembly Substrate 192

LIST OF ABBREVIATIONS

AR Auger Recombination

BA Butylamine

BCC Body Centered Cubic

CL Cathodoluminescence

CM Carrier Multiplication

CZT Cadmium Zinc Telluride – $Cd_{0.9}Zn_{0.1}Te$

DIP Di-isobutyl-phosphine

DPE Diphenyl Ether

EA Electron Affinity

ED Electron Diffraction

EDS Energy Dispersive Spectroscopy

EDT 1,2-Ethanedithiol

EMA Effective Mass Approximation

FCC Face Centered Cubic

FWHM Full Width at Half Maximum

HOMO-LUMO Highest Occupied Molecular Orbital and Lowest Unoccupied Molecular Orbital

HPGe Hyper Purity Germanium

HRTEM High Resolution Transmission Electron Microscope (Micrograph)

II Impact Ionization

IP Ionization Potential

LED Light Emitting Diode

LBL Layer-by-Layer

MBE Melecular Beam Epitaxy

MEG Multiple Exciton Generation

MEH-PPV Poly[2-methoxy-5-(2-ethylhexyloxy)-1,4-phenylenevinylene]

MOCVD Metal-organic Chemical Vapor Deposition

MO-LCAO Molecular Orbitals as Linear Combinations of Atomic Orbitals

NC Nanocrystalline, Nanocrystal

NP Nanoparticle

NW Nanowire

OA Oleic Acid

ODE Octadecene

PDF Powder Diffraction File

PL Photoluminescence

QD Quantum Dot

XRD X-Ray Diffraction

SC Simple Cubic

SCL Space Charge Limited

SEM Scanning Electron Microscope (Micrograph)

TEM Transmission Electron Microscope (Micrograph)

TFT Thin Film Transistor

TGA Thioglycolic Acid

TMS Bis(trimethylsilyl)sulfide

TOP Trioctylphosphine

VLS Vapor-liquid-solid

ABSTRACT

Nanocrystalline Semiconductor
Nuclear Radiation Detectors

by

Geehyun Kim

Chair: David K. Wehe / Mark D. Hammig

The demand for precise and efficient nuclear radiation detection has significantly increased, especially in many scientific research fields as well as homeland security and medical imaging applications. The utilization of a quantum-dot-based semiconductor detector can, in principle, transform the capabilities of radiation detectors by yielding a high-performance detector via a low-cost solution-based fabrication modality. Nanocrystalline semiconductor (Nanocrystal, NC) materials exhibit exploitable properties – such as tunable energy band gap, and charge carrier multiplication – which arise due to the strong quantum confinement effect. If highly uniform multiplicities of excitons can be developed across macroscopic NC samples, then one can potentially quench the statistical counting noise associated with charge carrier creation in the bulk material.

Based on the favorable features of NC materials for their application to the detection of ionizing radiation, the NC approach, with a primary focus on the high atomic number and density materials (PbS, PbSe and CdTe), was investigated as a means

to maximize the charge creation and minimize the uncertainty in that conversion. NC particles of different size and shape were synthesized by changing the reaction conditions, and their physical and opto-electric properties were investigated.

Close-packed NC assemblies of cadmium and lead chalcogenides were formed by drop-, slide-, spin-casting or dip-coating NC dispersions on various metal contacts. Current-voltage (I-V) characteristics of each NC assembly were studied to evaluate its properties as an NC-assembly diode, as a function of the opto-electric properties of the NC particles, metal contacts, and the physiochemical property of the NC assembly. The responses of the NC assemblies toward radiation sources were studied via alpha particle impingement from an Am-241 source, and the highest energy-resolution samples exhibited a gamma-ray response that was comparable or better than existing semiconductor materials, including high-purity germanium and cadmium-zinc-telluride. The viability of using NC materials as a basis for the detection of ionizing radiation is assessed and empirical challenges are discussed.

In short, this research focuses on fabricating nuclear radiation detectors out of nanocrystalline semiconductors via a solution-based approach. Various recipes and the subsequent electrical results for the NC assembly samples will be discussed, the main attention being paid to the enhancement of the charge carrier transport properties of the NC assembly.

CHAPTER I

Introduction

Instrumental aspects of nuclear science and technology have served as a core technology for monitoring the operation and assuring the safety of nuclear reactors, as well as providing fundamental measurements in nuclear physics. Moreover, the significance of radiation detection has become more acute with the effort in developing advanced technologies, that include: a) fast breeder reactors (FBR), b) neutron source facilities using fast and cold neutrons, and c) high energy beam facilities based on accelerators. Increasing threats of terrorism and the resulting necessity of precise dangerous-material detection technology, and the need for continual improvement in medical imaging instruments, also provide considerable motivation for the research in detection and measurement of nuclear radiation.

Existing methods to detect and measure ionizing radiation are based on a) gas-filled detectors, b) single crystal and liquid scintillators, or c) semiconductor materials. The essence of radiation detection and measurement technology is sensing the non-equilibrium charge states induced in the interaction media. Thus, either charges, in the form of electron-ion or electron-hole pairs, can be sensed by their effects on the electric field created by the surrounding device architecture, or the light that accompanies the radiative-recombination of those charges, can be monitored using scintillation photon detectors. The technology has been well-developed and has de-

livered adequate performance for the recent century after the discovery of ionizing radiation either through its conversion to charges or photons. However, high performance, low cost sensors and imagers are unavailable. The reason for this is either that: a) the underlying material cost is high (typical for semiconductors), b) the low-cost material has a poor information-conversion efficiency (typical for scintillators), or c) the implementation of the technology poses demanding engineering challenges (typical for advanced methods such as micro-calorimeters and mechanical detectors). If one wishes to have the ubiquitous deployment of radiation sensors, it is necessary to develop detectors that can guarantee high detection efficiency, free from the logistical burdens (e.g., HPGe detector with liquid nitrogen dewar – room temperature operation is necessary), and low fabrication cost. More importantly, if high resolution imaging of the radiation field is to be accomplished, then one prefers a material that makes a highly accurate conversion of the particle's energy into the information carriers in the detection media [1].

In this research, we explored an approach to achieve optimal detector performance by controlling the basic charge-creation mechanisms and charge-transport in solid state devices, based on probing the physics in novel semiconductor materials. Nanocrystalline semiconductor (Nanocrystal, NC) materials provide an attractive material basis upon which to develop optoelectronic devices because they present a means of controlling the charge and phonon dynamics via geometric control of the colloidal solid. Especially, dramatic suppression of the phonon-assisted loss-processes has given promises of very efficient conversion of incident particle into the information carriers (charge or light) which is, in principle, only limited by the energy conservation.

There are two main approaches in utilization of nanostructured media for ionizing radiation detection: 1) nanoscintillators and 2) NC assembly as a semiconductor device. The dominant modality currently being investigated by the radiation-detection

community consists of composite arrays of nanoparticles that scintillate upon their excitation. The physics motivation is that in comparison to single crystalline materials, nanostructured scintillators exhibit more rapid and enhanced light emission due to the suppression of non-radiative loss processes, which yields higher imaging performance in radiation detection [1]. Nanoscintillators consisting of lead-iodide [2], rare-earth-doped fluorides, such as CaF_2(Eu), CeF_3 and LaF_2(Eu) [3, 4], and rare-earth oxides, such as $LuBO_3$ [5] are among many other materials currently being studied, many exhibiting accelerated decay responses and high light conversion efficiency on a nanoparticle basis. Development of nanoscintillators is usually conducted through embedding scintillating nanoparticles into transparent light propagating media, such as organic scintillators. Here, nanoparticles act as the main interaction media with incident radiation and the scintillation photon emitted by the scintillating nanoparticle scatters through the matrix material as governed by Rayleigh scattering [3]. A slightly different approach is attempted by utilizing a scintillating NC assembly as an interaction and light propagating media analogous to single crystal scintillator.

However, the main challenge presented by both approaches is the optical self-absorption in the nanoparticles, the matrix, and the innumerable interfaces as the photons meander their way to the readout surface. In addition, a recent study on an ultrafast cathodoluminescence (CL) experiment on cadmium salt NC assembly shows efficient charged- and multi-exciton generation phenomena risen by 20 keV electron, instead of enhanced excitonic emission from the NC [6]. This has given unfavorable results for application of NC to nanoscintillators. To date, no nanocrystalline scintillator detector has exhibited comparable characteristics to the best single-crystal media, whether composed of NaI(Tl) or brighter scintillators such as $LaBr_3$(Ce). More to the point, one doesn't anticipate that an optimized light-emission media will ever produce a greater number of information carriers than a semiconductor equivalent because of the losses associated with converting the charge into scintillation light –

and back again, at the photocathode or photodiode readout.

The approach made in this research is by employing NC assembly as a semiconductor composite. This is one of the first approaches for studying NCs, called "quantum dots," as a material basis for nuclear radiation detectors. The quantum-dot-based semiconductor detector is expected to revolutionize the capabilities of radiation imaging instruments by yielding a high-performance detector via a low-cost solution-based fabrication modality, if one can overcome the following expected challenges: a) charge loss during the slowing-down of the charged-particle in the inactive matrix, b) charge trapping during subsequent electron and hole transport, and c) small detector volumes. [1, 7, 8]. Colloidal NC dispersions of cadmium chalcogenides and lead chalcogenides were chemically synthesized and deposited onto metal contact evaporated substrates to create an NC assembly. Then, top metal contacts were evaporated onto the assembly, followed by electrical property characterization. Finally, the response of the material to radiation impingement was investigated using alpha and gamma sources.

To summarize, two most important keywords in this dissertation are: *Nanocrystal (NC)* and *solution-based process*. First, this research explores various NC materials' potential for ionizing radiation detector application as opposed to the bulk semiconductor material. There have been extensive developments on quantum dot based devices in many applications; including solar cells [9–17], FETs [18], LEDs [19–21], and photodiodes [17, 22, 23]. However, those devices were mainly formed within the size dimension of approximate mean free path range of the charge carriers (a few hundred nanometers) in the NC assembly. The nuclear radiation detector application is another challenge in making a macroscopic device of much larger dimension, based on the quantum dot material. Second, it is also an attempt at the solution-based processing approach as opposed to the prevalent single-crystal-based approach in device fabrication. This may be an unusual attempt especially in the field of radiation detec-

tion and measurement; however, solution-based processes are often popularly used in such opto-electric devices as LEDs [24], light sensors [25, 26] and solar cells[16, 27–29] using organic semiconductors. Even in the field of radiation detector development, there has been several attempts at adopting a solution-based processing method, using polymer-based organic semiconductor materials [30]. The biggest challenge in this method is attaining a high degree of homogeneity of the assembly, and mitigating the inevitable colloidal defects that accumulate as a greater number of layers are cast onto the sample; thus, it is hard to achieve efficient charge carrier conductivity within the material. If one can develop a solution-processed device that can order nanoparticles comparable to the degree that single crystalline devices order atoms, then, there is great economical advantage for the former method.

In this dissertation, I will discuss various fabrication procedures and following results for the NC assembly samples that I have attempted to develop as a nuclear radiation detector. The effort was mainly focused on the enhancement of the charge carrier transport properties of the NC assembly. In the theory section (Chap. II), I will summarize fundamentals on unique optical properties of NCs (2.1) in association with the motivation for the nuclear radiation detector application (2.2). This will connect many other disciplines to nuclear engineering and radiological sciences, which represents the major portion of the audience for this dissertation. Then I will discuss the design parameters and challenges raised by the solution-based processing (2.3). In the experimental section (Chap. III), I will describe various recipes and methods used for the NC synthesis (3.1), characterization (3.2), and assembly fabrication (3.3), efforts related to enhancing the charge transport properties in the NC assembly. In the results section (Chap. IV), I will present results I have obtained from the NC assembly detector samples, based on cadmium chalcogenide and lead chalcogenide materials, built with diversified fabrication methods and NC layer arrangements. Most importantly, in the conclusion section (Chap. V), I will make several suggestions

for future development directions on NC assembly detectors by launching the idea of "NC Assembly Radiation Detectors."

CHAPTER II

Nanocrystalline Semiconductor (Nanocrystal, NC) "Quantum Dots (QD)"

In the NC realm, whose size scale generally ranges from $\sim 10^2$ to $\sim 10^5$ atoms per particle, the wave functions of the electron-hole (e-h) pairs in the semiconductor are strongly confined if the diameter of the particles are substantially smaller than the de Broglie wavelength and the Bohr radius of the excitons in the bulk semiconductor material. The energy state density of excitons is discretized and unique size-dependent optoelectronic material properties of the NCs, such as tunable energy band-gap, can be developed. The strong quantum confinement effect gives rise to carrier multiplication (CM) [14, 31], which is the efficient direct photogeneration of multiple electron-hole pairs from a single incident photon by greatly enhancing carrier-carrier interactions [32, 33]. These possibilities have been investigated for solar energy conversion, with the goal of achieving quantum efficiencies limited only by energy conservation [11, 13, 14, 31]. This also provides an important motivation for the radiation detector development by mitigating the statistical noise associated with charge carrier creation process. In this chapter, novel properties of NCs will be introduced with consequent motivation for the ionizing radiation detector application. Then, dimensional constraints and expected challenges in the fabrication process will be discussed.

2.1 Optical Properties of Nanocrystal

In this section, I will introduce the basic concept of NCs for the wide spectrum of readership for this dissertation, from diverse disciplines. It is worth covering conceptual fundamentals so that everyone can grasp some basic ideas about the novel properties of NCs and how they are developed.

2.1.1 Two Approaches

In the theoretical consideration of nanocrystalline semiconductors, there are mainly two approaches to explaining the major properties of NC – top-to-bottom (particle-in-a-box approximation) and bottom-to-top (quantum chemistry). The former is an extension of the effective mass approximation (EMA) from solid state physics towards spatially confined structures for the quasiparticle. Here, absorption and emission of energy by a photon in the electron subsystem is described as elementary excitations of quasiparticles (excitons) in the NC. NCs are approximated as three dimensional potential boxes where quasiparticles are confined; thus, energy states are quantized like a particle in a box problem in quantum mechanics. Therefore, the problem connected with NCs can be simplified to a quantum mechanics form and approaches and techniques developed for other quantum systems become applicable to the NC problem. Notably, the electronic properties of NC on the way from the crystal-like to the cluster-like behavior can be successfully explained within the framework of particle-in-a-box approximation of QDs using the EMA. Size-dependent features due to the three-dimensional spatial confinement of quasiparticles, such as the blue shift of the $1S_e$-$1S_h$ transition with decreasing particle size, for instance, are better explained with this method. However, this approach cannot provide a sufficient description for smaller sized NCs, namely particles smaller than 2 nm, that contain fewer than 1000 atoms in total per particle. Corrections such as introducing an empirical pseudo-potential must be made to the problem.

Another approach via molecular quantum mechanics, often referred to as quantum chemistry, is based on considering NCs as large molecules. This approach reveals the development of crystal-like properties of materials starting from the atomic and molecular level, an example of which is shown in the schematic in Fig. 2.1 [34]. In addition, quantum chemistry, in particular, provides useful information on properties of a single-electron energy structure determined by the cluster configuration. It takes into consideration kinetic energies of all electrons and nuclei, as well as potential energies of attractive and repulsive interactions between electrons, nuclei, and the electron-nucleus interaction. Therefore, the calculation sensitively depends on a large number of parameters involving the particular number of atoms and specific spatial configurations of atoms in the NC. Due to the inherent complexity of the problem which requires demanding computational capacity and time, the quantum-chemical approaches are essentially based on numerical analysis with several assumptions and approximations – e.g., the Born-Oppenheimer (or adiabatic) approximation and the molecular orbitals as linear combinations of atomic orbitals (MO-LCAO), the so-called tight-binding approximation. Semi-empirical techniques (Hückel techniques) are also developed to simplify the calculations by adopting some experimental values and this provides better agreement with observable energies. However, this approach is often applicable for small clusters only and does not provide functional relationships between the number of atoms in a cluster and its electronic properties [34, 35].

In the discussion of NC, we can consider the crystal lattice constant, a_L and the exciton Bohr radius, $a_{B_{exc}}$ as two key parameters to characterize the optical properties of NCs. These parameters provide a clue about the size range of the NCs where each approach becomes more descriptively applicable. If the size of a NC is comparable to the lattice constant (a_L), the particle presents more molecular or cluster-like properties represented by the absence of a monotonic dependence of the optical transition energies and probabilities on number of atoms; that is, size-dependent features

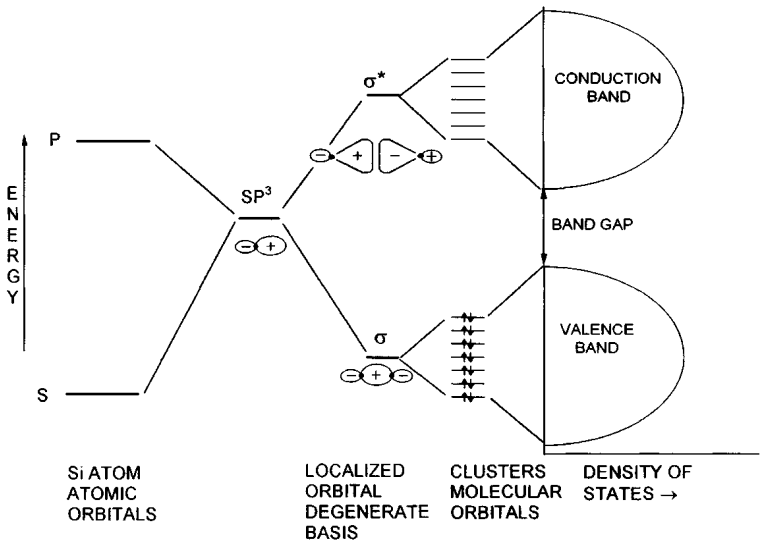

Figure 2.1: Evolution of silicon atomic orbitals into crystal energy bands; Starting from sp^3-hybridized Si atoms to bond orbitals, which form molecular orbitals and finally develop into conduction and valence bands [34].

become ambiguous, and the size of the cluster can no longer be considered as a characteristic factor. In this range, the quantum chemical approach with the specific number of atoms and configuration will provide an accurate prediction for the features of a particle. If the particle size of an NC is much larger than a_L, but considerably smaller than a typical photonic wavelength range, one can apply the particle-in-a-box model with the EMA to the description of the NC. The EMA approach will predict the evolution of size-dependent optical properties of the NC. This specific range can be divided again into two subranges to provide interpretation of size-dependent properties in terms of: a) electron and hole strongly confined in the particle (particle size $a \ll a_{B_{exc}}$) , and b) quantized center-of-mass motions of a hydrogen-like exciton ($a \geq a_{B_{exc}}$). Both approaches – EMA and quantum chemistry – smoothly converge into one another around $a \approx a_{B_{exc}}$. In the following section, I would like to pay special attention to the top-to-bottom approach to show the size-dependent properties of NC appearing in a strong confinement region.

As the size of NC reaches the range of the photonic wavelength, on the order of

100 nm, one cannot exclude the optical coupling phenomena related to the photonic absorption and scattering; such as resonant optical transitions and the photon confinement effect due to the exciton-photon coupling. Therefore, a new quasiparticle concept of *polariton* must be introduced to interpret light absorption and propagation behavior within the particle. This range is often referred to as polaritonic range, where many interesting phenomena of photonic crystals will appear [35].

2.1.2 Size Dependent Properties of Nanocrystal (NC)

As was mentioned previously, approximating spatial confinement of quasiparticles in NC as a particle-in-a-box problem based on the EMA would present size-dependent optical properties of NCs. Here, I will conceptually show the thought process of the idea step by step. Starting from the very basic principles of quantum mechanics, the concept of quasiparticles and effective mass approximation in condensed matter physics will be introduced and combined with the particle-in-a-box problem in order to schematize the quantum confinement effect of the quasiparticle (exciton) in an NC. Finally, size-dependent opto-electrical properties of NCs will be conceptually manifested and more detailed approaches and treatments for the problem will be briefly introduced.

2.1.2.1 Assorted Concepts from Quantum Mechanics

The optical properties of a material are mainly governed by the state of electrons around the atom. Based on the wave-like motion of an electron by wave-particle duality, behavior of the electron can be described by the wave equation. The wave function, $\Psi(\mathbf{r}, t)$, provides a probability amplitude of a quantum state of the particle, and it contains information about various measurable properties – such as the position, momentum and energy of the particle. The wave function can be obtained by solving the wave equation (Schrödinger equation) for the system, and the square

of the wave amplitude, $|\Psi(\mathbf{r},t)|^2$, gives the probability density function for a certain measurable property of the particle. So, let's start from the Schrödinger equation:

$$i\hbar\frac{\partial\Psi}{\partial t} = \hat{H}\Psi. \tag{2.1}$$

This is the general form of the time-dependent Schrödinger equation. This equation describes how the quantum state of a physical system changes with time. $\hat{H}$, here, is the Hamiltonian operator, and this gives the total energy of the wavefunction which is the sum of the kinetic and potential energy. The non-relativistic version of the Schrödinger equation describing a single particle in an electric field is shown as:

$$i\hbar\frac{\partial\Psi}{\partial t} = \left[-\frac{\hbar^2}{2m}\nabla^2 + V\right]\Psi. \tag{2.2}$$

In the case of a time-independent Hamiltonian, i.e., if it is not an explicit function of time, the equation can be separated into spatial terms and the temporal term. This will simplify the equation into an eigenvalue problem calculating the energy eigenvalue E of the particle in stationary states (orbitals), which is the time-independent Schrödinger equation [36]:

$$\hat{H}\psi = E\psi. \tag{2.3}$$

Here,

$$\hat{H} = -\frac{\hbar^2}{2m}\nabla^2 + V(\mathbf{r},t), \tag{2.4a}$$

$$\Psi(\mathbf{r},t) = \psi(r)e^{-iEt/\hbar}. \tag{2.4b}$$

The most common example of quantum mechanics is an infinite potential well problem in one dimensional space. The wavefunction of a particle confined in an

infinitely high square well potential can be calculated analytically, and the energy eigenvalue of the state can be calculated accordingly.

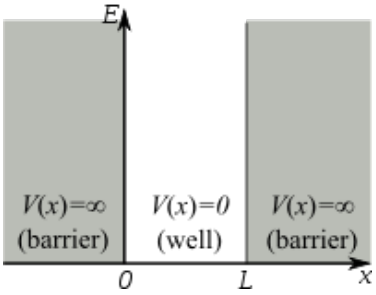

The potential energy of the 1-D square well is,

$$V(x) = \begin{cases} 0, & (0 < x < L), \\ \infty, & \text{otherwise.} \end{cases}$$

The Schrödinger equation in 1-D with potential energy $V(x)$ is shown as:

$$\mathrm{i}\hbar\frac{\partial}{\partial t}\Psi(x,t) = -\frac{\hbar^2}{2m}\frac{\partial^2}{\partial x^2}\Psi(x,t) + V(x)\Psi(x,t). \tag{2.5}$$

The general solution of the 1-D Schrödinger equation is known as:

$$\Psi(x,t) = [A\sin(kx) + B\cos(kx)]\mathrm{e}^{-\mathrm{i}\omega t}. \tag{2.6}$$

Applying boundary conditions for the infinite potential well gives the wavefunction:

$$\Psi_n(x,t) = \begin{cases} \sqrt{\frac{2}{L}}\sin(k_n x)\mathrm{e}^{-\mathrm{i}\omega_n t}, & (0 < x < L), \\ 0, & \text{otherwise.} \end{cases} \tag{2.7a}$$

$$k_n = \frac{n\pi}{L}, \quad \text{where} \quad n = \{1, 2, 3, 4, \ldots\}. \tag{2.7b}$$

And the energy eignenvalue for each mode is as follows:

$$E_n = \hbar\omega_n = \frac{\hbar^2 k_n^2}{2m} = \frac{n^2\hbar^2\pi^2}{2mL^2}. \tag{2.8}$$

In a three dimensional infinite square well potential, one can obtain a set of stationary states of a particle in a box as shown in Eq. 2.10, from the general solution

(Eq. 2.9) to the time-dependent Schrödinger equation (Eq. 2.2):

$$\Psi(\mathbf{r},t) = \sum c_n \psi_n(\mathbf{r}) e^{-iE_n t/\hbar}. \tag{2.9}$$

where, $\psi_n(\mathbf{r})$ is a solution of the time independent Schrödinger equation:

$$\psi_n(\mathbf{r}) = \psi_{n_x,n_y,n_z}(x,y,z) = \sqrt{\frac{8}{L_x L_y L_z}} \sin\left(k_{n_x} x\right) \sin\left(k_{n_y} y\right) \sin\left(k_{n_z} z\right), \tag{2.10}$$

and the energy eigenvalue in the 3-D infinite potential well is:

$$E_{n_x,n_y,n_z} = \frac{\hbar^2 k^2_{n_x,n_y,n_z}}{2m} \tag{2.11a}$$

$$\begin{aligned} \mathbf{k}_{\mathbf{n_x},\mathbf{n_y},\mathbf{n_z}} &= k_{n_x}\hat{\mathbf{x}} + k_{n_y}\hat{\mathbf{y}} + k_{n_z}\hat{\mathbf{z}}, \\ &= \frac{n_x \pi}{L_x}\hat{\mathbf{x}} + \frac{n_y \pi}{L_y}\hat{\mathbf{y}} + \frac{n_z \pi}{L_z}\hat{\mathbf{z}}. \end{aligned} \tag{2.11b}$$

Since most of the NCs can be approximated as nearly-spherical-shaped particles, it is easier to depict the potential encountered by quasiparticles in a NC by assuming a spherically symmetric potential. In order to describe the behavior of a particle in a sphere, one may write the stationary part of the wavefunction $\psi(\mathbf{r})$ in terms of the spherical coordinate r, θ, ϕ. Since the potential is a function of the distance from the origin only, by definition, one can separate the wavefunction into the radial portion and the angular portion using the separation of variables method. The spherical polar angles θ and ϕ can be put together as spherical harmonics. Therefore, eigenfunctions for the spherically symmetric potential can be written as following:

$$\psi(r,\theta,\phi) = R(r)\Theta(\theta)\Phi(\phi) = R(r)Y_{lm}(\theta,\phi). \tag{2.12}$$

The Hamiltonian in the spherically symmetric potential can be described as:

$$\hat{H} = \frac{\hat{p}^2}{2m_0} + V(r). \tag{2.13a}$$

where, kinetic energy term can be written as:

$$\frac{\hat{p}^2}{2m_0} = -\frac{\hbar^2}{2m_0}\nabla^2 = -\frac{\hbar^2}{2m_0\, r^2}\left[\frac{\partial}{\partial r}\Big(r^2\frac{\partial}{\partial r}\Big) - \hat{l}^2\right]. \tag{2.13b}$$

And spherical harmonics, by definition, satisfy the following condition about $\hat{l}^2$:

$$\begin{aligned}\hat{l}^2 Y_{lm}(\theta,\phi) &\equiv \left\{-\frac{1}{\sin^2\theta}\left[\sin\theta\frac{\partial}{\partial\theta}\Big(\sin\theta\frac{\partial}{\partial\theta}\Big) + \frac{\partial^2}{\partial\phi^2}\right]\right\} Y_{lm}(\theta,\phi) \\ &= l(l+1)Y_{lm}(\theta,\phi).\end{aligned} \tag{2.13c}$$

Here, we have used particle mass "m_0" instead of "m" from above, to avoid confusion with the quantum number m of the spherical harmonics. The time-independent Schrödinger equation (Eq. 2.3) can be simplified into a radial equation and restated as following:

$$\left\{-\frac{\hbar^2}{2m_0 r^2}\frac{d}{dr}\left(r^2\frac{d}{dr}\right) + \frac{\hbar^2 l(l+1)}{2m_0 r^2} + V(r)\right\} R(r) = ER(r). \tag{2.14}$$

This can be further reduced into another simple form of the 1-D Schrödinger equation:

$$-\frac{\hbar^2}{2m_0}\frac{d^2u(r)}{dr^2} + V_{\text{eff}}(r)u(r) = Eu(r), \tag{2.15a}$$

with the change of variable and the introduction of the effective potential that includes

the centrifugal term,

$$u(r) \stackrel{\text{def}}{=} rR(r), \tag{2.15b}$$

$$k \stackrel{\text{def}}{=} \sqrt{\frac{2m_0E}{\hbar^2}}, \tag{2.15c}$$

$$V_{\text{eff}}(r) = V(r) + \frac{\hbar^2 l(l+1)}{2m_0r^2}. \tag{2.15d}$$

The general solution for the radial equation (Eq. 2.15a) is known to be:

$$u(r) = Arj_l(kr) + Brn_l(kr), \tag{2.16a}$$

where $j_l(x)$ is the spherical Bessel function of order l, and $n_l(x)$ is the spherical Neumann function of order l. They are defined as follows:

$$j_l(x) = (-x)^l \left(\frac{1}{x}\frac{d}{dx}\right)^l \frac{sin\ x}{x}, \tag{2.16b}$$

$$n_l(x) = (-x)^l \left(\frac{1}{x}\frac{d}{dx}\right)^l \frac{cos\ x}{x}. \tag{2.16c}$$

Potential configuration for the infinite spherical well can be defined as:

$$V(r) = \begin{cases} 0, & (r < a), \\ \infty, & (r > a). \end{cases}$$

Applying boundary conditions from the given potential configuration to the problem provides the following wavefunction:

$$\psi_{nlm}(r,\theta,\phi) = A_{nl}\ j_l(\beta_{nl}r/a)\ Y_{lm}(\theta,\phi), \tag{2.17}$$

where β_{nl} is the n^{th} zero of the l^{th} order spherical Bessel function. Thus, $k_{nl} = \beta_{nl}/a$.

The allowed energy states are given by:

$$E_{nl} = \frac{\hbar^2 k_{nl}^2}{2m_0} = \frac{\hbar^2}{2m_0 a^2}\beta_{nl}^2. \tag{2.18}$$

The energy levels of a particle in a spherical well can be represented as a set of energy levels $1s, 1p, 1d, \ldots, 2s, 2p, 2d, \ldots$ which arise due to the spherical symmetry of the potential well. When energy values for $l = 0$ $(1s, 2s, \ldots)$ are calculated, $\beta_{n0} = \pi n$ $(n = 1, 2, 3, \ldots)$, and the energy state value matches that of 1-D infinite square well potential case.

An infinite spherical potential would provide a good approximation for the prediction of the optical property of NCs. However, by introducing the finite barrier potential well to the problem, one can bring even further precision to the calculation. In the case of a particle placed in a finite spherical well, defined as:

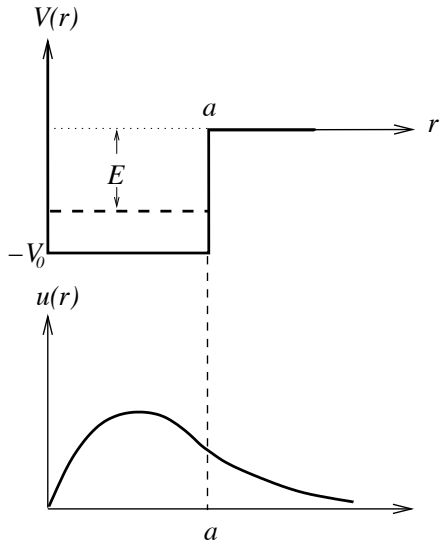

$$V(r) = \begin{cases} -V_0, & (r < a), \\ 0, & (r > a). \end{cases}$$

Radial solutions for bound states can be obtained both inside and outside of the spherical potential, which can be written as following:

$$u_{nl}(r) = \begin{cases} Arj_l(kr), & (r < a), \\ Br(j_l(i\kappa r) + in_l(i\kappa r)), & (r > a). \end{cases} \tag{2.19}$$

where,

$$k \overset{\text{def}}{=} \sqrt{\frac{2m_0(E+V_0)}{\hbar^2}}, \tag{2.20a}$$

$$\kappa \overset{\text{def}}{=} \sqrt{\frac{2m_0E}{\hbar^2}}. \tag{2.20b}$$

In order to meet the boundary condition, solutions in both regions must satisfy

$$-\cot\left(\sqrt{\frac{2m_0(E+V_0)}{\hbar^2}}a\right) = \sqrt{\frac{-E}{V_0+E}}. \tag{2.21}$$

By solving this transcendental equation numerically, one can calculate the allowed energy eigenvalues of the bound state within the spherical potential.

The last example in this section is the hydrogen(-like) atom problem, which consists of a nucleus and an electron. This is a two-particle system with interaction therein through the Coulomb potential $V(r) = -\dfrac{Ze^2}{r}$ (in Gaussian units). Z refers to the charge of the nucleus. Considering the hydrogen atom, which is composed of a proton and an electron, one can let $Z = 1$. The Hamiltonian for this two-particle system can be written as:

$$\hat{H} = -\frac{\hbar^2}{2m_N}\nabla_N^2 - \frac{\hbar^2}{2m_e}\nabla_e^2 - \frac{e^2}{|\mathbf{r}_N - \mathbf{r}_e|}. \tag{2.22}$$

where N and e refer to nucleus and electron respectively. The operation must be performed with respect to each individual coordinate of both particles. To simplify the problem into an integrated motion of the two-particle system, which has its own internal states associated with the relative motion of both particles, we can introduce the center-of-mass system into the discussion. The relative radius vector $\mathbf{r}$ and the

radius vector of the center-of-mass $\mathbf{R}$ can be defined as follows:

$$\mathbf{r} = \mathbf{r}_N - \mathbf{r}_e, \tag{2.23a}$$

$$\mathbf{R} = \frac{m_e\mathbf{r}_e + m_N\mathbf{r}_N}{m_e + m_N}, \tag{2.23b}$$

and the total mass M and the reduced mass μ can be determined as:

$$M = m_e + m_N, \tag{2.24a}$$

$$\mu = \frac{m_e m_N}{m_e + m_N}. \tag{2.24b}$$

Then, the Hamiltonian for the interacting two-particle system (Eq. 2.22) is transformed into the Hamiltonian defined at the center-of-mass:

$$\hat{H} = -\frac{\hbar^2}{2M}\nabla_R^2 - \frac{\hbar^2}{2\mu}\nabla_r^2 - \frac{e^2}{r}. \tag{2.25}$$

Here the Hamiltonian is separated into a Hamiltonian of a free particle with the mass M and a Hamiltonian of another particle with the mass μ in the potential $-e^2/r$. The former describes an infinite motion of the center-of-mass in the two-particle atom, and the latter accounts for the internal states of the two-particle atom system. In order to calculate the allowed energy states of a bound electron in a hydrogen atom, we can assume a heavy, motionless proton located at the origin with a much lighter electron orbiting around it. The Hamiltonian related to the center-of-mass motion can be approximated as negligible by this assumption. The radial equation (Eq. 2.15a) for this Hamiltonian can be written as:

$$-\frac{\hbar^2}{2m_0}\frac{d^2u(r)}{dr^2} + \left[-\frac{e^2}{r} + \frac{\hbar^2 l(l+1)}{2m_0 r^2}\right]u(r) = Eu(r). \tag{2.26}$$

The equation can be solved yielding the allowed energy states of a bound electron in

a hydrogen atom:

$$E_n = -\frac{Ry}{n^2}, \qquad \text{for } E < 0, \tag{2.27a}$$

where, Ry is called the *Rydberg constant*, which corresponds to the ionization energy of the lowest state. This can be written in terms of the Bohr radius, a_B, which roughly represents the most probable distance between the two particles (proton and electron in this case) in its ground state:

$$Ry = \frac{\mu e^4}{2\hbar^2} = \frac{e^2}{2a_B}, \tag{2.27b}$$

$$a_B = \frac{\hbar^2}{\mu e^2}. \tag{2.27c}$$

Throughout this subsection, a few fundamental problems in quantum mechanics were revisited. The problems we have discussed will fundamentalize an important basis for the conceptual consideration of NCs. Namely, the infinite spherical potential will provide the approximate description of an electron and a hole in an NC, whereas the hydrogen atom model will provide a clue about excitons in an NC, as well as in a bulk crystal. One big advantage of the hydrogen atom model, especially, is that it provides a transition from the many-body problem (proton and electron) to the one-body problem by means of the renormalization of mass (reduced mass μ instead of M_0 and m_0) and a differentiation between the collective behavior (the center-of-mass translational motion) and the single-particle motion in a certain effective field. The infinite potential problem can be further refined by introducing a finite potential well, to create a more precise approach for the description [35–38].

2.1.2.2 Effective Mass Approximation

In consideration of the many particle problem, the Hamiltonian for the system composed of N particles can be presented as follows:

$$\hat{H} = \sum_{n=1}^{N} \hat{T}_n + V. \tag{2.28}$$

Here, the potential energy term V, as a general formalism, has to be described in terms of the spatial configuration of the system and time. Therefore,

$$\begin{aligned} \hat{H} &= \sum_{n=1}^{N} \frac{\hat{\mathbf{p}}_n \cdot \hat{\mathbf{p}}_n}{2m_n} + \sum_{n=1}^{N} \frac{\hat{\mathbf{p}}_n \cdot \hat{\mathbf{p}}_n}{2m_n} + V(\mathbf{r}_1, \mathbf{r}_2 \cdots \mathbf{r}_N, t) \\ &= -\frac{\hbar^2}{2} \sum_{n=1}^{N} \frac{1}{m_n} \nabla_n^2 + V(\mathbf{r}_1, \mathbf{r}_2 \cdots \mathbf{r}_N, t). \end{aligned} \tag{2.29}$$

This presents a very complicated many-body problem, since one must consider every interaction between each individual particle, as well as the spatial arrangement of each particle at certain point, in order to determine the potential term. In addition, the kinetic energy term also relies on the specific condition of the potential term. Only if one makes a radical assumption that only non-interacting particles comprise the system, one can express the potential term as a sum of the separate potential energy for each particle. And the problem can be simplified as follows:

$$\begin{aligned} \hat{H} &= -\frac{\hbar^2}{2} \sum_{i=1}^{N} \frac{1}{m_i} \nabla_i^2 + \sum_{i=1}^{N} V_i \\ &= \sum_{i=1}^{N} \left(-\frac{\hbar^2}{2m_i} \nabla_i^2 + V_i \right) = \sum_{i=1}^{N} \hat{H}_i. \end{aligned} \tag{2.30}$$

In a crystal, the periodic arrangement of atoms provides a periodic potential encountered by electrons in the solid. A rigorous approach for the description of particles in the system can be provided by considering the following Hamiltonian,

which involves consideration of: a) the kinetic energy of every electron of mass m_0, b) the kinetic energy of every nucleus of mass M, c) the potential energy of the Coulombic repulsion between electrons, U_1, d) the potential energy of the nuclear-electronic Coulombic attractions, U_2, and e) the potential energy of the internuclear repulsion, U_3 [35]:

$$\hat{H} = -\frac{\hbar^2}{2m_0}\sum_i \nabla_i^2 - \frac{\hbar^2}{2M}\sum_a \nabla_a^2 + \frac{1}{2}\sum_{i\neq j} U_1(\mathbf{r}_i - \mathbf{r}_j) + \sum_{a,i} U_2(\mathbf{r}_i - \mathbf{R}_a) + \frac{1}{2}\sum_{a\neq b} U_3(\mathbf{R}_a - \mathbf{R}_b). \tag{2.31}$$

In Eq. 2.31, $\mathbf{r}$ and $\mathbf{R}$ refer to the radius vectors, and i, j and a, b are the indices for the electron and the nucleus respectively. However, solving the Schrödinger equation with such Hamiltonian that contains $\sim 10^{23}$ terms is impractical; therefore, several approximations need to be made in order to simplify the problem.

The first approximation can be made based on the screening effect of individual atoms; the electrical and optical properties of the crystal are mostly governed by the behavior of the valence electrons of the constituent atoms. Thus, instead of considering the nuclei and each bound electron in the shell, the problem can be simplified by considering the ion core and the valence electrons in the external shell. Under this approximation, electron-electron interactions within the same atom no longer need to be considered, only Coulomb interactions between valence electrons in each atom need to be considered. Thus, the third electron-electron interaction term in the previous equation (Eq. 2.31) can be restated as follows:

$$\frac{1}{2}\sum_{i\neq j} U_1(\mathbf{r}_i - \mathbf{r}_j) = \frac{1}{2}\sum_{i\neq j} \frac{e^2}{|\mathbf{r}_i - \mathbf{r}_j|}. \tag{2.32}$$

The next approximation to be made is the Born-Oppenheimer approximation, also known as the *adiabatic approximation*. This approximation is based on the large

difference in mass between the nucleus (M) and the electron (m_0); thus the nucleus is considered as motionless. The same approximation was applied in the hydrogen atom case (Eq. 2.22) in the previous section. Here, we can consider this problem as one in the simplified system composed of the motionless ion core and valence electrons. As shown previously, the wavefunction becomes separable and thus, the Hamiltonian can be then separated into two groups describing subsystems of ion cores ($\mathbf{R}_a$) and valence electrons ($\mathbf{r}_i$). Each Schrödinger equation is to be solved in their respective coordinates; the electron and the ion. The Schrödinger equation for the electron subsystem in crystal can be written as:

$$-\frac{\hbar^2}{2m_0}\sum_i \nabla_i^2\psi + \frac{1}{2}\sum_{i\neq j}\frac{e^2}{|\mathbf{r}_i-\mathbf{r}_j|}\psi + \sum_{a,i} U_2(\mathbf{r}_i-\mathbf{R}_a) = E_R\psi. \tag{2.33}$$

Then, one can apply the self-consistent field approximation, also known as the *Hartree-Fock method*, a method to determine an eigenfunction and the energy eigenvalue of a many-body quantum system on the basis of the Born-Oppenheimer approximation, the mean-field theory and the variational principle. This method utilizes the *Fock operator*, which is an effective one-particle Hamiltonian consisting of kinetic and potential energy terms under the mean field exerted by all other particles. By iteratively applying eigenfunctions into the calculation of a new Fock operator and optimizing the consequent eigenfunction, one can calculate the self-consistent one-electron orbital and the energy eigenvalue. Thus, Coulombic interactions between valence electrons and ion cores can be effectively described by introducing a periodic potential $U(\mathbf{r})$ that can be adjusted by empirical values in the reiterative process of the calculation. Therefore, it can be dramatically simplified into a single-particle Schrödinger equation:

$$-\frac{\hbar^2}{2m_0}\nabla^2\psi + U(\mathbf{r})\psi = E\psi. \tag{2.34}$$

Bloch's theorem shows that the eigenfunction of the Hamiltonian with a periodic potential is a plane wave modulated by a function with the same periodicity of the crystal lattice, i.e., the periodic potential. Thus, a typical form of wavefunction that satisfies the Schrödinger equation for a particle in the periodic potential appears as shown below:

$$\psi_{\mathbf{k}}(\mathbf{r}) = u_{\mathbf{k}}(\mathbf{r})\ e^{i\mathbf{k}\cdot\mathbf{r}}. \tag{2.35}$$

Several well-known methods – such as the empty lattice approximation (nearly free electron model), the Kronig-Penny model, and the tight binding approximation, for instance – utilize Bloch's theorem to provide a simplified means to describe the periodic potential encountered by electrons in the crystal. Combined with the self-consistent field approximation, the theorem also remarkably simplifies the description of a particle in a solid – electrons subject to the attractive force of the nuclei – approximated by the periodic potential. The state of the particle then can be represented in terms of the quasi-momentum (or crystal momentum) k and $u_{\mathbf{k}}(\mathbf{r})$, which is the periodic function related to the crystal lattice. The energy dispersion relation calculated by the simplified models in the quasi-momentum space show continuous bands separated from each other by forbidden energy gaps; this provides the basis for the well-known concept of conduction band (E_C) and valence band (E_V) separated by the energy band gap (E_g).

In the vicinity of extrema in the energy band, the energy dispersion relation can be approximated as a quadratic form of the quasi-momentum k, which is used to describe the motion of a free particle. On this basis, we can now introduce the *"effective mass"* from the following relationship about the energy of a conceptual free particle in the

crystal, described by the quasi-momentum [39]:

$$E(k) = \frac{\hbar^2 k^2}{2m^*(k)}. \tag{2.36}$$

Motion of the charge carrier in a crystal is always subject to the complicated periodic potential created by the constituent atoms in the crystal lattice. The *effective mass approximation (EMA)* attempts to incorporate the effect of atoms in the lattice and allows the carrier to be treated as if it were a free particle only with a different mass. Therefore, the particle's behavior under the circumstances of the electric and magnetic fields or other external forces can be described in terms of the effective mass, with dependence in the direction of motion; thus, the effective mass can be represented as a tensor. However, the effective mass $m^*(k)$ can be often regarded as a constant around the extrema of energy bands, which is highly significant in the discussion of electrical and optical properties of the solid, especially in the semiconductor. Here, the effective mass can be written as:

$$m^* = \hbar^2 \cdot \left[\frac{d^2E}{dk^2}\right]^{-1}. \tag{2.37}$$

Therefore, Eq. 2.34 can be restated in terms of the effective mass:

$$-\frac{\hbar^2}{2m^*}\nabla^2\psi = E\psi. \tag{2.38}$$

This provides a very powerful tool for the calculation of energy eigenvalues and eigenfunctions of particles in the crystal. Combined with the envelope function approximation, one can split the overall potential term encountered by the particle with the slowly-varying envelope function and the periodic function of the crystal lattice; the latter can be embraced by the EMA. Then, one only needs to consider the slowly varying envelope term to calculate the energy eigenvalue, which can be an additional

term to the eigenvalue of a free particle in the vacuum. Here, without the assumption of any external force such as electric field, the particle in the periodic potential can be assumed as a free particle with an effective mass. The eigenfunction $\psi_{\mathbf{k}}(\mathbf{r})$ given by Bloch's theorem can be viewed as modulation of slowly varying plane wave with a function of crystal lattice periodicity. If the energy states (E_0) for the free particle in vacuum (m_0) is known, the energy eigenvalues for the particle in a crystal can be calculated as follows:

$$E = E_0 + E_{env} = E_0 + \frac{\hbar^2 k^2}{2m^*}. \tag{2.39}$$

2.1.2.3 Quasiparticles

Electrical conductivity of a material is governed by the motion of free electrons in the conduction band, which can liberate themselves from their affiliated atoms easily and travel through the crystal lattice. The differences between conductors and insulators are primarily due to the location of the Fermi level with regard to the conduction band and the valence band. Thus, it must be noted that the concept of *"free electron"* in a solid must be distinguished from that in vacuum; it is indeed a conduction electron which should be treated as a different type of non-interacting particle, called a *quasi-particle*, with the charge $-e$, spin 1/2, effective mass m_e^*, and energy determined by the quasi-momentum $\hbar k$. Properties of these particles attribute to the interactions in a many-body system between a large number of nuclei and bound electrons, which is conceptually and empirically considered under the effective mass approximation (EMA). Another type of quasiparticle is defined by the ensemble of electrons in the valence band where an electron is removed. This quasiparticle is called a *hole*, and has the charge of $+e$, spin 1/2, and the effective mass m_h^*. One can also define the Bohr radii for these quasiparticles in terms of their effective masses as an expected size boundary of their existence. In other words, the Bohr radius of a

particle can be also considered as a probable radius for an effective area of interaction when the particle is considered in the many-body system:

$$a_{B_{e,h}} = \frac{\varepsilon \hbar^2}{m^*_{e,h} e^2}. \tag{2.40}$$

Both electrons and holes constitute the elementary excitations of the crystal. Fig. 2.2 shows the schematic presentation of the electron-hole pair creation process by photon absorption, as an external perturbation on the many-body system, in two different diagrams. The creation of an electron-hole pair gives rise to the excited states of the system, which finally becomes stabilized by the opposite process, radiative transition emitting a photon with the band gap energy. According to the energy and momentum conservation,

$$\begin{aligned} \hbar\omega &= E_g + E_{e,kin} + E_{h,kin}, \\ \hbar\mathbf{k} &= \hbar\mathbf{k}_e + \hbar\mathbf{k}_h. \end{aligned} \tag{2.41}$$

Meanwhile, interactions between electrons and holes via the Coulomb potential create a hydrogen-like bound state of an electron-hole pair; this is described by introducing another type of quasiparticle, called the *exciton*. Therefore, one can consider an exciton can be created by photon absorption. An exciton is represented by a Hamiltonian similar to that of hydrogen atom (Eq. 2.22),

$$\hat{H} = -\frac{\hbar^2}{2m^*_e}\nabla^2_e - \frac{\hbar^2}{2m^*_h}\nabla^2_h - \frac{e^2}{\varepsilon|\mathbf{r}_e - \mathbf{r}_h|}. \tag{2.42}$$

Note that masses of the nucleus and the electron is replaced with the effective mass m^*_e and m^*_h, and the dielectric constant ε is not assumed to be 1 any more. Similar to the hydrogen problem, one can also define the *Bohr radius* and the *Rydberg constant*

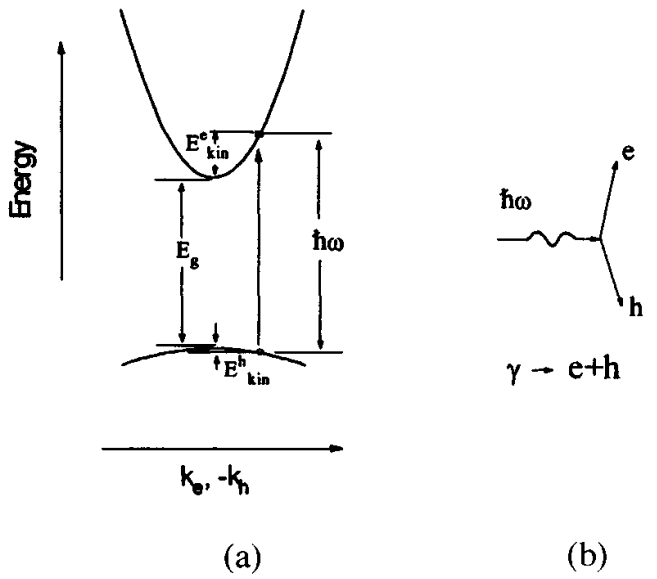

Figure 2.2: An electron-hole pair creation process via photon absorption schematized in (a) the energy dispersion relation in the momentum space and (b) the Feynman diagram [35].

for an exciton:

$$a_{B_{exc}} = \frac{\varepsilon \hbar^2}{\mu^* e^2}, \tag{2.43}$$

$$Ry^* = \frac{e^2}{2\varepsilon a_{B_{exc}}} = \frac{\mu^* e^4}{2\varepsilon^2 \hbar^2}, \tag{2.44}$$

with the total mass M and the reduced mass μ defined in the similar manner:

$$M^* = m_e^* + m_h^*, \tag{2.45a}$$

$$\mu^* = \frac{m_e^* m_h^*}{m_e^* + m_h^*}. \tag{2.45b}$$

The Bohr radius of exciton can be regarded as an estimated length scale for the Coulombic interaction between an electron-hole pair. Typical values of the exciton Bohr radius for the common semiconductor material tend to be significantly larger than that for the hydrogen atom, thus they are in the range of 10-100 Å. Therefore the Rydberg energy tends to be much smaller, falling in the range of 1-100 meV.

There are materials which have relatively larger exciton Bohr radius depending on the effective mass and the dielectric constant. Notably, lead chalcogenides (PbX, X = S, Se, and Te) have the exciton Bohr radii of 20 nm, 46 nm and 50 nm, respectively, which can be substantially larger than the physical size of the nanoparticle, where quantum confinement effect of an exciton within the particle can arise.

The energy eigenstates of an exciton consists of the hydrogen-like internal energy states and the kinetic energy of the translational motion on the basis of the band gap energy. Taking the translational center-of-mass motion of an exciton into consideration, the energy dispersion relation of an exciton can be represented as:

$$E_n(\mathbf{K}) = E_g - \frac{Ry^*}{n^2} + \frac{\hbar^2 \mathbf{K}^2}{2M^*}. \tag{2.46}$$

Here, E_g is the band gap of the material, and the second and third term accounts for the internal and external energy states of the exciton respectively. In case of a photon absorption process involving a negligible momentum, one can observe that the energy state of an exciton is slightly lower than the energy band gap, and this gives rise to the excitonic emission of the semiconductor.

2.1.2.4 Quantum Confinement and Size-dependent Properties

So far, we have covered the basic quantum mechanics problems and a few approximation methods to simplify the many-body problem in the crystal. By a series of approximations, the NC problem can be reduced to the particle-in-a-sphere form (Eq. 2.18). Electrons and holes created by the photoexcitation may then be treated as particles inside a sphere of constant potential. Now the necessary step comes down to: *how can we apply these approaches to the NC problem?* First of all, a NC can be considered as a semiconductor inclusion embedded in an insulating matrix; for example, chemically synthesized colloidal NCs consist of an inorganic core overcoated

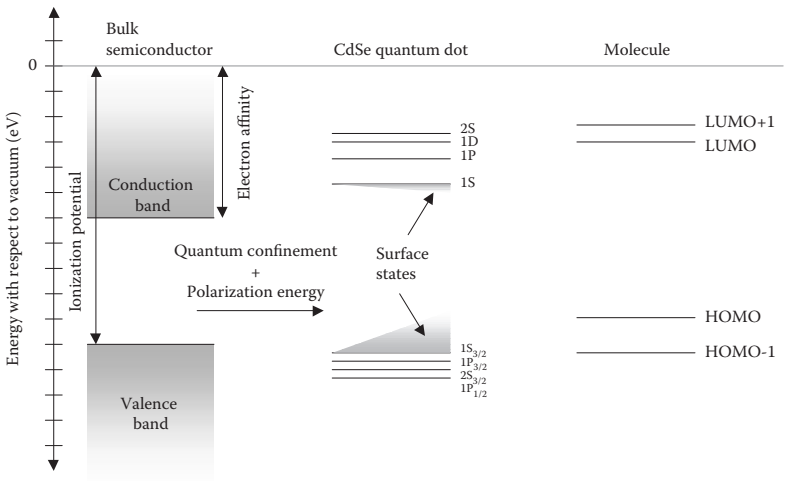

Figure 2.3: Energy-level diagrams comparing the energy bands of a bulk semiconductor crystal, the discrete quantum-confined states in a semiconductor nanocrystal, and the energy levels in a small molecule. Any dangling bonds at the surface of the quantum dot may create mid-gap states that can act as electron- or hole-accepting traps. [33].

with a layer of organic capping ligands which provide electronic and chemical passivation of surface dangling bonds. The potential barrier at the boundaries can be approximated as infinitely high, or, more realistically, it can be modeled as a finite barrier [37, 38].

If the size of the semiconductor structure becomes comparable to or smaller than the natural length scale of quasiparticles, the quasiparticles will experience "restriction" of their motion by the presence of boundaries in the semiconductor structure. The semiconductor structure provides spatial confinement of quasiparticles, which is known as *quantum confinement* and leads to atomic-like optical properties of NCs as the bulk bands become quantized. The energy level of electrons and holes becomes sensitively dependent on the amount of confinement, as do the optical spectra of nanocrystals due to the size of the crystallite. "Quantum dots" often refer to the mesoscopic semiconductor structure where spatial confinement of quasiparticles can exist in all three dimensions. Thus, quantum dots are nanocrystalline semiconductors which typically have the size smaller than 10 nm.

Fig. 2.3 shows the difference in energy level structures between a bulk semiconductor crystal, a quantum dot, and a small molecule. The continuous energy bands of bulk semiconductor become discretized in the quantum-confined NCs, of which energy level structure resembles the highest occupied molecular orbital and lowest unoccupied molecular orbital (HOMO-LUMO) level structures of a molecule. Meanwhile, an ideal QD is realizable only when the electronic states within the dot face a discontinuity at the edge of the material. Due to this, the electron within the dot feels an insurmountable barrier at the edge. When a material is truncated at the surface, the surface atoms have unsatisfied valencies. In order to reduce the surface energy, the surface reconstructs, which leads to energy levels in the forbidden gap of the semiconductor. The electrical and optical properties of the material are degraded by these traps [33].

The analogy of quantum dots to the particle-in-a-box problem as a spatially confined structure of quasiparticles, is enabled by the extension of EMA to the NC structure; i.e., quasiparticles in a quantum dot can be treated as if they have the same properties as in a bulk structure. This approach is reasonable if the size of the NC particle is significantly larger than the unit cell – the lattice spacings of the crystal. This allows the application of the envelope function approximation to the NC problem, of which energy states can be calculated from the envelope function component in addition to the known band gap of the bulk material. Otherwise, the quantum chemistry approach with an explicit number of atoms in calculation will provide a much more precise presentation of the property. In addition, the physical dimension of the NC particle must be comparable to or smaller than the size parameters of constituent quasiparticles in the bulk material, in order to be considered as a quantum box for the quasiparticles.

As was mentioned previously, the amount of confinement of quasiparticles can be considered in terms of their Bohr Radii: a_{B_e}, a_{B_h}, and $a_{B_{exc}}$ as Bohr radii for the

electron, hole and exciton, respectively. When the size of NC is on the same order as that of exciton Bohr radius $a_{B_{exc}}$ ($a > a_{B_e}, a_{B_h}$ and $a \sim a_{B_{exc}}$) quasiparticles in the NC are considered to be in the *weak confinement regime*. In this regime, the quantum confinement effect does not interfere with the relative motion of electron-hole pair; only the center-of-mass motion of the hydrogen-like exciton is quantized in the NC. The energy of an exciton can be represented as follows, using Eq. 2.46 above:

$$E_{nml} = E_g - \frac{Ry^*}{n^2} + \frac{\hbar^2 \beta_{ml}^2}{2M^* a^2}. \tag{2.47}$$

Note that the center-of-mass kinetic energy term for a free exciton is now replaced by the solution for the particle-in-a-sphere problem (Eq. 2.18). This represents the external states of an exciton, which are governed by the center-of-mass motion within the potential barrier due to the quantization given by the NC boundary. The second term accounts for the internal states of the exciton given by the Coulombic interaction between the electron and hole. The lowest state of the exciton energy is shown as:

$$E_{110} = E_g - Ry^* + \frac{\pi^2 \hbar^2}{2M^* a^2}. \tag{2.48}$$

This corresponds to the first excitonic absorption energy of the NC in the weak confinement regime. The minimal energy required to create an unbound (so called, "free", thus conductive) electron-hole pair is

$$E_{ml} = E_g + \frac{\hbar^2 \beta_{ml}^2}{2m_e^* a^2} + \frac{\hbar^2 \beta_{ml}^2}{2m_h^* a^2} = E_g + \frac{\hbar^2 \beta_{ml}^2}{2\mu^* a^2}. \tag{2.49}$$

The relation shows that the energy absorption required to create a conductive electron-hole pair has dependence on the size of the NC (a), however, the dependence turns out to be not significant in the weak confinement regime, where the size of the NC is relatively large.

Strong confinement of electrons and holes within the NC boundary occurs when the size of NC is much smaller than the Bohr radii of quasiparticles ($a < a_{B_e}, a_{B_h}$: thus $a \ll a_{B_{exc}}$). This causes the continuous valence and conduction bands to be collapsed into a ladder of hole and electron levels, respectively (Fig. 2.3). The discrete structure of energy states leads to a discrete absorption spectrum of NCs, which is in contrast to the continuous absorption spectrum above the band gap of the bulk semiconductor.

Due to the dimension scale of the NC being much smaller than the exciton Bohr radius, internally correlated bound states of excitons cannot be formed in this range. Under the strong confinement condition, the electron and hole can be treated independently and each can be described using the particle-in-a-sphere model. Thus, the optical properties of NCs in the strong confinement regime mainly attribute to the uncorrelated motion of an electron and a hole as well as the Coulomb interaction between them. The Hamiltonian for the strongly-confined electron and hole can be described based on the two-particle Hamiltonian form including kinetic energy terms and potential energy terms due to the confinement effect ($U(r)$), and Coulomb interactions between them:

$$\hat{H} = -\frac{\hbar^2}{2m_e^*}\nabla_e^2 - \frac{\hbar^2}{2m_h^*}\nabla_h^2 - \frac{e^2}{\varepsilon|\mathbf{r}_e - \mathbf{r}_h|} + U(r). \tag{2.50}$$

Without consideration of the Coulomb interaction, the energy gap between the lowest energy levels of an electron and a hole can be described using Eq. 2.49 above, which shows that the size dependent contribution to the energy gap varies as $(1/a^2)$; therefore the energy gap increases as the size of the NC decreases. This is due to the kinetic energy of the electron and hole in the confined structure varying as $(1/a^2)$, which becomes fairly significant now, in smaller structures. Meanwhile, the Coulomb energy term that has $(1/r)$ dependence has relatively less significance compared with the kinetic energy term in the strong confinement condition. The effect

of the Coulomb interaction between the electron and hole strongly confined in the NC can be treated as a first order perturbation to the problem. Several variational approaches have been made to calculate the first absorption peak of the NC ($1S_e1S_h$ – the ground state for the electron-hole pair; this corresponds to the HOMO-LUMO transition in molecular orbital), which can be expressed as [40–42]:

$$E_{1S_e1S_h} = E_g + \frac{\pi^2\hbar^2}{2\mu^* a^2} - 1.786\frac{e^2}{\varepsilon a}. \tag{2.51}$$

More rigorous approaches can be made to calculate the ground level of the electron and hole in the NC, which can be expressed in terms of the exciton Rydberg energy:

$$E_{1S_e1S_h} = E_g + \pi^2\left(\frac{a_{B_{exc}}}{a}\right)^2 Ry^* - 1.786\left(\frac{a_{B_{exc}}}{a}\right)Ry^* - 0.248Ry^*. \tag{2.52}$$

Figs. 2.4-2.6 show examples of size-dependent properties of CdX and PbX (X=S, Se, Te) quantum dots from previous investigations by several groups [12, 43–46]. Fig. 2.4 shows a typical Transmission Electron Micrograph (TEM) image and illustrations of size-dependent absorption spectra of PbSe NCs, studied by Q. Dai *et al.* (Fig. 2.4(a)-(c)) and M. C. Beard *et al.* (Fig. 2.4(d)). Fig. 2.5 and 2.6 show absorption spectra and extinction coefficient dependence on the size of cadmium chalcogenide NCs. The absorption spectra of quantum dots exhibit a series of discrete electronic transitions between quantized levels due to the quantum confinement effect. Thanks to the large exciton Bohr radius of PbSe (46 nm), strong confinement can be easily achieved in relatively larger size NCs (Fig. 2.4), as one can tell from the distinctive peaks observed in the absorption spectra, showing discretized energy states of the NC. On the contrary, the absorption spectra of CdSe NC which has the exciton Bohr radius of 6 nm, show evidence for the transition from the discrete level to the bulk-like continuous level as the size of the NC increases (Fig. 2.5). In addition, the first absorption peak exhibits a blue shift as the NC size decreases, which is a manifesta-

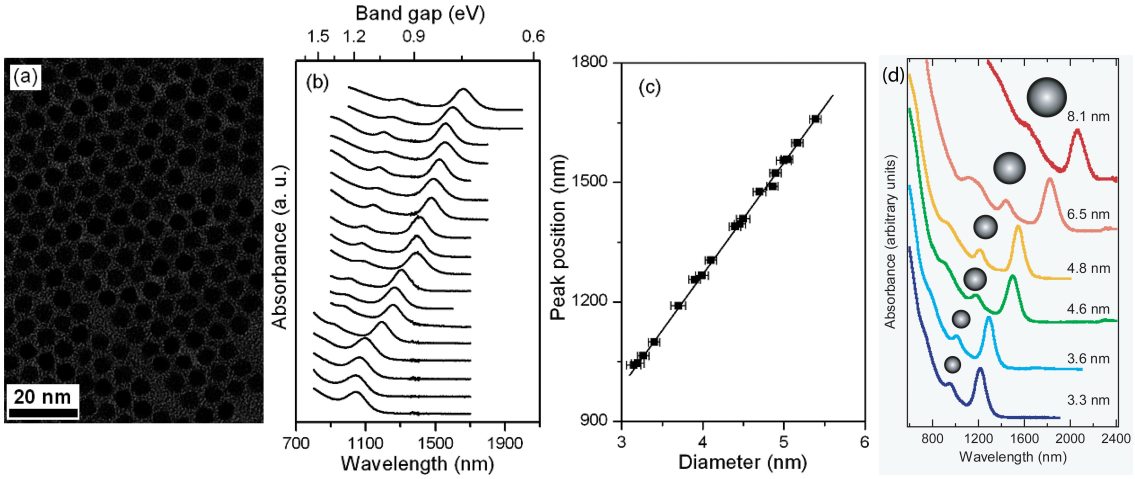

Figure 2.4: (a) A typical TEM image of PbSe NCs of 5 nm diameter in average, (b) absorption spectra of diversely sized PbSe NCs and (c) the first absorption peak position plotted versus the diameter of the PbSe NC [45]. (d) Absorption spectra with illustrations of PbSe NCs with average diameter ranging from 3.3 nm to 8.1 nm [12].

tion of the energy gap dependence on the NC size. The discrete optical spectra of NCs governed by the size (or the number of atoms inside) are often compared to the discrete optical spectra of an atom determined by the number of nuclei; the analogy from which NCs are often referred to as "artificial atoms."

To summarize, the size-dependent optical properties of the NC were illustrated based on the particle-in-a-sphere model approach by virtue of the aforementioned approximations, which enabled the calculation of allowed energy states of quantum-confined quasiparticles in the NC configuration in a simple manner. Smooth evolution of properties from the bulk crystal to the cluster-like features can be observed within the framework of the EMA. The limitation of the EMA based approach, however, rests on its asymptotical precision only associated with the large crystallites. Notably, energy bands are assumed to be parabolic only for small regions of the Brillouin zone near the band extrema. To make better agreements with the experimental result, further refinements of calculation have been attempted, for example, by applying a finite potential well to the problem [37, 38], energy-dependence in effective mass

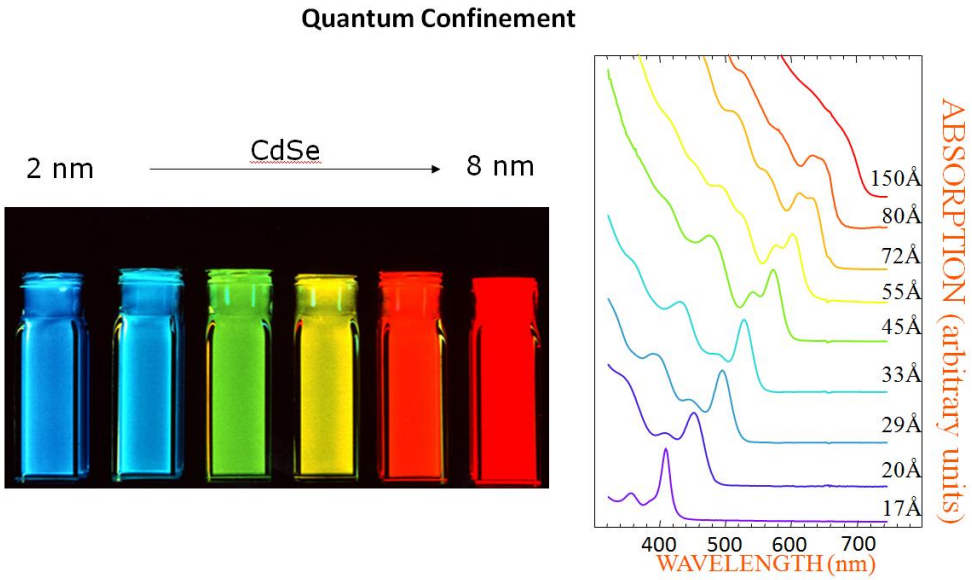

Figure 2.5: The fluorescence image and absorption spectra of CdSe NCs in various size. The average diameter ranges from 1.7 nm to 15 nm [46].

[47], empirical pseudo-potential method [48]. Sophisticated approaches other than particle-in-a-box model can be also made to calculate the energy band structure of the NC: $k \cdot p$ method, Luttinger Hamiltonian, and the Kane Model [33].

2.1.3 Carrier Multiplication (CM)

Carrier Multiplication (CM), often referred to as multiple exciton generation (MEG), is a photogeneration mechanism of multi-excitons, in which two or more electron-hole (e-h) pairs are produced by a single photon. Motivations for CM studies were provided by potential applications in photovoltaics where this effect can potentially improve the power conversion efficiency of solar cells via increased photocurrent [9, 14, 15]. Conventional photovoltaic solar cells can generate electricity by absorbing light or photons yielding a single electron-hole pair as schematically shown in Fig. 2.7(a). The energy in excess of the bandgap of the semiconductor is lost as heat. The detailed-balance power conversion efficiency of a Si-based single-junction solar cell can reach approximately 33%, which is known as Shockley-Queisser limit

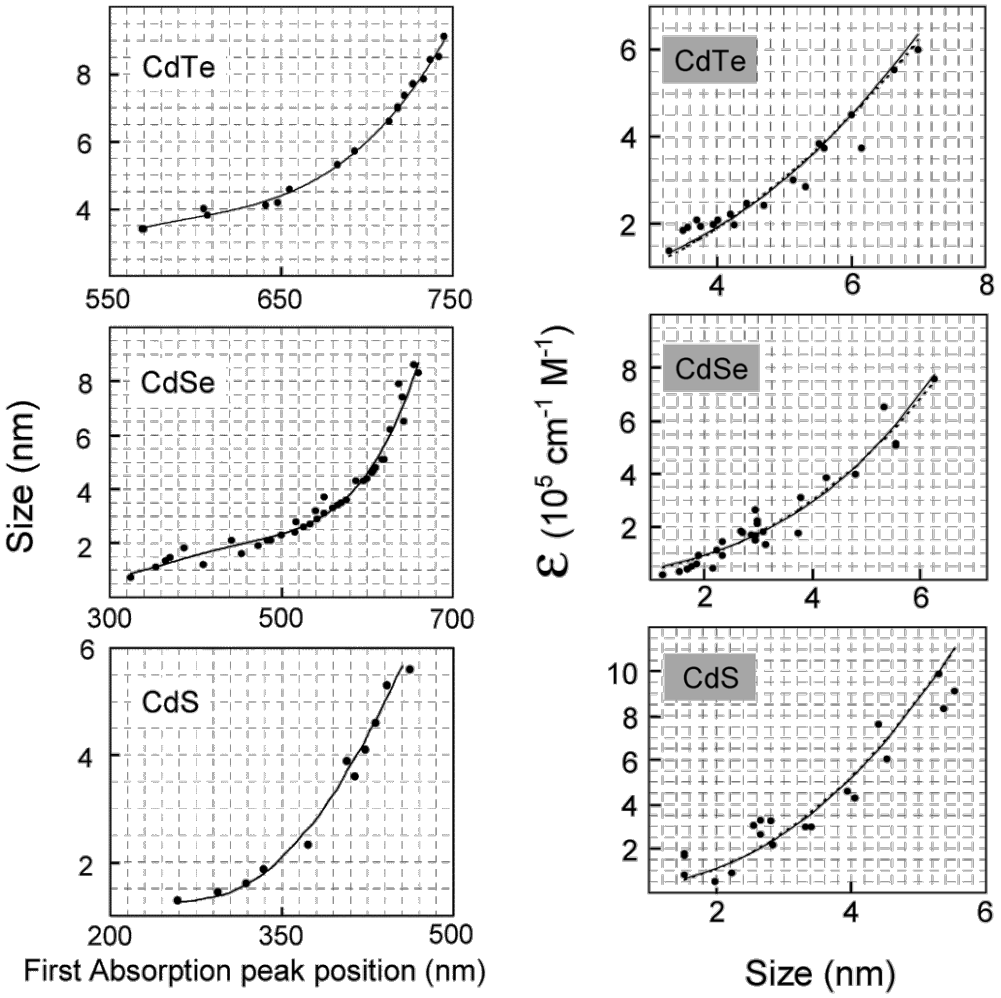

Figure 2.6: Size-dependent first excitonic absorption peak and the corresponding extinction coefficients of CdTe, CdSe, and CdS NCs. Fitting curves show the empirical formulae suggested from the work done by W. Yu *et al.* [43].

[49]. Greater-than-unity exciton multiplicities produced by CM in NCs can be exploited to increase the efficiency of photovoltaic cells and one can possibly surpass this limit. As shown in Fig. 2.7(c), for example, assuming the case of a $2E_g$ threshold for CM onset and an e-h pair creation energy of E_g (both values represent the energy-conservation defined limits), the power conversion efficiency can increase up to 42% [9].

In a typical semiconductor material, absorption of a photon with energy $h\nu \geq E_g$ would create a single e-h pair, and excited charge carriers with a kinetic energy of at least kT above the conduction and valence bands go through several types of relaxation interactions; for instance, carrier-carrier collisions, inter-valley scattering, and carrier-phonon interactions as they de-excite to the band edge. In the phonon emission process, the photon energy in excess of the energy band gap will be dissipated as heat until excited charge carriers reach equilibrium by transferring excess kinetic energy to quantized lattice vibrations, called longitudinal optical (LO) phonons (Fig. 2.8(a)).

Meanwhile, strong Coulomb interaction between carriers can open a competing carrier generation/relaxation channel, in which the excess energy of the hot carriers is transferred to another carrier in the valence band, thereby exciting it across the energy gap in a collision-like process, called *impact ionization (II)* (Fig. 2.8(b)). This is the reverse process of *Auger recombination (AR)*, a process in which the e-h recombination energy is not emitted as a photon, but is transferred instead to a third particle that is re-excited to a higher-energy state.

In the bulk state, both processes are inefficient because of relatively weak Coulomb interactions, the constraints imposed by translational momentum conservation and fast phonon emission competing with impact ionization. Thus, high thermal energy is required to create momentum-conserving phonons in order to enable the process [12, 50].

In 0-dimensional NCs, quantum dots (QD), where strong spatial confinement of

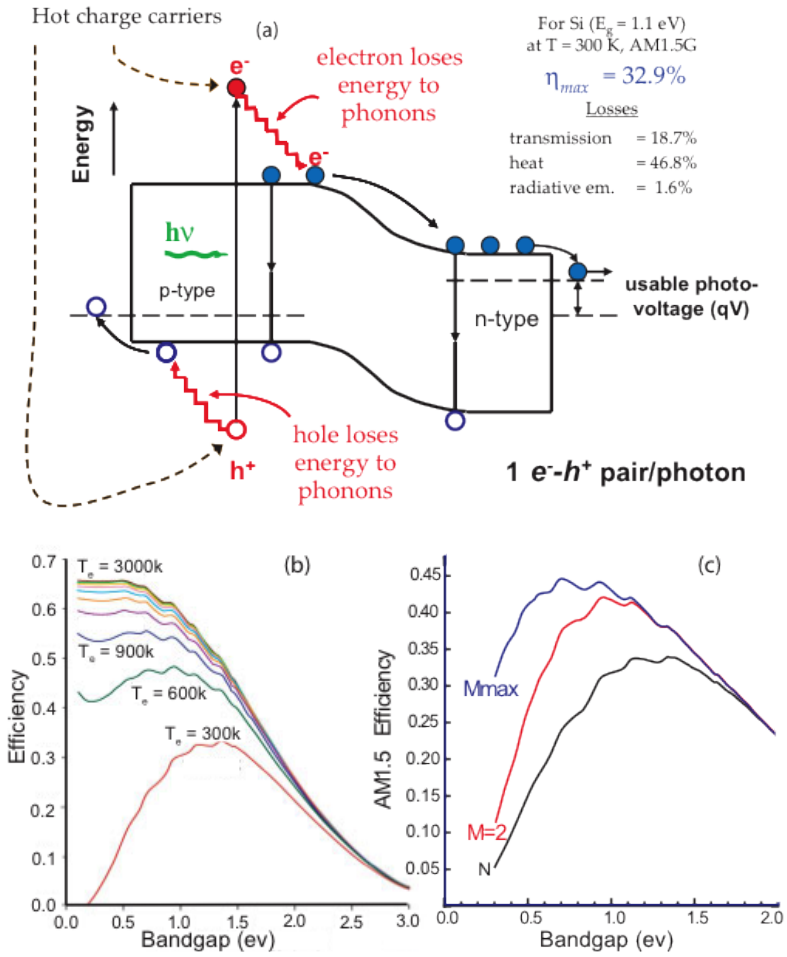

Figure 2.7: (a) Schematic of energy conversion process in a traditional p-n junction solar cell. Charge carriers (e^-, h^+) with excess kinetic energy are created from absorbing a photon that has higher energy than the band gap. These "hot" carriers lose energy by scattering with the lattice and emitting phonons. (b) If the carriers could be extracted with no heat loss, then thermodynamically allowed conversion efficiency could be doubled to ~67%. T_e is the hot carrier temperature. (c) Enhancement of power conversion efficiency expected from an increased photocurrent due to the carrier multiplication. N is the Shockley-Queisser limit, M = 2 is for extracting 2 carriers per absorbed photon at $E_{hv} > 2E_g$, and M_{max} is extracting M carriers at $E_{hv} > ME_g$ [12, 15].

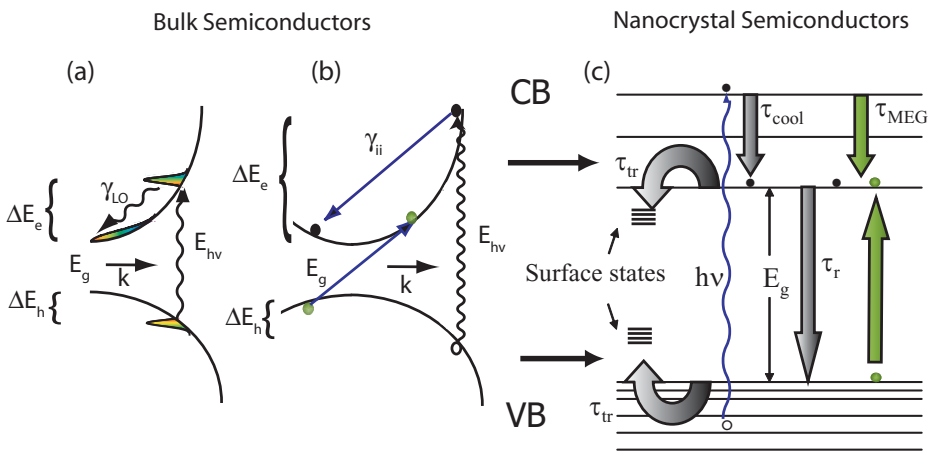

Figure 2.8: (a) Photo-excited carrier dynamics in bulk semiconductors. Following excitation by absorbing a photon with total energy in excess of the band gap, an athermal electron and hole population is formed with excess kinetic energy. The electrons/holes thermalize and cool to form a Fermi-Dirac distribution at the band gap edge within the timescale of 100 fs. (b) Electrons/holes with excess energy of greater than E_g may undergo impact ionization (II) to form additional carriers at the band gap. The II event must satisfy both energy and momentum conservation. (c) Carrier dynamics in NC semiconductors under the quantum confinement effect. Photo-excited carriers with excess energy are created only at the allowed states of the NCs. The influence of surface states becomes significant in NCs due to the increased surface to volume ratio. Cooling by phonon emission becomes less efficient, whereas CM becomes more efficient. [12].

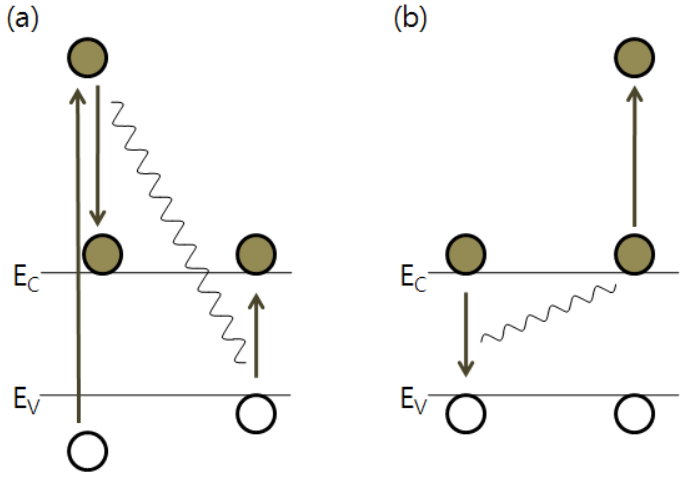

Figure 2.9: Schematic diagrams of: (a) the generation of multiple excitons via II and (b) AR in which the e-h recombination energy is transferred to excite another exciton to a higher energy state.

carriers in a small particle dimension is achieved and electronic wave functions are forced to overlap while dielectric screening effects are reduced, translational momentum conservation requirements are lifted[1] and stronger Coulomb interactions between carriers are promoted. In addition, the discretized electronic energy states of the carriers in the NCs reduces the availability of electronic states that satisfy energy conservation in the phonon emission process (Fig. 2.8(c)), which gives rise to remarkably slow intraband relaxation processes, a phenomenon known as the "phonon bottleneck" effect. For strongly confined carriers in NCs, especially, in which energy level separation can exceed several LO phonon energies, phonon-emission-type carrier relaxation can occur only through multiphonon processes, which rarely occur [50, 51]. Due to the suppressed rate of intraband relaxation, the energy loss exchanges can become dominated by II, which is the previously mentioned Auger-type process by which multiple excitons are generated from a single incident quanta, as shown schematically in Fig. 2.9(a) [10].

Another important consequence of the quantum confinement effect in NC solids is the enhancement of Coulomb interactions, as represented by the exciton and biexciton (a quasiparticle created from two free excitons) binding energies, the latter providing a measure of the strength of the exciton-exciton interaction. Increases in these energies as the NC size decreases eventually leads to the high efficiency nonradiative decay of multiexcitons via AR, counteracting II (cf. Fig. 2.9(b)). Symmetry of the matrix elements implies that both II and AR can be very efficient in quantum-confined NCs [10]. Fig. 2.10 shows schematic illustrations of: (a) CM via II and (b) other possible processes that can happen in NCs and the respective rates of each process. Multiexcitons generated through the CM process decay rapidly by AR and produce single excitons. To achieve enhanced photocurrent, the rate of e-h pair mul-

[1]Consider Heisenberg's uncertainty principle; when the position uncertainty of carriers are reduced due to the quantum confinement, the uncertainty in momentum increases – the momentum can no longer be a good quantum number to describe the quantum state of particle.

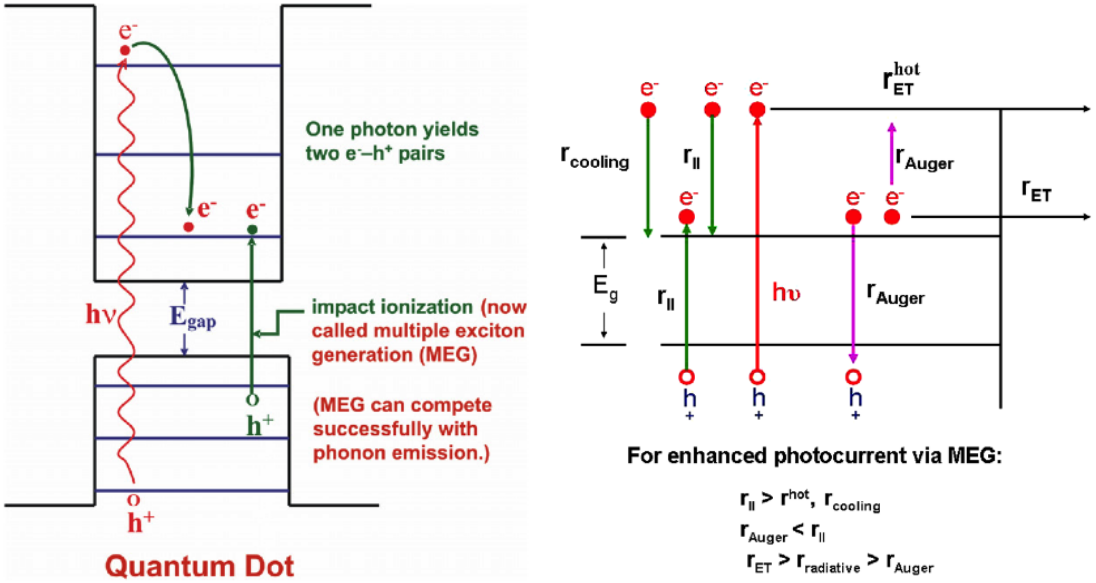

Figure 2.10: Schematics of (a) CM via II and (b) dynamical channels for photoinduced hot electron-hole pair in NCs. Rate conditions for each dynamical channel must meet shown criteria, in order to achieve enhanced photocurrent via MEG.

tiplication (impact ionization, $\mathbf{r}_{II}$) must be greater than the rates of carrier cooling ($\mathbf{r}_{cooling}$), electron transfer ($\mathbf{r}_{ET}$) of hot electrons, and the Auger recombination processes ($\mathbf{r}_{Auger}$). Also, the rate of electron transfer of cooled electrons must be faster than the radiative recombination rate ($\mathbf{r}_{radiative}$) and $\mathbf{r}_{Auger}$. Therefore, the quick separation and extraction of charge carriers generated by II, along with the development of effective suppression methods for counter-acting mechanisms, are essential in the efficient conversion of photon energy into electric charges [12, 32, 50].

Most methods used to study the CM phenomena exploit a significant difference in the recombination dynamics of single excitons and mutiexcitons. There exists a difference between the decay-time of single- vs. multi-excitons in NCs. This difference in decay time (nanoseconds for single excitons via slow radiative recombination vs. picoseconds for multiple excitons) is due to the Auger recombination (AR) in multi-excitons into a single exciton and can be detected in the NC population dynamics as a

fast decay component [12, 14, 52]. Two complementary techniques have been typically conducted to detect and quantify the decay time: the transient absorption (TA) measurement and the time-resolved (or up-conversion) photoluminescence (uPL).

Experimental evidences for the efficient CM in quantum-confined NCs have been reported from many spectroscopic studies through the two methods. Highly efficient CM in PbSe NCs was first reported in 2004 [31], and supported by follow-up studies of a slew of different NCs compositions including PbS, PbTe, CdSe, InAs and Si [53–56]. However, eventually this process has become a subject of intense controversy because, in other recent studies, the observed quantum efficiencies (QEs) of photon-to-exciton conversion (a.k.a. CM yields) have been significantly lower than those from earlier publications [57, 58] or the CM effect has not been detected at all [52, 59, 60]. These observed controversial results are attributed to several factors in the experiment: 1) NC surface properties, 2) NC charging, 3) multiple photon absorption events and 4) transient spectral shift.

Whereas most of observations of the CM process have been indirect and based on spectroscopic measurement, a recent study has reported more direct method to count the number of electron-hole pairs created per absorbed photon. J. B. Sambur *et al.* and O. E. Semonin *et al.* have reported the photocurrent quantum efficiency exceeding 100% via CM in PbS and PbSe NC based solar cells [11, 13]. However, due to the various types of carrier losses in devices – such as reflection, transmission, scattering, re-radiation and absorption in the non-QD part of the device, the result has not yet proven the ideal scenario of CM creating multiple carriers from absorption of a single photon of higher energy that is only limited by energy conservation.

Nevertheless, recent results have shown the existence of more efficient CM in NCs compared with bulk semiconductors. At least, in principle, the CM is expected to be more efficient in QDs due to the limited availability of electronic states which restricts the phonon emission process. Slow phonon-related carrier cooling in NCs has been

correlated with increased CM efficiencies [14, 33, 61]. This gives an important motivation for the application of NC based devices to the radiation detector development (2.2).

2.2 Motivation for the Radiation Detector Application

Semiconductor nanocrystals (NCs), as has been discussed, exhibit novel properties that can be exploited for various application – such as tunable energy band gap, and charge carrier multiplication – which arise due to the strong quantum confinement effect. In addition, the ability to control the composition, size and shape of NCs in their growth with the precision corresponding to the addition of an atomic layer provides a driving force for optoelectronics applications through the wave function engineering with the direct manipulation of the electronic wave functions [33]. Accordingly, NCs have been extensively studied for a number of applications such as solar cells [9–15], LEDs [19–21], photodetectors [17, 22, 23], telecommunication [62], and biomedical labeling [63, 64].

In this dissertation, we have investigated the viability of NCs for the material basis for the ionizing radiation detection and will present the potential behind utilizing NCs for radiation detection. Namely, we consider the motivation for developing NC based nuclear radiation detector as follows:

1) Average ionization energy (W-value) and charge carrier statistics.

2) High atomic number and density material with tunable energy band gap.

3) Low-cost fabrication with versatility in the size and shape.

2.2.1 Average Ionization Energy (W-value)

One of the main motivations that drives the development of NC based radiation detectors, whether nanoscintillators or nanosemiconductors, is that the phonon-assisted loss-processes can be suppressed to a larger degree than is possible in single-crystal materials, such that more of the incident information is converted into the information carriers (charge, light) that participate in signal formation. If one wishes to gauge the precision with which a semiconductor estimates the energy deposited during its interaction with an incident quantum, Fig. 2.11 shows that the energy consumed during the creation of an electron-hole pair, W, is equal to approximately 3 times the band-gap, E_g, the extra energy lost during phonon exchange as the excited carrier de-excites to the band-edge. For instance, the W value in silicon is 3.66 eV [65, 66], compared with a band-gap (E_g) of 1.12 eV. In fact, the most common materials used to detect ionizing radiation – silicon, germanium, and cadmium- zinc-telluride (CZT) – all fall near the $W = 3E_g$ line, while the n-VIIB materials, where n = II, III, or IV (e.g., TlBr and HgI_2) follow the same slope but exhibit better charge-creation statistics, as shown in the green line of Fig. 2.11 [67].

One would prefer that W be reduced to one times the band-gap, as shown by the lowest line in Fig. 2.11; that is, to be limited only by energy conservation, resulting in more charge carriers, which can not only enhance the size of the signal but it can reduce the statistical counting noise because more of the incident energy is converted into information which participates in the signal formation. If the variance in the charge population can be reduced by making the charge-creation process more efficient, then the statistical counting noise can be quenched, a feat only possible with momentum detectors such as mechanical radiation devices [68]. For nuclear radiation detectors, the realization of a uniform multi-exciton response would allow one to tolerate relatively large band-gaps because the uncertainty in the energy determination would be more dependent on non-uniformities in the fabrication rather than on simple

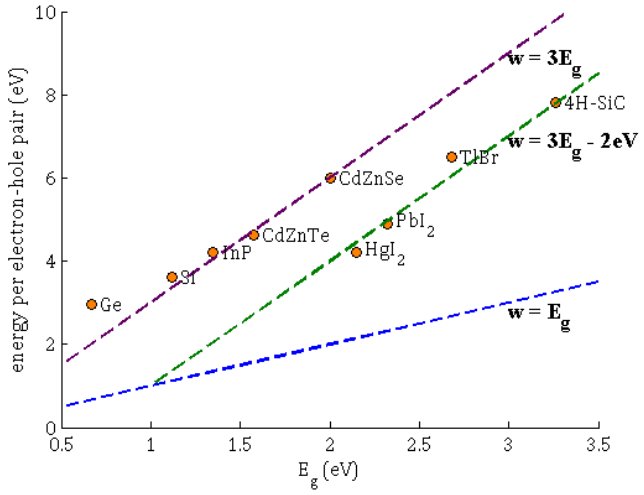

Figure 2.11: Relationship between the energy consumed per electron-hole pair created, W, and the band-gap E_g for a variety of semiconductor materials used in ionizing radiation detectors (in purple and green), in relation to the limit imposed by energy conservation (in blue). The data for the common materials is taken from [67] and the references therein, and the measurement of the NC data is described later in this report.

counting statistics.

These possibilities have been investigated for solar energy conversion, in which impact ionization (II) is used for carrier multiplication (CM) in semiconductor nanocrystals, with the goal of achieving quantum efficiencies limited only by energy conservation. Experimental results reveal that structuring semiconductors in a solid nanocrystalline composite can suppress the heat-loss mechanism relative to charge-creation processes, resulting in better estimates of the initial energy of the radiation than those produced by single-crystalline materials [33]. Even in the non-ideal case that the creation of charge carriers is not strictly limited by energy conservation, the discretized energy levels in NC will bring about more a efficient II effect, which will create more charge carriers in the NC than in the bulk material. This will still enhance the charge carrier statistics to accurately estimate the incident radiation energy. However, in principle, the uncertainty in the energy-measurement process can be reduced by limiting W-value to the size of the band-gap, which serves as the fixed

increment that governs the number of charge-carriers created.

The multiplicity of excitons is far greater if the energy source is from nuclear radiation in the form of a secondary electron or fast ion (from a gamma-ray or neutron interaction) rather than from an incident optical photon. This can impact the conversion efficiency because the effective band-gap will vary depending on the number of excitons. For example, in the quantum-confined PbSe system, the 1S state is 8-fold degenerate; therefore, if greater than 8 electron-hole pairs are created per dot, then the effective band-gap is formed between the 1P electron and hole states. For larger diameter NCs therefore (for which the E_g is also lower), then the varying band-gap can impact the energy conversion, though one can obviously design the NC ensemble to suppress this effect. Recently, an efficient CM in NCs for higher energy electron was also experimentally proven from the cathodoluminescence (CL) study of CdSe quantum dots [6].

2.2.2 High atomic number and density of material

The second motivation is related to the size-tunable optical properties of NCs. The evolution of the colloidal NC growth technique is approaching the precision of adding an atomic layer and allows unrestricted manipulation of the size-dependent property, thus one may engineer the energy band gap arrangement at will. Compound semiconductor materials that consist of high atomic number elements – lead chalcogenides, for instance – tend to have a small energy band gap, which requires bulky cooling mechanisms. Thus, their versatility, especially in deployability, is often hampered by not being favorable for room temperature operation. On the contrary, by utilizing the NC approach using the same semiconductor material, one can still take the advantage of the high atomic number elements in the material which assures more stopping power and detection efficiency without compromising their versatility limited due to their small band gap.

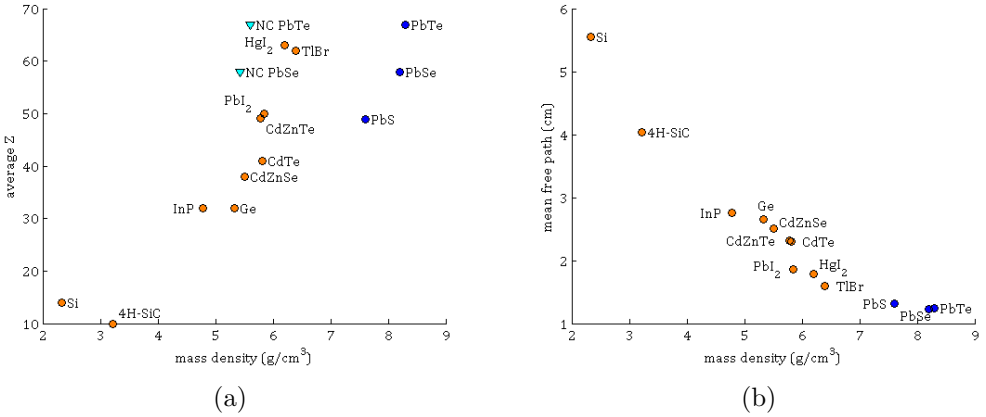

(a) (b)

Figure 2.12: (a) The average atomic number Z and the mass density for various semiconducting materials. (b) The mean free path for a 662 keV photon interacting with single-crystal forms of the semiconducting media.

Fig. 2.12(a) shows the comparison of various common single-crystal detection media with a few compound semiconductor materials under study, including lead and cadmium chalcogenides in both single-crystal and nanocrystalline form. Lead chalcogenides, especially, are superior in terms of their combined mass densities and atomic numbers, Z, both of which combine to yield a higher specific detection efficiency. As an example, Fig. 2.12(b) shows the photonic mean free path, as derived from the density and the macroscopic photoelectric-absorption linear attenuation coefficient at a photon energy of 662 keV, which is consistent with the gamma-ray emission from Cs-137. A comparison of PbSe or PbTe with CZT – the most common room-temperature gamma-ray detection medium – shows that the mean free path in CZT is 1.85 times longer than that of either lead salt. On a path-length normalized basis therefore, the lead chalcogenides can form a highly efficient gamma-ray detection medium.

The accrued efficiency advantages of utilizing high Z material in gamma ray detection can be distinguished more distinctively through the MCNP simulation [69]. Whereas the absolute efficiency depends on the source-detector geometric conditions, as well as inherent detector properties, which is only considered in calculation of in-

trinsic efficiency, usual efficiency values tabulated for gamma-ray detectors are the intrinsic peak efficiencies, which is defined as follows [70]:

$$\begin{aligned}\epsilon_{int.peak} &= \epsilon_{int} \cdot \frac{\epsilon_{peak}}{\epsilon_{total}} \\ &= \frac{\text{Number of pulses recorded on the full energy photopeak}}{\text{Number of radiation quanta incident on the detector}}.\end{aligned} \tag{2.53}$$

The simulated intrinsic peak efficiencies of ideal HPGe and $Cd_{0.9}Zn_{0.1}Te$ (CZT) crystals are compared with one of the highest atomic number material we investigate with the NC approach, PbTe, in Fig. 2.13. The crystal geometry was assumed to be the same 2 cm thick cylinders, considering the fact that the typical producible size of the crystal in CZT detectors currently, is no bigger than $2\times2\times2$ cm^3.[2] The figure shows that a PbTe detector exhibit several times better efficiency than HPGe detectors for 1 MeV photons and an order of magnitude difference for high energy γ-ray (> 2 MeV) for the same geometric conditions.

2.2.3 Low-cost fabrication modality with versatility in the size and shape

The other motivation for employing colloidal NC approaches is thus that high energy-resolution performance can be achieved with a lower-cost, larger-area alternative to detectors based on single-crystal materials. This could be, in an engineering perspective, the most practically appealing motivation amongst all. Although one can deploy high-vacuum, precisely controlled chamber-based equipment (e.g., molecular beam epitaxy) to create and grow nanoparticles, the most common approach is one of wet-chemistry, in which atmospheric pressure or low-vacuum processes are used to create the colloidal dispersions. Furthermore, the resulting solutions can then be

[2]One of the variance reduction techniques of Monte Carlo simulation theory, the direction biasing method, was utilized to calculate the intrinsic peak efficiency of the given detector. Thus, it was not necessary to have the same cross-sectional geometry for each detector (e.g., typical HPGe detectors are normally cylindrical whereas typical PbTe and CZT crystals are polyhedral) as long as the thickness of the detector normal to the source direction is the same; however, the simulation was performed assuming identical cylindrical detector geometries.

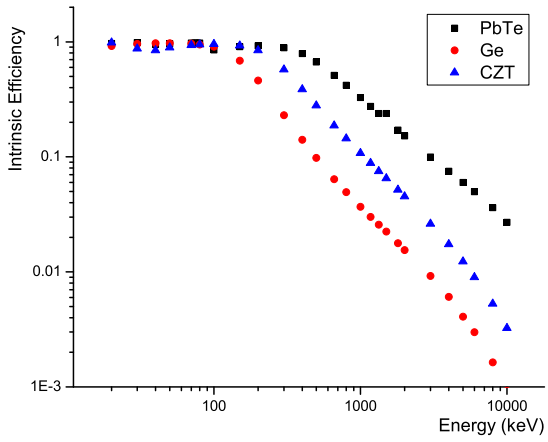

Figure 2.13: Calculated intrinsic peak efficiency of an ideal 2 cm×2 cm cylindrical single crystal PbTe detector compared with CZT and HPGe detectors of identical detector geometry setup.

deposited into solids of various form by the utilization of self-assembly during the solvent drying phase. Thus, the initial capital cost is far less than that required in a fabrication methodology based on microelectronic processing equipment, such as single-crystal growth furnaces.

2.3 Design Parameters and Problems

2.3.1 Dimension – Thickness

Among many design parameters for ionizing radiation detector fabrication, the most major concern relies on the size dimension of the detector: in this study, it is the thickness of the NC assembly. *How thick should we aim for, in order to make an allowable working device?* This problem is, in fact, what makes the nuclear radiation detector distinguished from any other optoelectric devices, such as LEDs, solar cells, and photodetectors. These devices are, in principle, designed to be formed within the range of the expected mean free paths of charge carriers in the superlattice assembly. LEDs, for example, are operated by excitonic emission from the recombination of

the injected electrons and holes; therefore, they must be made within the mean free paths of charge carriers so that electron-hole pairs can combine efficiently as well as the mean free paths of emitted photons so that it will produce an external light. When QD based LEDs are developed, typically a few to a couple tens of layers of QDs are deposited to from a device. Thickness requirements for photovoltaic devices are primarily "thick enough" to absorb all the incident photons, while "thin enough" to minimize the lost of charge carriers in their drift path. Most solar cells and photodiodes are usually made in the range of a couple hundred nanometer thickness.

In a broader aspect, nuclear radiation detectors are cousins of photovoltaics, except that the incident quanta does not necessarily have to be a photon. What are the mean free paths of the typical radiation quanta we are expecting?

a) Alpha particles: SRIM calculation [71] shows that an estimated range of the 5.486 MeV alpha particle emitted from Am-241 source is $\sim$22 μm in the lead sulfide bulk crystal (Fig. 2.14), one of the materials that is investigated via NC approach in this dissertation.

b) Beta particles: PENELOPE simulations [72] shown in Fig. 2.15 illustrate the simulated particle tracks in the lead oxide slab[3]. Notably, about 70% of simulated track paths of 1 MeV beta particles, for instance, are confined within the range of 200 μm, as shown in Fig. 2.15(a). This implies that, for charged particle detection, even a sub-mm thin foil of crystalline layer can effectively stop the charged particle and absorb the energy transfer.

c) Gamma rays: mean free paths of 662 keV gammas in typical semiconductor material are illustrated in Fig. 2.12(b). Fig. 2.15(b) shows the simulated tracks of 662 keV primary photoelectrons created from the photoelectric interaction with the 662 keV gamma in a lead oxide slab. Particle tracks can be fairly confined

[3]This was the closest material compared with the the atomic number and density of lead sulfide, in the existing material library of PENELOPE.

within the thickness of 100 μm. It implies that a minimum requirement of 100 μm thick high atomic number element material can act as an intermediate energy gamma spectrometer. However, the thickness in the direction of incident radiation quanta should be comparable to the mean free paths shown in the Fig. 2.12(b), which is a few millimeter to centimeters, in order to efficiently work as a gamma ray detector.

d) X-rays: typical x-rays will require $\sim$ mm thickness to guarantee enough interaction rate. X-ray spectrometers, in particular, are required to enclose most of tracks of photoelectrons created by the x-ray interaction. Fig. 2.15(c) shows the simulated path tracks of 80 keV electron in a lead oxide slab. Fortunately, the estimated size of charge cloud tracks are $\sim$10 μm, which is small compared with the detector's mm size. However, this also means that the thickness has to be at least 10 μm in order to properly work as an x-ray spectrometer.

e) Neutrons: it depends on the nuclide and the energy-dependent cross-section of the neutron interaction. In case of thermal neutrons, for example, a thin layer (a few micrometer) of boron lining can act as a converting layer to absorb thermal neutrons and produce charged particles. The resulting charged particles can be detected using a thin film material as was discussed in the alpha particle detection. In case of fast neutrons, the mean free paths of neutrons can be millimeters or could be up to tens of centimeters in a material.

So, although one can readily make a thin charged particle detector; making a 5 mm thick homogeneous device presents the empirical challenge in developing NC based nuclear radiation detector.

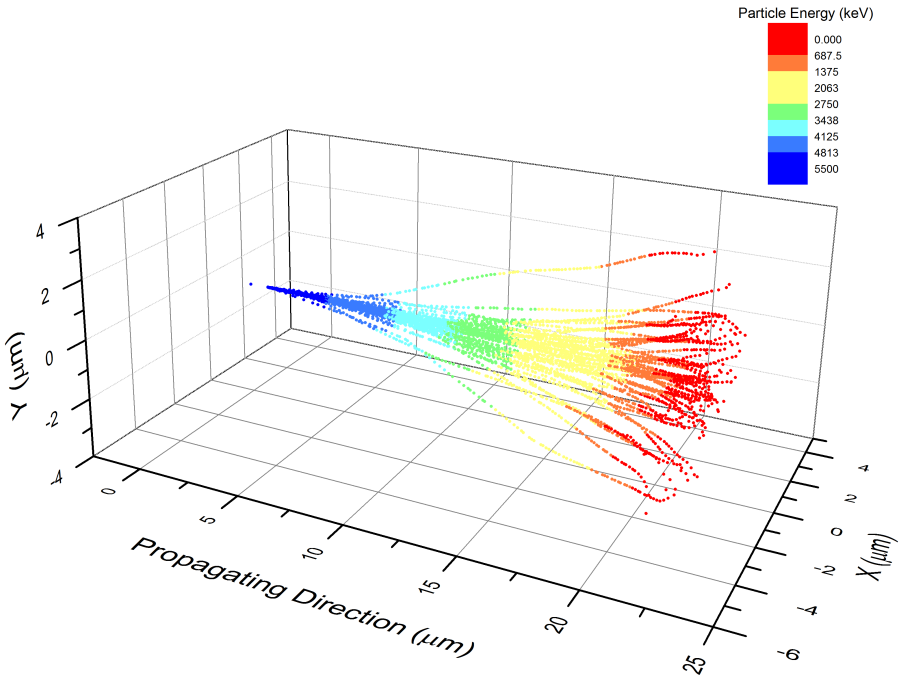

Figure 2.14: Simulated particle tracks of 5.486 MeV alpha particle incident in PbS using SRIM. Note that the range of the alpha particles is ∼22 μm in the PbS bulk crystal.

2.3.2 Confronting Challenges

If one can maximize the charge creation and minimize the loss during subsequent motion, then the capabilities of semiconductor-based radiation detectors can be substantially enhanced. For more advanced materials, such as the wide band-gap devices, material impurities and defects can reduce the number of information carriers and thus compromise the signal-to-noise ratio. Nanocrystalline semiconductors are promising candidates, in principle, to increase the charge creation yield and further, to suppress the uncertainty in conversion by further suppressing the Poissonian exciton population inherent to charge-creation in the bulk; nevertheless, that charge collection is typically quenched during charge passage because of trapping at the interfaces. As charge carriers transit through the various surfaces and materials in the composite during signal formation, their motion is often inhibited and the charges are trapped at the interband interface states due to induced stress and dangling bonds and finally

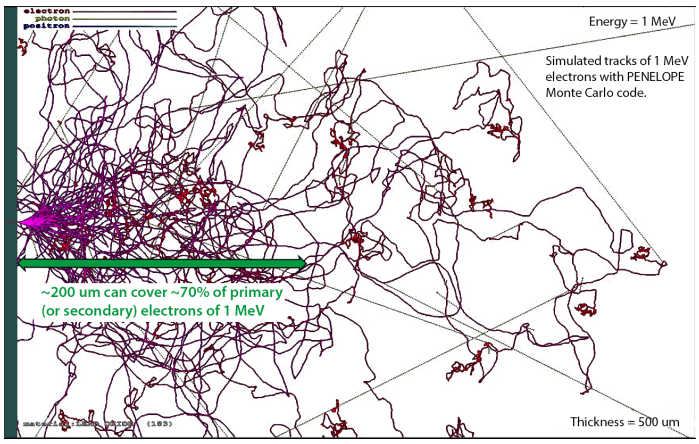

(a)

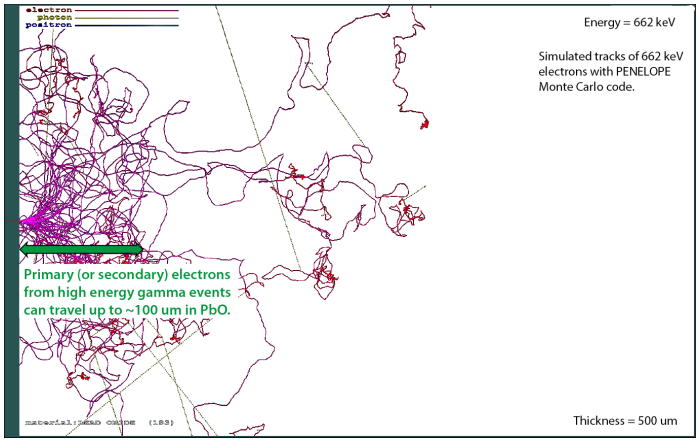

(b)

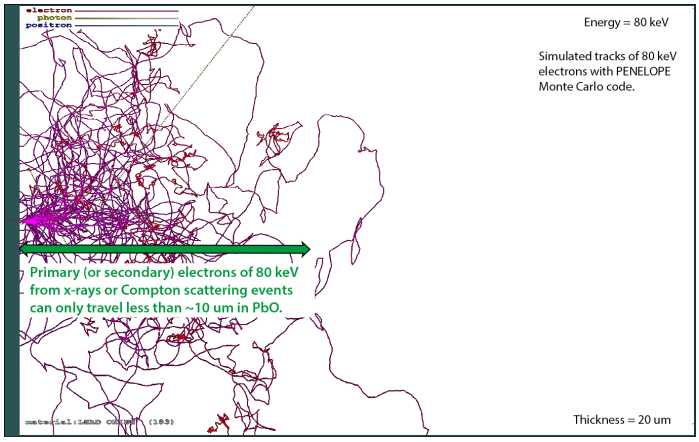

(c)

Figure 2.15: Simulated tracks of: (a) 1 MeV, (b) 662 keV and (c) 80 keV electrons in a PbO slab calculated by PENELOPE Monte Carlo code [72]. Primary and secondary electrons created by gamma-ray interactions can travel from a few micrometers up to a couple hundred micrometers depending on their energy.

form a space charge to limit the charge conduction again.

The poor charge transport characteristics of the devices made from the amorphous or colloidal material via solution process have been inevitable drawbacks of the fabrication method. Therefore, the main focus of the research is on controlling these charge loss mechanisms at NC-surfactant interfaces and between NCs so that the advantages accrued from NC charge-creation can be realized.

First, it is important to understand the physics of the charge carriers in the assembly – the charge transfer mechanism, both the creation and mitigation of surface states, and effective multiplicities by the high energy secondary electrons – so that one can take advantage of the favorable charge-creation properties of advanced materials. Secondly, one can attempt to maximize the electron exchange coupling for adjacent NCs such that the material makes a phase transition to the fully delocalized conducting regime. The empirical challenge here is, thus, to create a colloidal solid with highly ($< 5\%$ in size dispersion) uniform NCs deposited in close proximity such that the carriers become fully delocalized throughout the solid [73]. Furthermore, as previously mentioned, practical concerns in applications require fast extraction of the charges before Auger recombination (AR) can take place, although this has been demonstrated with high efficiency [13].

Another concern for nuclear radiation-detector applications is the energy loss from the high-energy secondary electrons in the surrounding material matrix used to passivate and coordinate the ensemble. These organic moieties bound to the surface are often composed of low atomic number material, thus may not be significant. However, for achieving high-performance devices, this issue must be considered even if the effect might be small. An approach utilizing the core-shell structured NCs is often suggested in device applications, to passivate the core with a higher band-gap capping layer of inorganic material, however, this is main reason the approach is often avoided; we want to avoid exciton creation in the bounding matrix.

Related to the consideration of thickness previously discussed, making a large, thick and homogeneous NC assembly through the solution based process is the big challenge in the successful realization of NC based nuclear radiation detector. As we will discuss, realizing novel properties in nuclear radiation application requires careful control over: a) the structure, size, and uniformity of the nanoparticles themselves, b) effective coupling of the nanoparticles into a colloidal solid through which the information can flow unimpeded, and c) suitable device design such that the information can be coupled into a readout circuit.

CHAPTER III

Experiments:

Synthesis, Characterization, and Fabrication

3.1 Synthesis of Nanocrystals

In order to take advantage of size-dependent properties of NC materials, it is essential to obtain NCs of consistent size and shape as well as identical chemical composition and surface structure. Traditionally there have been two main approaches developed to create NCs: top-down ("physical" methods) and bottom-up ("chemical" methods). The former starts with a macroscopic scale object and gradually reduces its size or dimension to the nanometer regime. Mechanical approaches such as high energy ball milling and melt mixing, as well as optical techniques such as laser ablation and laser pyrolysis belong to this category. The other approach is nucleating individual atoms and molecules into higher order structures through a sequence of chemical reactions with or without catalysts. Methods that utilize ion beam techniques such as molecular beam epitaxy (MBE), metal-organic chemical vapor deposition (MOCVD) [74–76], and vapor-liquid-solid (VLS) method [77, 78] to grow nanowires are considered as bottom-up approaches. In particular, colloidal chemical synthesis of NCs has become a popular method to create high-quality NCs with high crystallinity and size-monodispersity, good surface passivation, and the freedom of solubility control.

Colloidal NCs are often characterized as an inorganic core overcoated with a layer of organic ligand molecules, providing electronic and chemical passivation of the surface dangling bonds and thus preventing uncontrolled growth and agglomeration of the nanoparticles. The optical properties of NCs are mostly attributed to the properties of the core material, whereas their chemical reactions are mostly characterized by the organic moieties bound to the NC. That is, their chemical properties as molecules or clusters, such as solubility and reactivity depends on the identity of the surface ligand.

As previously mentioned, wet chemical synthesis of colloidal NCs has its advantages over other methods in that monodisperse NC particle size control is possible. In this synthetic method, the adjustment of the reaction conditions, including the time, the temperature and the concentration of precursor reagents and surfactants, are critical in the control of NC size [79, 80]. A typical synthetic method of creating colloidal NC dispersion is called the hot injection method, or the high-temperature solution-phase route [79], which is often described in term of a monodispersed colloid preparation method proposed by V. K. La Mer and R. H. Dinegar [81]. By rapidly injecting organometallic precursors into a solvent while maintaining the reaction temperature and vigorously stirring, the precursor concentration goes temporarily beyond the nucleation threshold and becomes supersaturated. A short burst of NC nucleation occurs after supersaturation, which suddenly reduces the precursor concentration level. The small crystallite seeds then experience the growth stage for which the dynamics are controlled by the interplay between the diffusion mechanism of precursor ions and surface tension of the growing crystallites. The size distribution of the NC dispersion is principally determined by the nucleation interval when the NCs begin to grow, with a short period producing better uniformity in the NC size. Therefore, both the rapid injection of the precursor and the vigorous stirring of solvent with strict temperature control are critical in this method [80].

A slightly different approach to produce monodisperse NCs involves the mixing of all the precursors in a reaction vessel at a low temperature and then moderately heating the solution to grow the particles. An accelerated chemical reaction induced by increasing the temperature of the solution gives rise to supersaturation, which is relieved by the nucleation burst. The subsequent control of the solution temperature will induce further growing of NCs [82].

Synthesis of colloidal NCs are often followed by the "clean-up" process of the nanoparticles. One cannot emphasize enough the importance of the clean-up process, especially, in the device application of the NCs. This process is not only used to purify NCs by removing most of the unreacted organic solvents and precursors, but it can be also used for various types of surface treatments, and it is most commonly used as a method for size-selective precipitation of NCs [80, 83, 84].

This is essentially a titration process utilizing polarity and mass density difference of the colloids. Since chemical properties of colloidal NCs are determined by the surfactant, nanoparticles capped by non-polar ligands, for instance, are miscible with non-polar solvents. That is why oleic acid (OA) capped NCs are often re-dispersed in such solvents as hexane, octane, toluene, or chloroform. Slow addition of the incompatible solvent (polar solvents in this case) can slowly change the polarity of the solution, such that the capping ligands around the nanoparticle can no longer support the weight of the NC because of a weaker surfactant interaction with the non-polar molecules in the solvent. Therefore, the nanoparticles start to precipitate and one can separate the precipitated particles from the supernatant by centrifuging the colloidal dispersion. The precipitatant can then be re-dispersed into a compatible solvent again, which can be centrifuged once again at a very high speed, to remove any residual reaction debris contained in the solvated NC dispersion. This process is often repeated several times; however, continued purification beyond what is necessary only decreases the chemical yield by wasting a certain portion of the NCs in every iteration.

Note that smaller particles, due to their higher surface-to-volume ratio, have a higher relative concentration of surfactants which can prevent the nanoparticles from being precipitated from the solution even in the polarity transition of the solvent. Thus, the size-selective process is simply titrating the colloidal dispersion to slightly beyond the threshold of precipitation to precipitate a small fraction of the NCs. Such controlled precipitation preferentially removes the largest NQDs from the starting solution, as these first become unstable to solvation [33]. In a similar manner, one can separate the smaller NCs mixed in the supernatant from the main dispersion by adding an "adequate" amount of the incompatible solvent. Essentially this is just the same as the clean-up process. One can still extract the smaller particles later from the supernatant: a) by adding more incompatible solvent, or b) with much faster centrifuging. The iteration of this titration-precipitation-redissolving procedure will provide a more fine-tuned size dispersion at the cost of lower chemical yield of the NC.

3.1.1 Synthesis of CdTe Nanostructures

Cadmium telluride (CdTe) is a II-VI semiconductor material that has been extensively investigated as a single-crystal semiconductor radiation detector. NCs of the cadimum chalcogenides are also widely studied for the solar cell applications and the detection of optical photons. In fact, the fabrication methods are geared toward thin films consistent with the stopping of non-ionizing poorly-penetrating radiation. Although less favorable than the lead chalcogenides for the intended application, the CdTe NCs can be easily characterized in the visible light wavelength range, and they can be utilized to study properties of the wide band gap NC assembly. We have therefore investigated both systems.

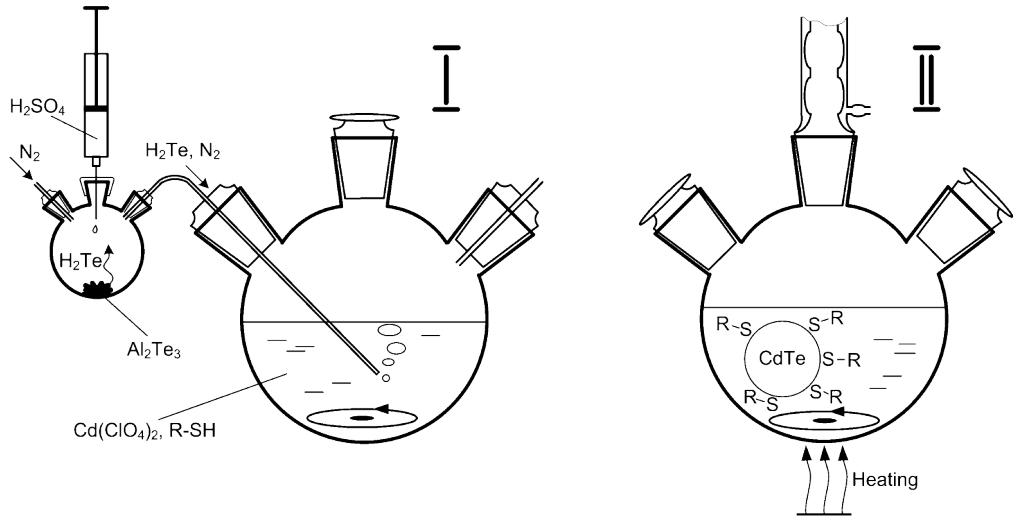

Figure 3.1: A schematic of TGA-stabilized colloidal CdTe NC synthesis. CdTe precursors are created by introducing H_2Te gas into the aqueous solution of Cd precursors complexed by thiols, followed by the formation and growth of CdTe NCs promoted by the reflux procedure [85].

3.1.1.1 CdTe Nanocrystal

The aqueous dispersion of the thioglycolic-acid (TGA)-stabilized CdTe was synthesized by the second approach discussed in the section introduction, as shown in Fig. 3.1 [82, 85]. At room temperature, 0.9113 g (ca. 2.17 mmol) of cadmium perchlorate hexahydrate, $Cd(ClO_4)_2 \cdot 6H_2O$ was dissolved into 120 ml of vigorously stirring de-ionized water, resulting in a solution pH of 2.7. TGA ($HSCH_2CO_2H$), of amount 0.4 ml (ca. 5.7 mmol), was added to the solution via a syringe, followed immediately and in conjunction with approximately 6 ml of 1 M NaOH in order to adjust the pH to 11.4, the latter addition necessary to obtain an adequate reaction yield.

Hydrogen telluride gas, H_2Te was generated by the acidification of 0.2 g of aluminum telluride, Al_2Te_3, with deoxygenated sulfuric acid (20 ml, 0.5 M) injected into the deoxygenated reaction solution, all in an inert environment, created by the flow of Ar or N_2 gas. The H_2Te gas flow was maintained for 10 minutes in order to ensure that sufficient Te was in the solution, after which refluxing began. The cadmium

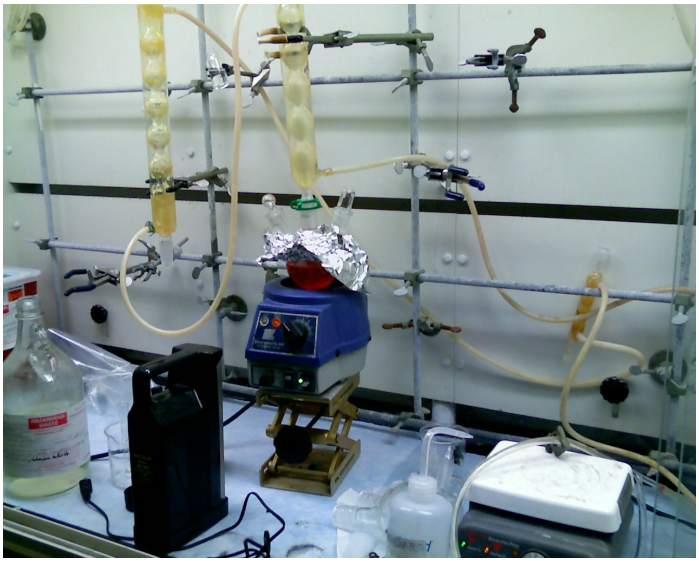

Figure 3.2: Photograph of a typical experimental setup for the colloidal CdTe NC synthesis with the resulting reaction solution.

thiolgycolic acid mixture, Cd^{2+}:$HOOCCH_2SH$, reacted with hydrogen telluride gas, with the thiol groups (RSH), acting as a reaction control, and the carboxylic acid enabling the formation of an aqueous dispersion.

During refluxing, in which the reaction flask/condenser column was sealed and the solution was maintained at the boiling point of water, the NC particles were grown to the desired size, which could be controlled via the reflux time. A standard setup with the resulting reaction solution is shown in Fig. 3.2. For instance, NCs in the nm range can be grown in 20 minutes, whereas larger particles can take 24 hours or more, the size judged during growth via the UV-photoluminescence [86]. For instance, a synthesized NC dispersion may exhibit green-colored photoluminescence of 540 nm average wavelength, which corresponds with a NC particle size of 3–4 nm [43]. According to the chemistry of the synthetic process, the resulting dispersion contains NCs with a CdTe crystalline core surrounded by deprotonated –OH and –COOH groups of the thioglycolic acid; thus, the NCs have negative charge [82, 87, 88].

3.1.2 Synthesis of CdTe Nanowire

As will be discussed later, lengthy fabrication time and effort to form a macroscopic layer were obstacles for the development of nuclear radiation detectors based on CdTe NC materials via the layer-by-layer (LBL) method, in spite of the excellent radiation response from the limited detection volume. Therefore, approaches utilizing CdTe nanowires (NW) were attempted to form a macroscopic assembly via the vacuum filtration method, which is also popularly used in various other application such as growing graphene oxides on substrate [89, 90]. First, CdTe NC particles were synthesized by following known procedures [7, 82, 85, 87], after which nanowires were grown from the 1-D assembling nature of the CdTe nanoparticles. Therefore, CdTe nanoparticles stabilized by thioglycolic acid (TGA) were prepared with a similar procedure described above.

Briefly, ∼2.3 mmol of $Cd(ClO_4)_2{\cdot}6H_2O$ (Alfa Aesar) dissolved in 125 ml of water was mixed with ∼5.7 mmol of thioglycolic acid (TGA). Subsequently, the pH of the medium was adjusted to be ∼9 by addition of 1 M NaOH solution. The reaction mixture was placed in 250 ml-three neck round bottom flask with a septum, valve and condenser and was bubbled with N_2 gas for 30 min. H_2Te gas formed by the reaction of Al_2Te_3 with 0.5 M-H_2SO_4 was passed through the reaction mixture for 10 min. Then, temperature was raised to 100°C and the reaction proceeded for 1 hr under magnetic stirring. The obtained nanoparticles have green photoluminescence ($\lambda_{em} \approx 548 \pm 20$ nm) when excited at 375 nm-light. This wavelength corresponds to a mean particle diameter of 3.22 ± 0.20 nm and a mean band-gap of 2.26 ± 0.08 eV, according to the empirical relations reported by W. Yu et al. [43], compared with a bulk band-gap of 1.44 eV [91–93].

For the assembly into 1-D nanowires (NWs), CdTe nanoparticles were precipitated by adding methanol and were centrifuged at 6000 rpm for 20 min. This process resulted in the partial removal of the stabilizer. The precipitated nanoparticles were

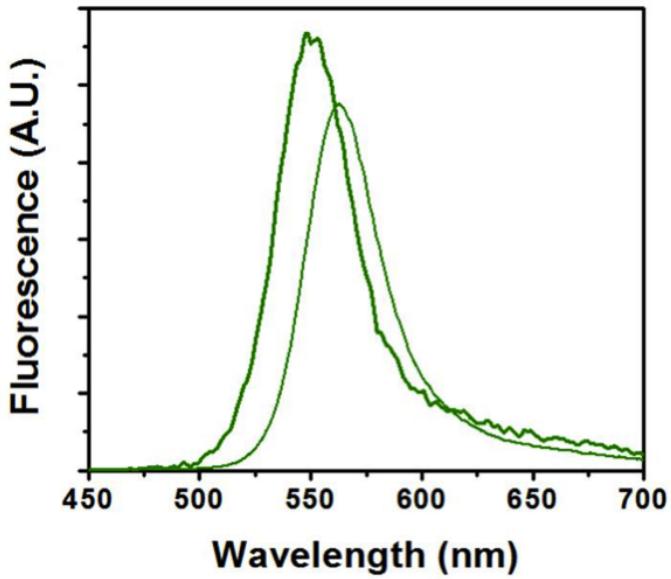

Figure 3.3: The PL emission spectra of parent CdTe nanoparticles (bold line) and resulting nanowires (faint line).

re-dispersed in pure water at pH 9.0. In order to assemble them into the NWs, the dispersion was allowed to age in darkness at 70°C for several days, during which the color of the solution gradually becomes darker [94]. The formation of NWs induced the wavelength red-shift for the maximum photoluminescence ($\lambda_{em} \approx 565 \pm 20$ nm). CdTe NCs in zinc blend structure makes a phase transition to hexagonal wurzite structures, which is intrinsically anisotropic and has a unique (001) axis. In and the assembly of NWs is driven by strong long-range dipole-dipole interactions of anistropic-shaped nanoparticles [94]. Fig. 3.4 and Fig. 3.5 show the transmission electron micrograph (TEM) images of CdTe NCs and NWs, respectively, and Fig. 3.3 shows the photoluminescence spectra of the CdTe NCs and NWs.

3.1.3 Synthesis of Lead Chalcogenide Nanocrystal

Lead chalcogenide materials (PbX, X = S, Se, Te), or lead salts in particular, have favorable physical properties for their use in NC applications, advantages which are fortuitous if one extends their applicability beyond optical radiation to highly

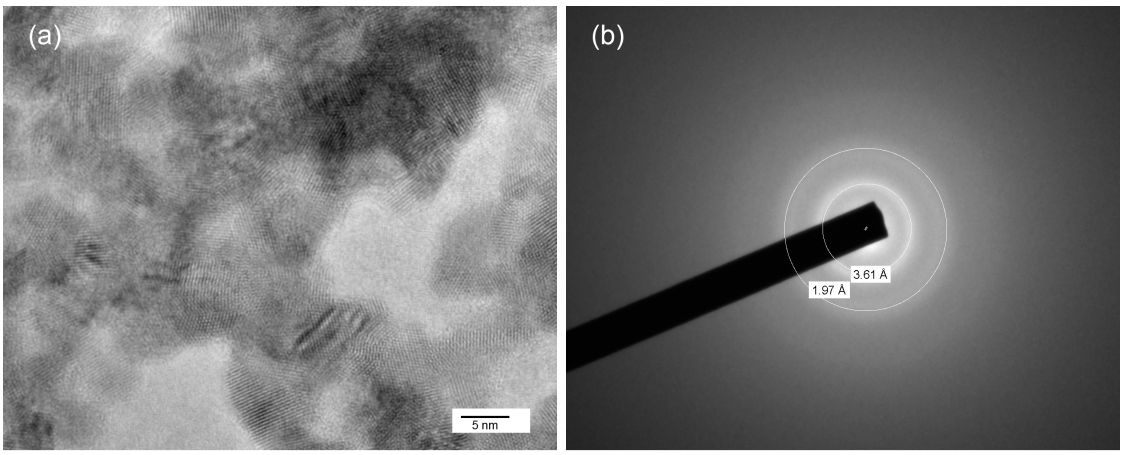

(a) (b)

Figure 3.4: TEM image and diffraction pattern of the TGA-stabilizaed CdTe NCs.

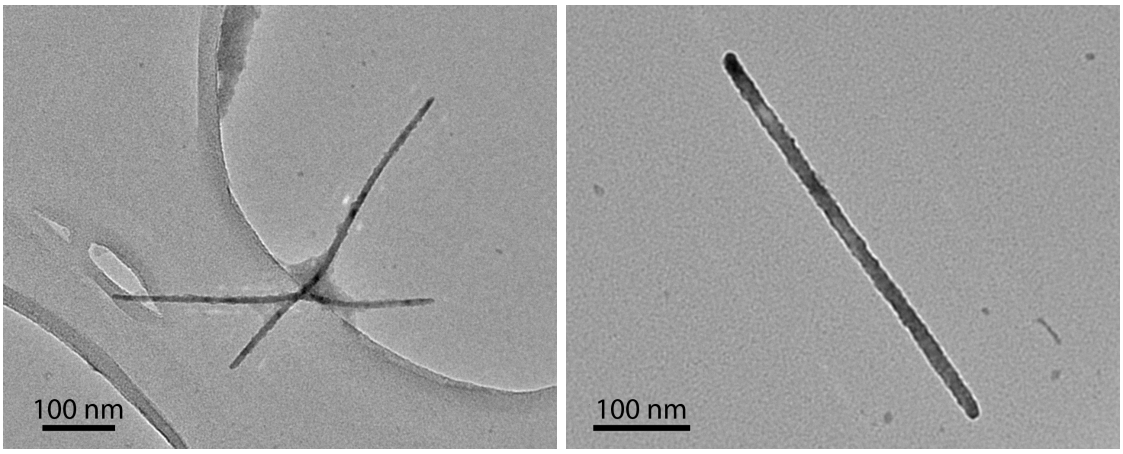

(a) (b)

Figure 3.5: TEM images of CdTe NWs assembled from the CdTe NCs.

penetrating ionizing radiation because they possess inherently high stopping-powers as previously mentioned (2.2.2). Their high atomic numbers (Z_{eff} = 49, 58, and 67 for PbS, PbSe, and PbTe, respectively) and high density (ρ = 7.6 g/cm^3, 8.2 g/cm^3, and 8.3 g/cm^3 for PbS, PbSe, and PbTe, respectively) inherently ensure better detection efficiency of the incident quanta, compared with other materials of the same physical dimension. Specifically, the large bulk Bohr radii of their excitons (20 nm, 46 nm and 50 nm for PbS, PbSe and PbTe, respectively) enables strong quantum confinement in relatively large NC structures. In addition, the materials have nearly identical and small effective masses of the electrons and holes resulting in the symmetric, relatively simple and broadly separated electronic energy density levels, which lead to much slower intraband relaxation [33, 51].

3.1.3.1 Synthesis of PbSe Nanocrystal

Colloidal PbSe NCs were synthesized through the high-temperature solution-phase routes, following the procedure reported by C. B. Murray *et al.* illustrated in Fig. 3.6 [7, 79]. Lead oleate and selenium dissolved in trioctylphosphine (TOP-Se) were used as organo-metallic precursors, and diphenyl ether (DPE) as the high-temperature organic solvent. The lead oleate precursor was prepared by dissolving 0.65 g of lead(II) acetate tryhydrate, $Pb(CH_3COO)_2{\cdot}3H_2O$, into a mixture of 2 ml of DPE, 8 ml of TOP and 1.5 ml of oleic acid, which was heated to 85°C for 1 hour under vacuum and subsequently cooled to room temperature. In this solution, the oleic acid is used as the stabilizing agent. Meanwhile, 0.395 g of Se powder was dissolved in 5 ml of TOP. 1.7 ml of TOP-Se was then mixed with lead oleate. Precursors were rapidly injected into vigorously stirred DPE at various reaction conditions, defined by the injection temperature (T_{inj}), in an inert environment. PbSe NCs were grown at the growth temperature (T_{gr}) for 3–6 minutes and cooled.

Synthesis of the PbSe NCs was also studied by varying the concentration of pre-

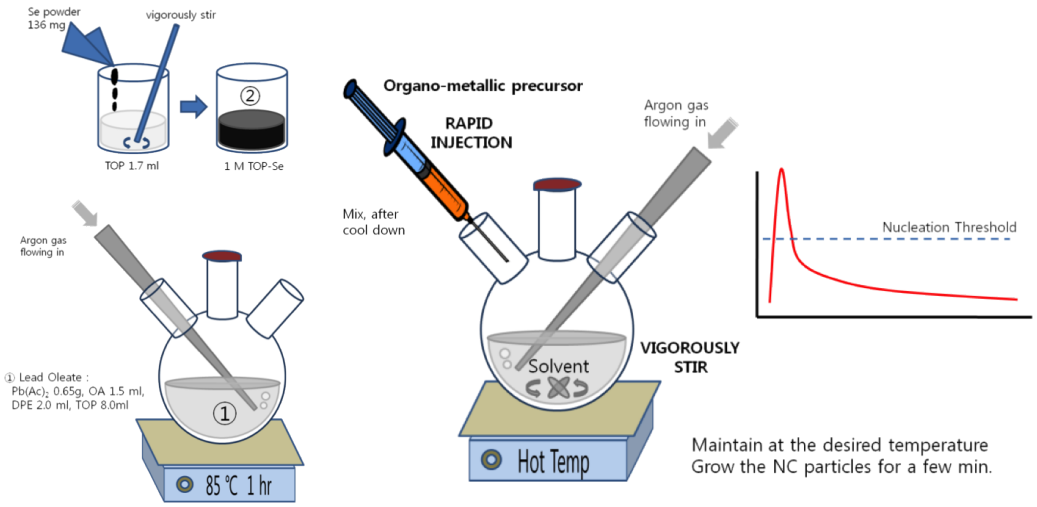

Figure 3.6: Synthesis of colloidal PbSe nanocrystal (NC) dispersion through hot injection method.

Precursors	T_{inj}	T_{gr}	Time	Size	Shape	Figure
Lead-oleate[1]	150°C	123°C	6 min.	7–9 nm	Nearly-spherical	Fig. 3.7(a)
Lead-oleate[2]	150°C	123°C	3 min.	12–14 nm	Star-shaped	Fig. 3.7(b)
Lead-oleate[2]	180°C	142°C	3 min.	∼20 nm	Star-shaped	Fig. 3.7(c)
Lead-oleate[2]	210°C	165°C	3 min.	∼30 nm	Star-shaped	Fig. 3.7(d)
Lead-oleate[1]	180°C	115°C	6 min.	∼10 nm	Nearly-spherical	Fig. 3.7(e)
Lead-oleate[1]	150°C	115°C	5 min.	3–5 nm	Nearly-spherical	Fig. 3.7(f)

[1] $Pb(Ac)_2$ 0.65 g, DPE 2.0 ml, TOP 8.0 ml, and OA 1.5 ml were mixed with 1.7 ml of TOP-Se

[2] $Pb(Ac)_2$ 1.5 g, DPE 25 ml, and OA 5.1 ml were mixed with 12 ml of TOP-Se

Table 3.1: Synthesis of PbSe NC at various reaction conditions – injection temperature (T_{inj}), growth temperature (T_{gr}), and growing time were varied.

cursor reagents and surfactants which provides control over the particle growth. It was reported that one can alter the reactivity of the precursor diffused on to the specific crystal plane, which concomitantly alters the growth speed, by alternating the relative concentration of acetate (Ac) from the $Pb(Ac)_2$ precursor reagents [95]. In addition, the role of OA in the synthesis of NC particle was studied in a previous study [96], showing the slow kinetics of a less discrete, more prolonged nucleation event induced by the OA. The size and shape of the NC particles made in various reaction conditions are listed in Table 3.1. The size and shape of the NC particles in each sample exhibited roughly uniform features over the sample. Notably, higher reaction temperatures result in the formation of the larger NC particles as shown in Fig. 3.7. Fig. 3.7(a)-(f) show different sizes and shapes of the PbSe particles synthesized in various reaction conditions. The growth of NC particle was controlled by the relative concentration of the precursor reagents and surfactants mixture ratio, which affects the relative concentration of the acetate in the lead-oleate precursor.

The clean-up process always followed the synthesis procedure. As illustrated in Fig. 3.8, the colloidal dispersion was first mixed with an incompatible agent – the short-chained alcohol, ethanol – until the solution becomes turbid to precipitate the NC particles from the chemically altered solution. The turbid solution was then centrifuged for 3–4 minutes to collect the precipitated NCs separated from the supernatant. After decanting the supernatant, the NC particles were then re-dispersed into the compatible solvent – hexane, octane, toluene, or chloroform, and the precipitation/re-dispersion process was repeated at least three times and finally re-dispersed in chloroform.

A more simplified method to synthesize the PbSe NC was attempted later, introducing a one-pot synthesis instead of two. In this procedure, PbO was used instead of $Pb(Ac)_2$, for the reasons previously mentioned about particle shape irregularities induced by the acetate molecule. As a solvent, both octadecene (ODE) and diphenyl

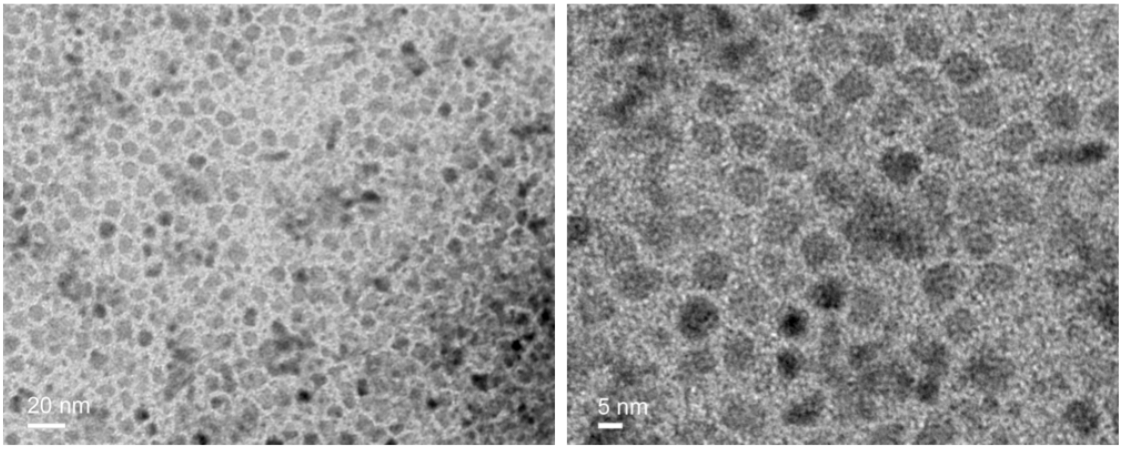

(a) Lead-oleate[1] injected at 150°C, grown for 6 minutes at 123°C and cooled.

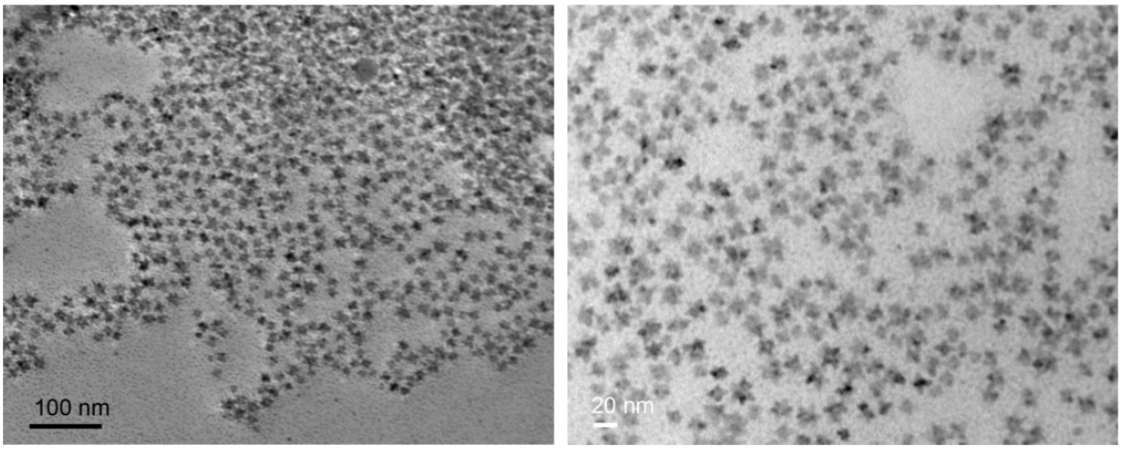

(b) Lead-oleate[2] injected at 150°C, grown for 3 minutes at 123°C and cooled.

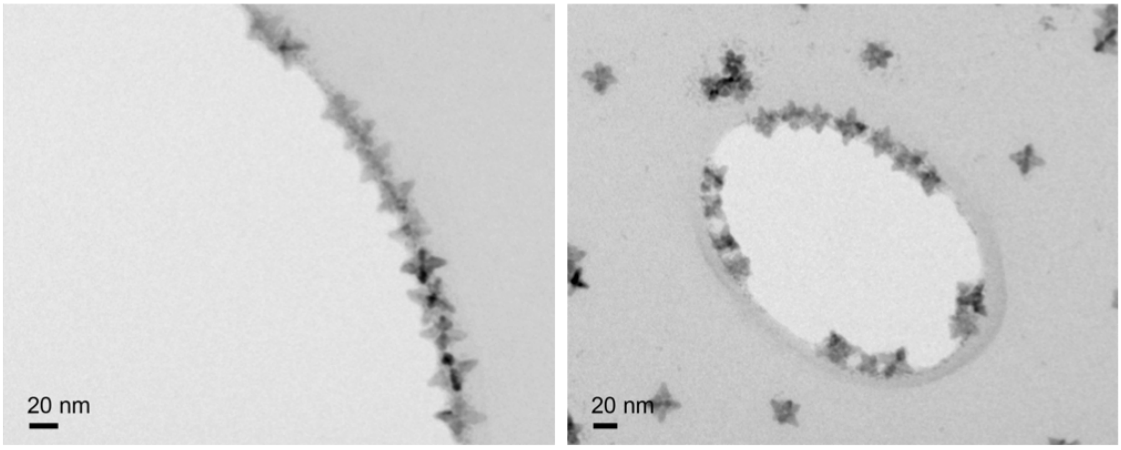

(c) Lead-oleate[2] injected at 180°C, grown for 3 minutes at 142°C and cooled.

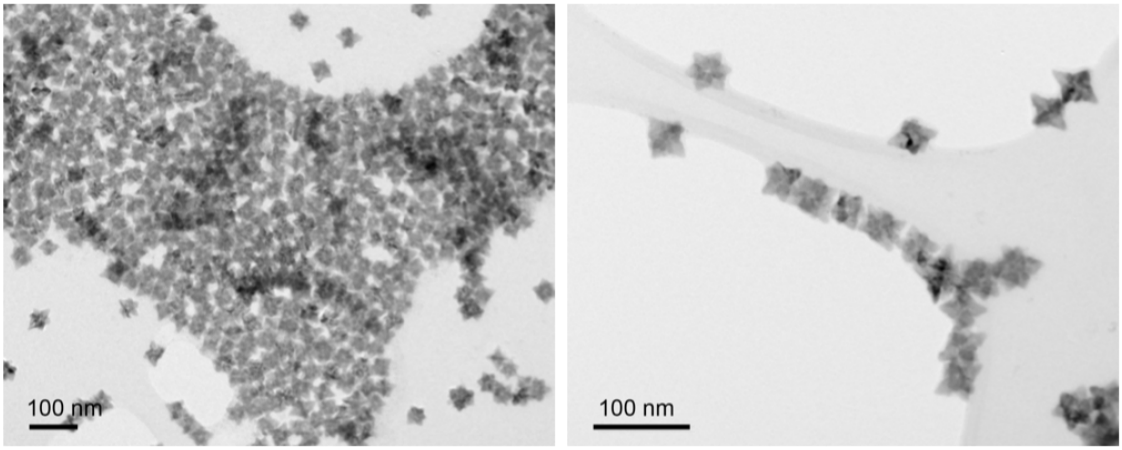

(d) Lead-oleate[2] injected at 210°C, grown for 3 minutes at 165°C and cooled.

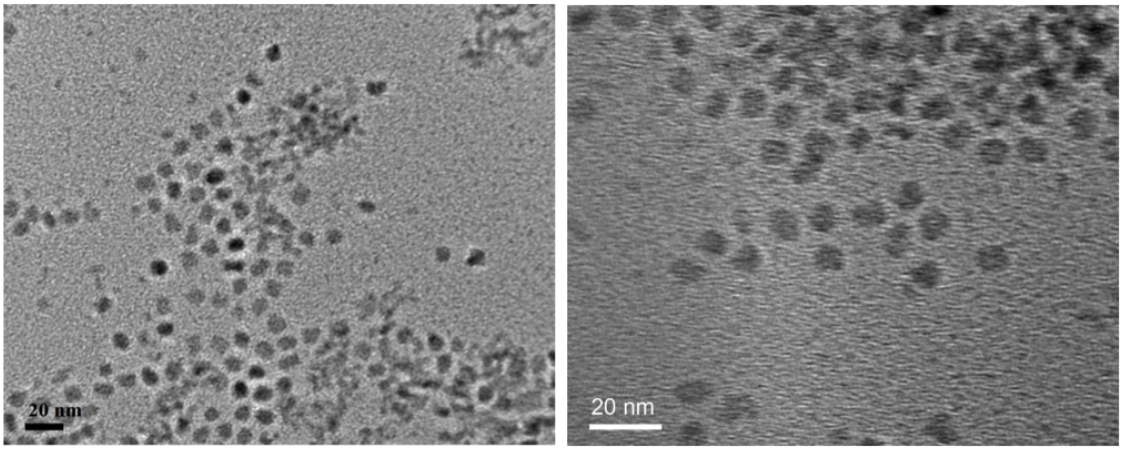

(e) Lead-oleate[1] injected at 180°C, grown for 6 minutes at 115°C and cooled.

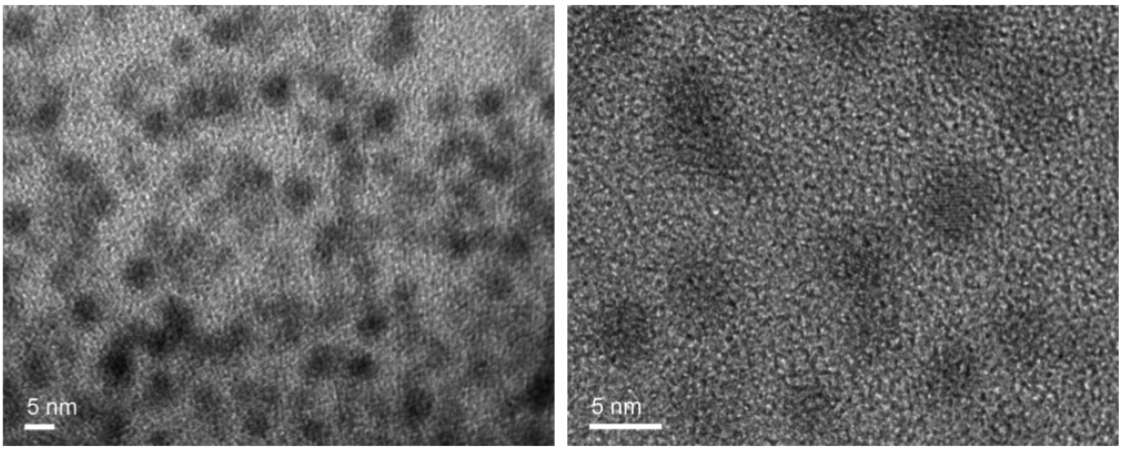

(f) Lead-oleate[1] injected at 150°C, grown for 5 minutes at 115°C and cooled.

Figure 3.7: TEM images of PbSe NC synthesized in various reaction conditions. Refer to the Table 3.1 for Lead-oleate[1,2].

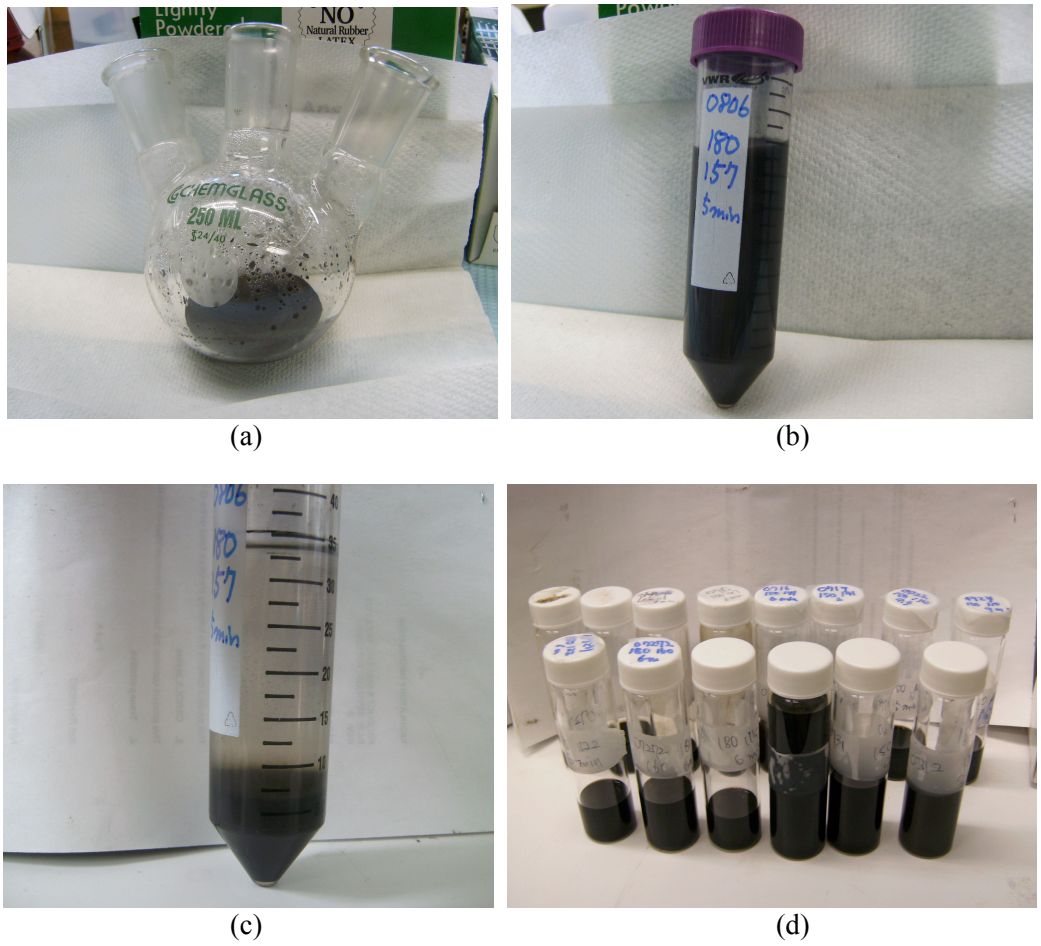

(a) (b)

(c) (d)

Figure 3.8: Quantum dot clean-up process: (a) PbSe NC dispersion after synthesis process (b) Addition of ethanol for NC precipitation (c) Precipitation of PbSe in progress (d) Batches of PbSe NC sample re-dispersed into chloroform.

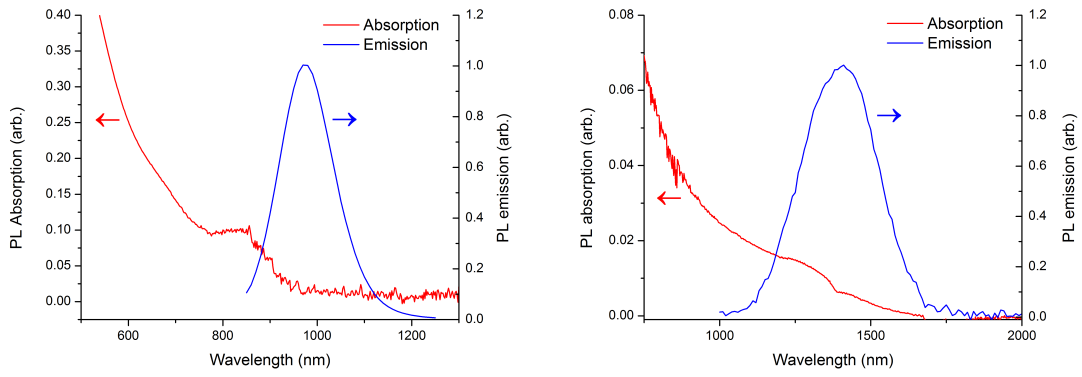

(a) (b)

Figure 3.9: PL absorption and emission spectra of PbSe NCs synthesized through procedure: (a) PbO 0.8 g, OA 3 ml, ODE 10 ml and TOP 8 ml, injected by the TOP-Se precursor where 2M TOP-Se 3 ml is diluted by TOP 10 ml and DIP 0.15 ml, at 170°C followed by immediate quenching, and (b) PbO 0.223 g (∼1 mmol), OA 1 ml, ODE 10 ml and TOP 8 ml, injected by the TOP-Se precursor where 2M TOP-Se 1 ml is diluted by TOP 10 ml and DIP 0.2 ml, at 170°C followed by immediate quenching.

ether (DPE) may work, however, in this process, we used ODE. One example of the synthesis procedure is as follows: Mix PbO 0.8 g, OA 3 ml, ODE (or DPE) 10 ml and TOP (97%, from Sigma-Aldrich) 8 ml in a reaction flask, and heat it to 130°C under vacuum for 60 minutes or more, in order to completely remove the water molecules in the mixture. The TOP-Se precursor for injection is prepared by mixing 3 ml of 2 M TOP-Se (usually prepared ahead as a stock solution – this can be prepared by melting Se shots[1] into the TOP), 10 ml TOP and 0.15 ml di-isobutyl-phosphine (DIP) in a syringe which is kept inert throughout the process. In addition, one can prepare an ice basin to cool down the reaction immediately. One then heats the former Pb-oleate precursor to a temperature slightly over 170°C under argon, after which the heat mantle is removed. As the temperature drops down to 170°C, inject the prepared TOP-Se solution rapidly and immediately plunge the reaction flask into the ice basin. The dispersion will go through the same clean-up procedure as described.

[1]One can use Se powder as well, however, the powder form of Se tends to have more impurities.

Fig. 3.9 shows the photoluminescence (PL) absorption and emission spectra of PbSe NCs synthesized from these two different procedures. The absorption peak, even though not very clear, exists at ∼850 nm in Fig. 3.9(a), and PL emission peak shows a clear emission peak at ∼950 nm. According to the empirical equation reported by Q. Dai *et al.* [45], the size of the NC particle is expected to be ∼2.5 nm. Results from PbSe NCs synthesized via a slightly different procedure by changing relative amounts of PbO, Se and DIP to the entire precursor solution are shown in Fig. 3.9(b). Relatively higher ratio of DIP to the reaction precursor material is expected to expedite the nucleation and growth reaction process. The result shows the absorption peak at ∼1300 nm and the emission peak at ∼1450 nm. Following the empirical equation in [45], the expected size of the particle is ∼4.1 nm.

3.1.3.2 Synthesis of PbS Nanocrystal

In the application of lead chalcogenide NCs, PbS-based devices have been more thoroughly investigated due to their higher relative stability. PbSe NCs are known to be easily oxidized in air, and the fabrication process thus needs to be strictly contained in the glove box in order to assure the nominal optical property of the NCs [97, 98]. In contrast, PbS NC devices are more forgiving. One may eschew PbS due to its lower atomic number compared with PbSe; however, the detection efficiency is not unduly compromised, as can be seen from the MCNPX-Polimi [99] simulation shown in Fig. 3.10. This is because the number of events in the lead chalcogenide assembly is often dominated by the interaction with the Pb atom, as discussed in Appendix A. In other words, the detection efficiency of the material is more effectively determined by the highest atomic number elements in the material when the relative composition is comparable with each other. Thus, it is expected that there wouldn't be a substantial reduction in detection efficiency between using PbS, PbSe or PbTe materials for ionizing radiation detection. For more details on

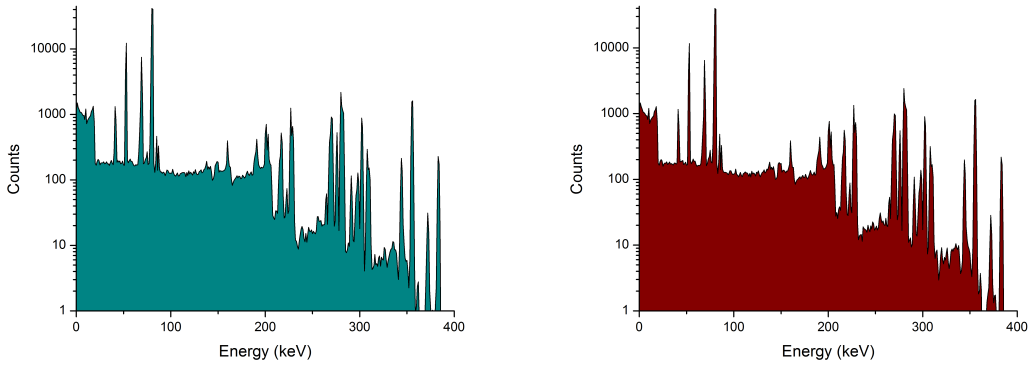

(a) (b)

Figure 3.10: Simulated spectra of Ba-133 from (a) PbS NC and (b) PbSe NC assembly

the Monte Carlo simulation of the detector responses, refer to Appendix A.

Synthesis of PbS NC was conducted following M. A. Hines and G. D. Scholes' procedure [84]. A typical synthesis was performed by injecting bis(trimethylsilyl)sulfide-octadecene mixture (TMS/ODE) prepared *a priori*, into a heated solvent (ODE) containing the lead-oleate precursor, detailed as follows. The lead-oleate precursor was prepared by mixing 0.4 g PbO, 8 ml oleic acid (OA), and 12 ml octadecene (ODE) followed by heating at 120°C for 1 hour in vacuum, to completely evaporate water molecules from the mixture. The TMS/ODE mixture had been previously prepared by mixing 168 μl of TMS into 8 ml of ODE in a glove box. (This mixture is often prepared as a stock solution by mixing a large amount ahead of time). One can inject the TMS/ODE into the reaction flask containing the lead-oleate precursor which is vigorously stirred, at various temperatures, depending on the desired properties of the NCs. In these experiments, TMS/ODE was usually injected at 100°C under an argon environment, and the reaction flask was left to be cooled by the ambient environment, only being stirred without further heating.

In the same way as is done for the PbSe NC synthesis, one can alternate the procedure by changing: a) the injection temperature (T_{inj}), b) the growing temperature (T_{gr}) and time, c) changing the solvent (ODE vs. TOP), and d) changing the mix-

ture ratio of the precursor reagent. Notably, it was reported that one can produce much smaller-sized particles by reducing the molar ratio of (OA:Pb:S) from 32:2:1 to 2:2:1 by diluting with ODE (i.e., dissolving PbO 0.09 g into OA 0.25 ml and ODE 3.75 ml instead of OA 4 ml, for instance) [84]. However, diluting the OA too much makes it hard to dissolve the PbO into the solvent. Thus, one needs enough OA to fully dissolve the PbO with ease. A typical procedure in this experiment uses the (OA:Pb:S) ratio in the range from (12.8:2:1) to (2:2:1), aiming at a relatively smaller sized particle which has shorter wavelength emission (i.e., wider band gap).

The PbS NC particles, after synthesis, were precipitated by adding a polar solvent – acetone and isopropyl alcohol – and centrifuging. The precipitation was then re-dispersed into an organic solvent such as hexane, toluene, or chloroform. The clean-up process was repeated 3 times to properly remove unnecessary solvents and reaction residue. The solvated NC dispersion was centrifuged at a high speed (e.g., 20,000 rpm) to remove any impurities or debris leftover in the solution. Fig. 3.11 shows TEM images of PbS NC synthesized through a typical procedure described previously. Average size of the NC particle was estimated to be 3–4 nm.

3.2 Characterization of Nanocrystals

As some of the previous figures have already shown, synthesized NCs can be investigated using several characterization tools. X-ray diffraction (XRD) can be exploited to check the crystallographic identity and average size of the particle by comparison with the existing diffraction pattern library, and use of Scherrer's euqation. The size and shape of individual particles can be also studied using transmission electron microscopy (TEM), with which one can also conduct elemental stoichiometry analysis via x-ray energy-dispersive spectroscopy (EDS) and electron diffraction pattern analysis, to verify the synthesized material. Photoluminescence (PL) spectra can be obtained to study the optoelectronic properties of the NC particles; specifically, the

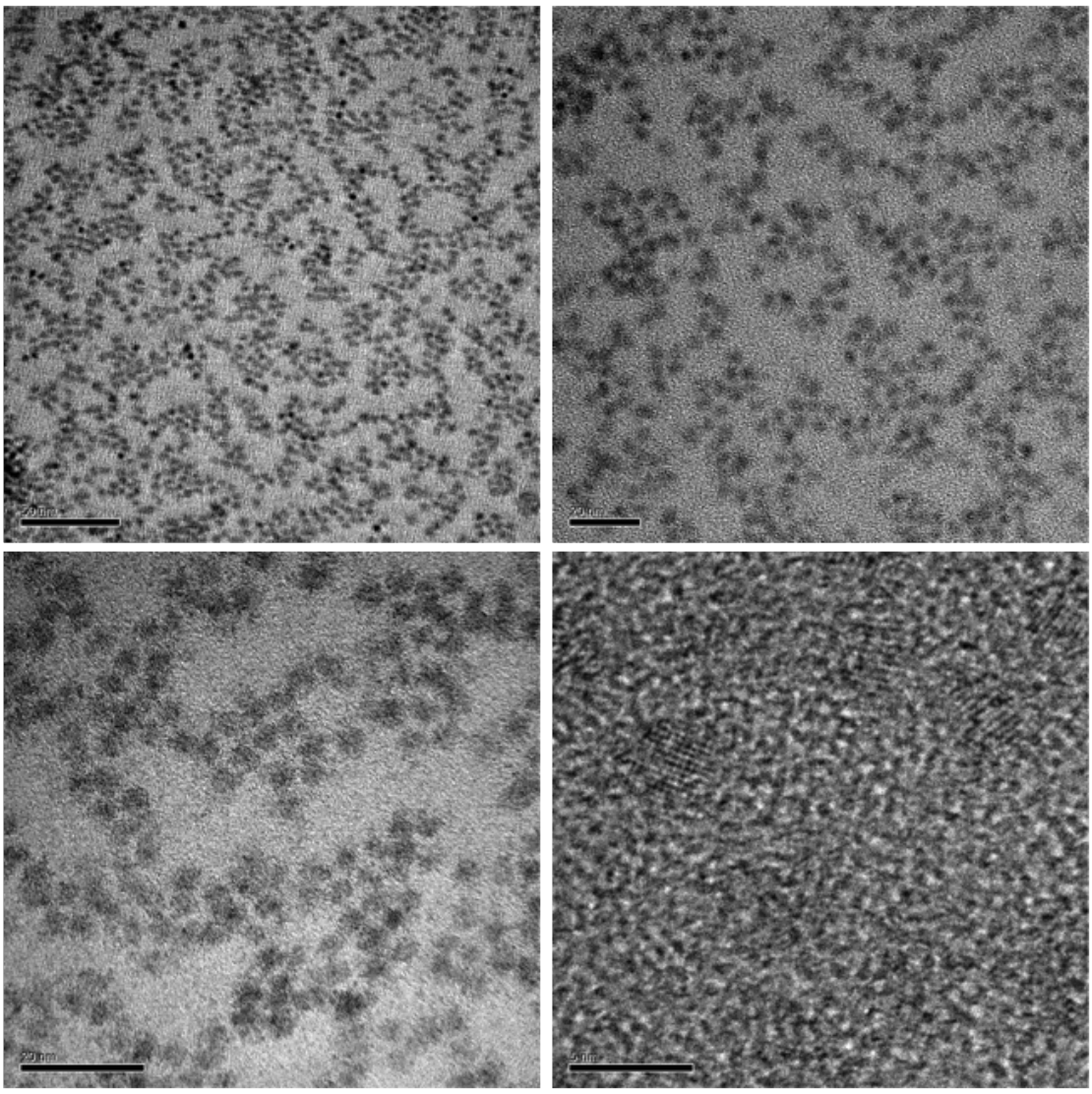

Figure 3.11: TEM images of PbS NCs synthesized through a typical procedure; mixture of PbO 0.09 g, OA 0.25 ml, and ODE 3.75 ml, into which 42 μl of TMS diluted in 2 ml ODE was injected at 100°C.

band-gap energy, through which one can determine the particle size. Typical results from these investigations will be discussed below.

3.2.1 Transmission Electron Micrograph (TEM)

A transmission electron microscope (TEM) has been used as a reliable tool for characterizing NC particles. As it has been already shown in the previous section (3.1.3.1), high resolution TEM (HRTEM) images can be used to verify the size and the shape of the NC particle, as well as the degree of crystallinity. HRTEM images in Fig. 3.12(a)-(c) show closer views of a star-shaped PbSe nanoparticle from the previous section (Fig. 3.7(b)-(d)), observed from the [001] and [111] directions – note that each particle was single crystalline. Lattice fringes shown in the figures represent the crystallographic projection of the lattice sites, gaps of which reflect the distances between lattice planes. Figs. 3.12(a) and (b) show the {200} lattice fringes on the four arms in the x-y plane and this corresponds with the observation of the {220} lattice fringe majority in Fig. 3.12(c). It was shown that the gaps between the fringes match the distances between (200) and (220) lattice planes of the PbSe, considering the crystallographic structure – Rock Salt ($Fm\bar{3}m$) – of the material with the lattice constant $a = 6.13$ Å.

As described in the previous section (3.1.3.1), water molecules introduced from the acetate in the synthesis process, causes the irregularity in the growth scheme of the nanocrystal depending on the crystallographic plane. Fig. 3.13 illustrates the growth scheme of the star-shaped PbSe NC particle. Each arm of the PbSe NC star stretches out to the $\langle 100 \rangle$ directions along each axis, reflecting the fact that this crystallographic direction is the most reactive plane among all the lattice planes.

Electron Diffraction (ED) patterns can be used to investigate the crystal structure of the nanoparticle – an example for PbSe is shown in Fig. 3.14. Due to the random orientation of each particle on the TEM sample mount, patterns of diffracted elec-

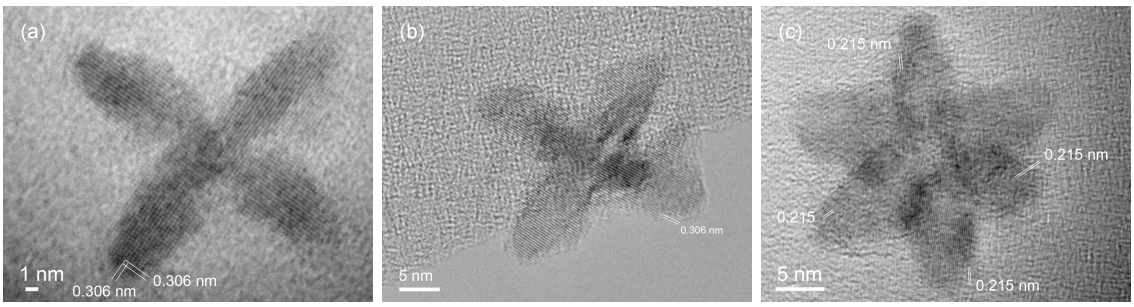

Figure 3.12: High Resolution Transmission Electron Micrograph (HRTEM) images of star-shaped PbSe NC particle. (a) and (b) corresponds to Fig. 3.7(b) and Fig. 3.7(c) observed from [001] direction, and (c) corresponds to Fig. 3.7(c) observed from [111] direction.

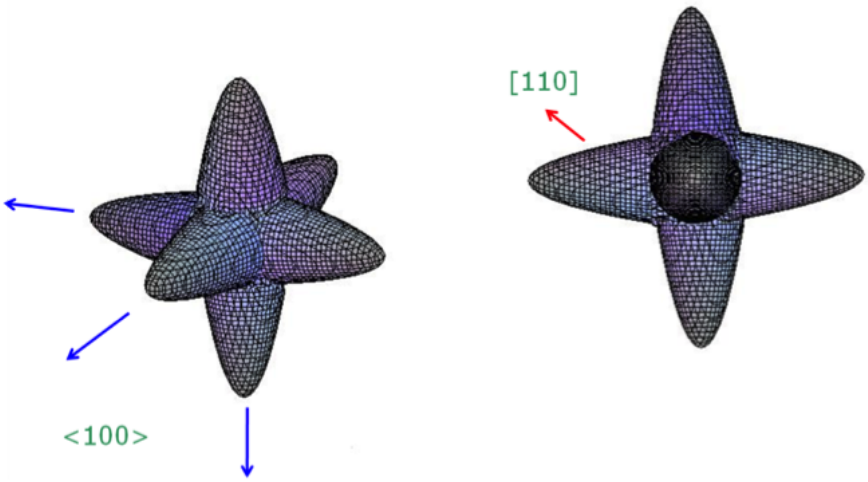

Figure 3.13: Illustration of star-shaped PbSe NC particle in terms of the particle growth direction.

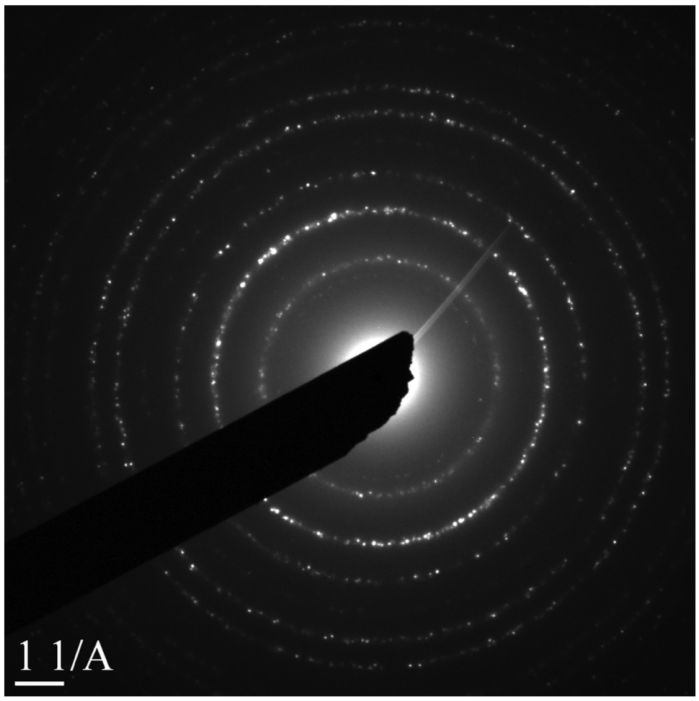

Figure 3.14: Electron Diffraction (ED) pattern of the PbSe NCs.

tron beams will make several concentric circles, of which existence and radii will be determined respectively by the structure factor and distances between lattice planes calculated from the crystalline structure of the PbSe. By matching the relative ratio of the radii of the concentric circles with spacing between designated lattice planes, one can verify the crystal structure of the material.

X-ray energy dispersive spectroscopy (EDS), derived from the detection of x-rays produced during electron impingement in the electron microscopes, enables stoichiometric composition analyses on the sample. An example of the spectrum obtained for the PbSe NCs with the stoichiometric analysis of the element is shown in Fig. 3.15. The spectrum shows the expected peaks from the various K and L atomic transitions from the constituent elements, and with areas in the expected ratios, if proper corrections for all the possible factors – atomic weights, ionization cross sections, fluorescence yields and relative transition probabilities of constituent elements, self-attenuation of x-rays in the sample, and detection efficiency of the x-ray detector

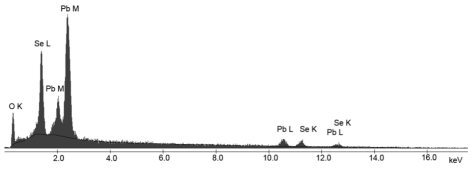

EDAX ZAF Quantification
Composition analysis

Element	Wt%	At%	K-ratio	Z
PbL	75.79	54.40	0.7183	1.0067
SeL	24.21	45.60	0.2754	0.9828
Total	100.0	100.0	·	·

Figure 3.15: X-ray energy dispersive spectrum (EDS) and the elemental composition analysis of the PbSe NCs.

– are accurately considered. Known approaches to quantitative elemental analysis of the specimen involves the Cliff-Lorimer method (determining k-factor) and the zeta-factor method developed by Watanabe and Horita [100].

3.2.2 Photoluminescence (PL)

Photoluminescence can be used to probe the electronic structure of materials, by impinging light upon a colloidal dispersion of NCs, such that photo-excitation results. When the excited electrons make transitions to their equilibrium states, the excess energy can be dissipated via either radiative or non-radiaitive processes. The energy of the emitted light (photoluminescence) relates to the difference in energy levels between the two electronic states involved in the transition between the excited state and the equilibrium state, and the quantity of the emitted light is related to the relative contribution of the radiative process.

One can determine electronic properties of the material, such as band gap, impurity levels and defect-recombination mechanisms from the PL measurement. The most common optical transition in semiconductors is between states in the conduction and valence bands, with the energy difference being known as the band gap, which can be estimated from the onset of the PL absorption. Fig. 3.16 shows a typical absorption spectrum of CdTe NC obtained in the ultraviolet (UV)-visible light (VIS) range, which exhibits a first absorption peak at 550 nm, which is equivalent to 2.25 eV. The CdTe NC dispersion was synthesized following the procedure described in (3.1.1.1). The size of the NC can be measured both qualitatively and quantitatively from the

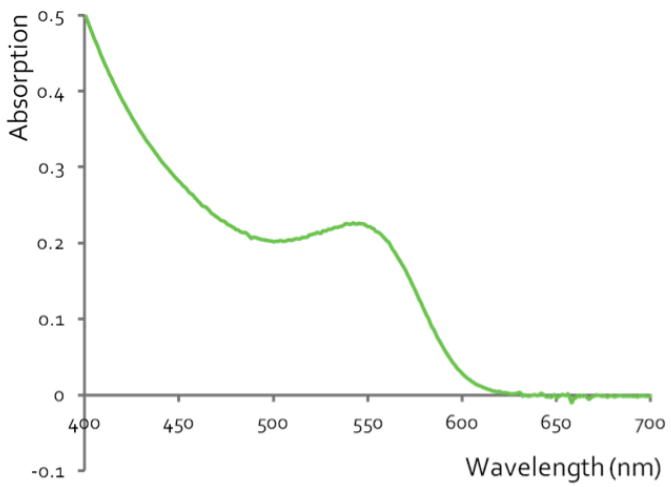

Figure 3.16: A typical UV-VIS absorption spectrum of CdTe NC.

PL absorption spectrum. Notably, longer wavelength absorption corresponds to lower energy photons used to initiate a electronic transition in the particle, and the smaller band gap corresponds to a larger size of the NC particle. Based on the empirical equation on the extinction coefficient, the particle size, and the concentration suggested by W. Yu *et al.* [43], of which the result was presented in the previous section (2.1.2.4 – Fig. 2.6), the average size of the CdTe NC particles was determined to be 3.24 nm and the concentration of the particle in the dispersion was calculated to be $\sim 10^{15}$ particles/cm^3.

PL *emission* spectrum provides a wavelength distribution of photons emitted as a result of the radiative decay of an exciton. Since emission wavelength is also determined by the electronic density states of the material, which depends on the size of the NC particle, a narrower distribution of the PL emission peak reflects a more uniform size distribution of the NC dispersion. Fig 3.17 shows the PL emission and excitation spectra of a CdTe NC dispersion after the size-selective precipitation process (Fig. 3.17(a)). The original NC dispersion was also synthesized through the process described in (3.1.1.1), and it had shown the PL absorption peak at $\lambda_{abs} \approx 535$ nm and PL emission at $\lambda_{em} \approx 550$ nm. Different sizes of CdTe NCs were separated, as

indicated visibly in Fig. 3.17(a), and qualitatively shown by the different positions of PL emission peaks (Fig. 3.17(b)). The movement in the peak from right (orange) to left (blue-supernatant) indicates that the particle size is decreasing as size-selective precipitation is employed. PL excitation spectra in Fig. 3.17(c) reflects the internal electronic density states of the NC related with the radiative excitonic emission.

Fig. 3.18 shows PL absorption and emission spectra obtained from PbS NCs synthesized following the procedure elaborated in the previous section (3.1.3.2). Specific reaction conditions for the synthesized samples and the corresponding absorption and and emission wavelength are listed in Table 3.2.

Label	OA:Pb:S	T_{inj}	λ_{abs}	λ_{em}
0524	12.8:2:1	100°C	1120 nm	1200 nm
0529	2:2:1	100°C	930 nm	1100 nm
0530	2:2:1	95°C	855 nm	1050 nm

Table 3.2: Synthesis of PbS NC varying precursor ratio and injection temperature.

3.2.3 X-ray Diffraction (XRD)

X-ray diffraction (XRD) is commonly used to investigate the crystallographic properties of the material. The usage of the XRD includes a determination of such information as: phase composition of a sample and its quantitative analysis, unit cell lattice parameters and Bravais lattice symmetry, residual strain (macrostrain), epitaxy/texture/orientation of the sample crystal, crystallite size and microstrain indicated by peak broadening and other defects such as stacking faults.

Diffraction occurs when each object in a periodic array scatters radiation coherently, producing constructive interference at specific angles. The electrons in an atom interact with the oscillating electric field of the light wave and coherently scatter light. Since atoms in a crystal form a periodic array of coherent scatterers and the wavelengths of x-rays are similar to the distance between atoms, diffraction from different planes of atoms produces a diffraction pattern, which contains information about the

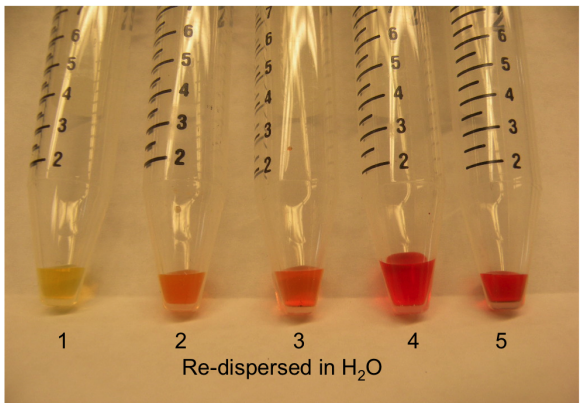

(a)

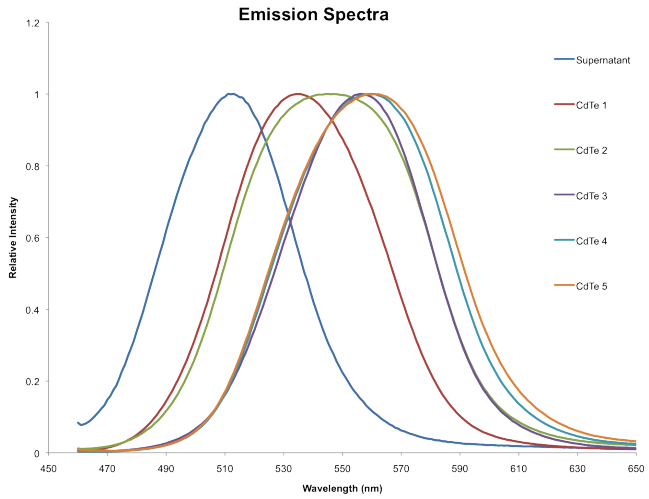

(b)

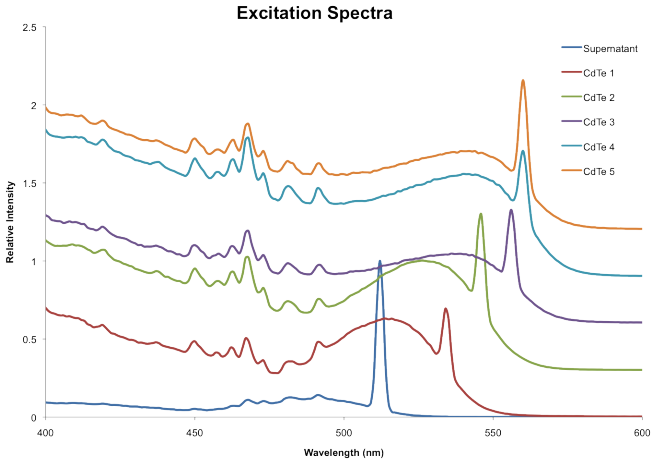

(c)

Figure 3.17: (a) Size-selectively precipitated CdTe NCs and the corresponding (b) PL emission and (c) PL excitation spectra obtained from each batch of the sample.

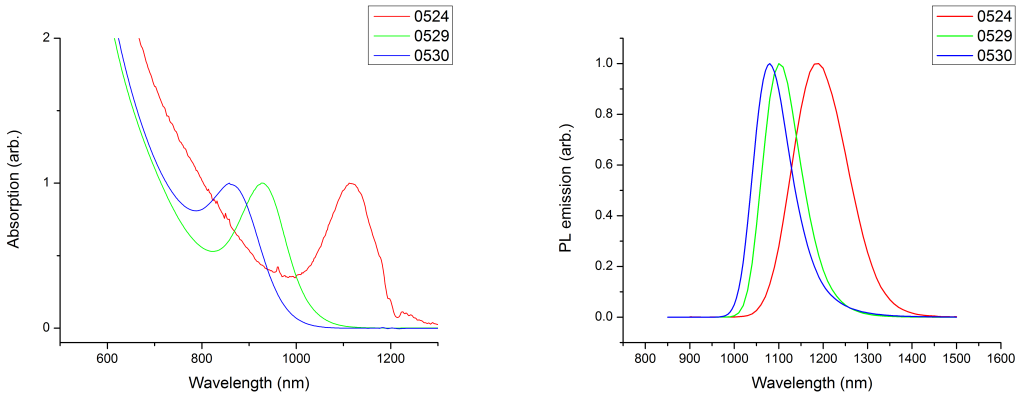

(a) (b)

Figure 3.18: (a) PL absorption and (b) PL emission spectra of PbS NC synthesized in various condition listed in Table 3.2.

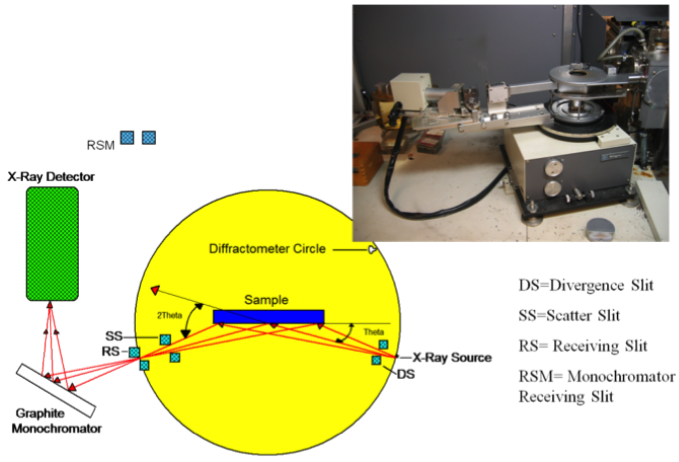

Figure 3.19: Schematic illustration of the Rigaku rotating anode XRD machine located at XMAL in the University of Michigan.

atomic arrangement within the crystal. Fig. 3.19 shows the setup of a Rigaku rotating anode XRD machine located at XMAL in the University of Michigan, used to perform powder diffraction for the NC particles.

For parallel planes of atoms, with a space d_{hkl} between the planes, constructive interference only occurs when Bragg's law is satisfied, which is given by: $n\lambda = 2(d_{hkl}) \sin\theta$. In the diffractometer, the wavelength of the x-ray is fixed via source selection. Consequently, a family of planes produces a diffraction peak only at a specific angle. The space between diffracting planes of atoms determines the peak positions

and the peak intensities in the spectrum, which depend on several factors including: what atoms are in the diffracting plane, the multiplicity of the plane, the crystalline structure of the material, and the linear absorption coefficient of the material.

The intensity of the peaks in the diffraction pattern reflects the total scattering from the each plane and can be represented as:

$$I_{(hkl)\alpha} = \frac{I_0 \lambda^3}{64\pi r} \left(\frac{e^2}{m_e c^2}\right)^2 \frac{M_{(hkl)}}{V_\alpha^2} |F_{(hkl)\alpha}|^2 \left(\frac{1+\cos^2 2\theta \cos 2\theta_m}{\sin^2\theta \cos\theta}\right)_{(hkl)} \frac{\nu_\alpha}{\mu_s}. \qquad (3.1)$$

where:

$I_{(hkl)\alpha}$: intensity of reflection of hkl in phase α

I_0 : incident beam intensity

r : distance from specimen to detector

λ : x-ray wavelength

$\left(\frac{e^2}{m_e c^2}\right)^2$: square of classical electron radius

μ_s : linear absorption coefficient of the specimen

V_α : volume fraction of phase

$M_{(hkl)}$: multiplicity of reflection hkl of phase α

ν_α : diffraction angle of the monochromator

$F_{(hkl)\alpha} = \sum_{j=1}^{s} f_j \; e^{-i\overrightarrow{G_{hkl}}\cdot\overrightarrow{r_j}}$, where, $f_j = \int_{cell} dV \; n_j(\vec{\rho}) \; e^{-i\overrightarrow{G_{hkl}}\cdot\vec{\rho}}$

: structure factor for reflection hkl of phase (i.e., the vector sum of scattering intensities of all atoms contributing to that reflection)

As mentioned above, by comparing the position and the relative intensity ratio between peaks with the Powder Diffraction File (PDF) library, we can verify the crystal structure of the material.

In addition, crystallites smaller than ∼100 nm create broadening of the diffraction peaks due to the limited number of unit cells that satisfy the Bragg condition. This peak broadening (FWHM) can be used to quantify the average crystallite size of nanoparticles using the Scherrer equation, as shown in Eq. 3.2. However, one must know the contribution of peak width from the instrument by using a calibration curve, *a priori*, and microstrain may also create peak broadening; thus, one must separate microstrain from crystallite size by analyzing the peak widths over a long range of 2θ, which is done by using Williamson-Hull method in the XRD profile analysis software (JADE).

$$B(2\theta) = \frac{K\lambda}{L\cos\theta} \qquad \text{(Scherrer Equation).} \tag{3.2}$$

A batch of several reaction conditions for PbSe NC dispersion synthesis are tabulated in Table 3.3 and XRD spectra for each sample are shown in Fig. 3.20. From the XRD spectrum patterns, it was verified that the peaks of the pattern from every sample exactly match with the peaks of the PbSe in the Powder Diffraction File (PDF) library. The lattice constant calculated from the peak location also matches the lattice constant of PbSe which has $Fm\bar{3}m$ cubic structure. The average size of the particles was estimated by Scherrer's formula (Eq. 3.2) from the mean FWHMs of the peaks. One expects that the particles will grow larger when reacted for either longer periods or higher temperatures, an expectation met as shown in Fig. 3.20. The XRD spectra exhibit peak broadening as the size of the particle decreases.

Table 3.3: Various synthesis conditions for PbSe NC samples – injection temperature (T_{inj}), growth temperature (T_{gr}), and growing time.

Label	Precursors	T_{inj}	T_{gr}	Time
Sample 1	Lead-oleate[1]	150°C	113°C	6 min.
Sample 2	Lead-oleate[1]	150°C	120°C	3 min.
Sample 3	Lead-oleate[1]	150°C	123°C	6 min.
Sample 4	Lead-oleate[1]	180°C	139°C	5 min.

[1] $Pb(Ac)_2$ 0.65 g, DPE 2.0 ml, TOP 8.0 ml, and OA 1.5 ml mixed with 1.7 ml of TOP-Se

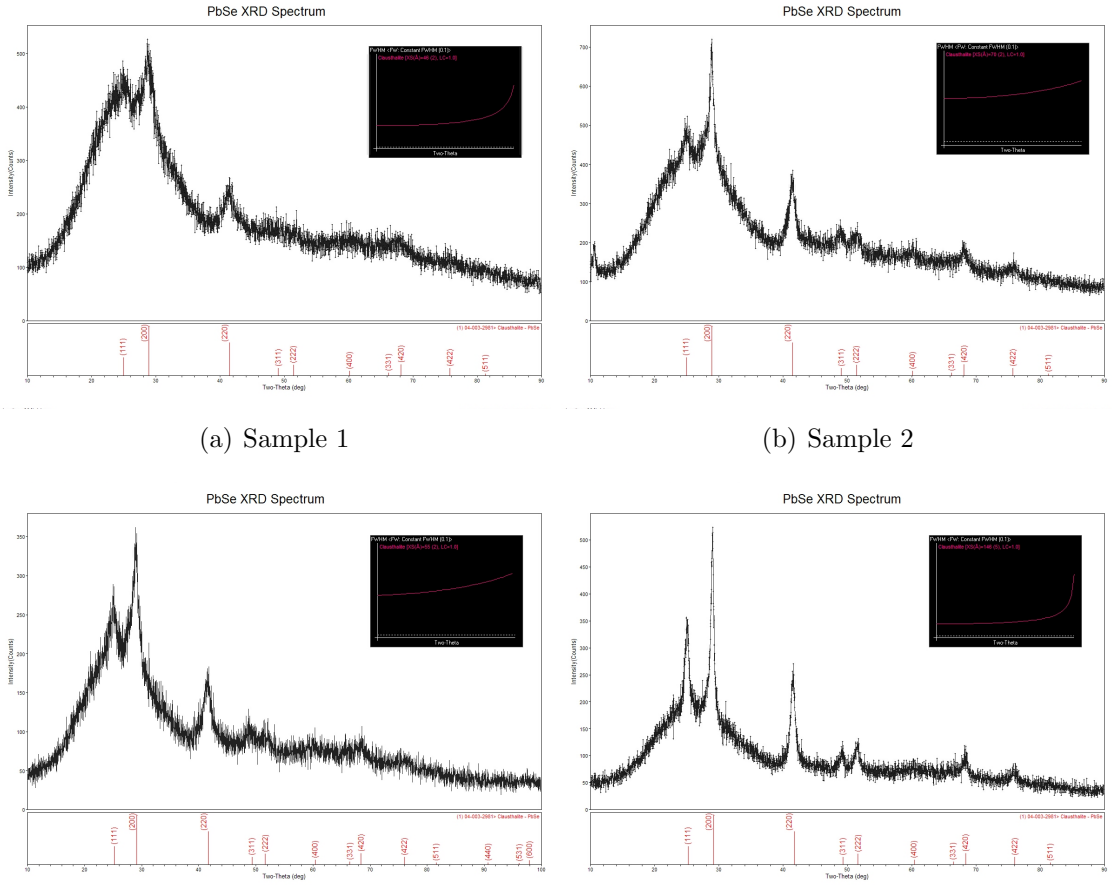

(a) Sample 1

(b) Sample 2

(c) Sample 3

(d) Sample 4

Figure 3.20: X-ray diffraction (XRD) spectra of PbSe NC samples synthesized in various conditions.

Specifically, the spectrum in Fig. 3.20(d), for which particles were grown at the highest temperature and thus yielded the largest size, shows relatively discernable peaks compared with the other spectra. In Fig. 3.20(a), the peaks were broadened and highly distorted due to the smaller expected size of the particles. Comparing Figs. 3.20(b) and 3.20(c), Fig. 3.20(c) shows slightly less behavior of the broadening, with more discernable peaks at the higher angles, even though they do not show a big difference in their reaction temperatures. This could have originated from the different growing time, which allows enough time for the precursors to diffuse between the particles to form mono-dispersed NC particles.

The average diameter of the particles, which formed either spheres, six-pointed

stars, or cubes – depending on the preparation recipe – was estimated via the peak profile analysis using the JADE XRD spectrum analysis program. This rather imprecise measure was buttressed by TEM and PL spectra, which were used to perform a more detailed analyses on the mean size and variance in the NC particle size in the solution.

3.3 Fabrication of Nanocrystal Assembly

Synthesized NC particles inherently self-assemble, if properly coordinated with organic ligands. Solution-based formation of the colloidal assembly is accompanied by the solvent evaporation. Depending on the nature of the solvents – viscosity, volatility, and compatibility, the dynamics of the assembly formation diversifies. As previously mentioned, the most important but critical problem in the NC approach is: *how to maximize the colloidal ordering as the solvent evaporates?*

NC particles dispersed in the non-polar solvent can be deposited on the substrate mainly using four methods: drop-casting, dip-coating, the slide-casting method, and spin-casting. Drop-casting is the process of depositing a droplet of the NC solution on the substrate and repeating the procedure, while allowing time for the solvent to evaporate between applications. Dip-coating is utilizing the adsorbing nature of the small particle which has very high surface energy due to the high-surface-to-volume ratio. The amount of adsorption is controlled by the balance between viscosity and volatility of the solvent, and the gravity exerted by the NC dispersion. Thus, in order to control the gravitational force applied to the NC dispersion, an intermediate method between the previous two method was attempted: termed the slide-casting method. This method consists of dripping the NC dispersion onto the substrate leaned against the supporting block. The solution flows along the substrate driven by the gravitational force; however, not as fast as vertical dip-coating. Therefore, one can expect a thicker layer of NC adsorption from this method than that from dip-

coating. Meanwhile, spin-casting is the process of dripping a droplet of the solution on a spinning substrate, for which the spread of the solution is driven by the centrifugal force of the spinning substrate, controlled by the viscosity of the solution. This method allows more uniform spreading of the NC solution as well as more rapid drying as the substrate is spun at a higher rate.

The aforementioned four methods can be combined with approaches to enhance the charge transport properties of the assembly. For example, layer-by-layer (LBL) deposition, which results in a uniform NC assembly, can be done via spin-casting, dip-coating or the slide-casting process. A blended structure of NC/polymer composites can be formed through either drop-casting or a slow spin-casting method. All of the these processes can be combined with a ligand-exchange treatment to enhance the hopping transport mechanism between NC particles by reducing the inter-particle distance and thus, closely-packing the NC assembly [23, 101–103]. NC assemblies of PbS, PbSe, and CdTe NCs fabricated with various procedures and methods will be introduced in the following sections. There are various assembly routes including: drop-casting without any additional treatment, LBL with dip-coating, spin-casting and slide-casting, and NC/polymer blended composite approaches using drop-casting and slow spin-casting.

One important factor to be considered in the fabrication of thick assembly samples as opposed to thin-film detectors, is that, although sensors were made based on repeated procedures of spin-cast monolayers or simply based on the layer-by-layer method, the colloidal NC dispersion was allowed to self-assemble in thick layers, and the spinner was used mainly as a tool to increase the uniformity of the detector, relative to pure drop-casting. That is, the solid, which can vary from tens of micrometers to a few millimeters, can be formed from the casting of tens or hundreds of layers depending on the spinning speed, and on the quantity of NCs cast in the single-layer drop.

Another factor that has to be also noted is the manner in which the fabrication recipe differs from those employed to sense quanta with short interaction lengths, such as optical photons. First, although the dispersion is nucleated and grown in either argon or vacuum environments, the casting of the colloidal solid is done in air, and one can therefore anticipate the rapid oxidation of any exposed NC surfaces, as an experimental study has proved for the PbSe NCs [98]. Note that although oxidation of the NC can potentially suppress recombination via increased band-gap due to the reduction of the size of the NC core, one generally desires to avoid surface oxidation because of carrier trapping [98].

3.3.1 Drop-cast plain NC assemblies

NC assemblies were initially formed from the colloidal dispersion, *as synthesized*, via the drop-casting method. With CdTe and PbSe particle dispersions, the colloidal NC assembly solids were constructed via repeated applications of drop-casting on the metal substrate, as illustrated in Fig. 3.21. That is, a bottom contact of gold or lead was deposited on a dielectric (printed circuit board, glass) or semiconductor (silicon) substrate.[2] The colloidal NC was then drop cast to form a solid layer, repetitively conducted several hundred times, each repetition requiring tens of seconds of drying, resulting in diagnostic samples that were a few hundred micrometers thick. Finally, a top contact of aluminum was patterned and isolated electrically from the bottom metal electrode. Note that in contrast to some forms of electronic nanotechnology – carbon nanotubes and graphenes, for instance – achieving large detector volumes with the drop casting method did not involve the invention of a new fabrication process but merely the repeated application of a single droplet to the active area formed *a priori*; however, one must compensate for the cracks that form during the drying

[2]Refer to Appendix B, for the detailed procedure in preparation of the substrate via microelectronic processing – photolithography.

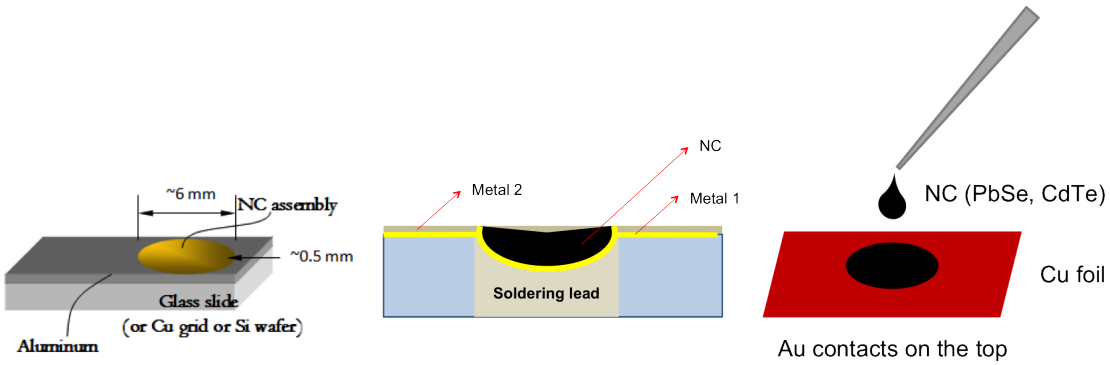

(a) (b) (c)

Figure 3.21: Schematic of NC assembly made by drop-casting NC dispersion on (a) metal-evaporated glass or silicon substrate (b) PCB based substrate and (c) copper foil.

stages, which can be accomplished by applying a dilute solution of the dispersion [3] or by applying rather highly concentrated solution to fill in the open spaces.

Fig. 3.22 shows the surface morphology of the CdTe NC assembly investigated by an SEM. As shown in Fig. 3.22, the NC particles, encased in organic ligands, coagulated into larger agglomerations as expected given the assembly method used. The drop-casting method was implemented by dropping and drying ∼0.1 mL of the CdTe NC solution 30 times on the metalized substrate as shown in Fig. 3.21(a). The assembly of approximately 6 mm diameter was created, and the thickness of the film was estimated to be ∼300 μm (The thickness was comparable to the thickness of a wafer). However, the variance in thickness deposited with simple drop-casting method was substantial.

Figs. 3.23 and 3.24 show a few representative drop-cast PbSe NC assembly samples and their SEM images, as the deposition schematically shown in Fig. 3.21. The NC dispersion was carefully dropped on the metalized substrates (not to damage the pre-existing assembly) and dried completely. Before the deposition of the top gold metal contact, the surface morphology of PbSe NC assembly samples was investigated by

[3] In this case, the diluted solution will dissolve part of the existing assembly to smoothen out the boundary.